2015

Hierarchical Engineering of Multimodal Ordered Nanoporous Materials

Shih-Chieh Kung
Lehigh University

Hierarchical Engineering of Multimodal Ordered Nanoporous Materials

by

Shih-Chieh Kung

Presented to the Graduate and Research Committee

of Lehigh University

in Candidacy for the Degree of

Doctor of Philosophy

in

Chemical Engineering

Lehigh University

May, 2015

Certificate of Approval

Approved and recommended for acceptance as a dissertation in partial fulfillment of the requirements of the degree of Doctor of Philosophy.

_____
Date

_____
Mark A. Snyder, Ph.D.
Dissertation Advisor

_____
Accepted Date

Committee Members:

_____
Mark A. Snyder, Ph.D.
Committee Chair

_____
James F. Gilchrist, Ph.D.
Committee Member

_____
Jeetain Mittal, Ph.D.
Committee Member

_____
H. Daniel Ou-Yang, Ph.D.
Committee Member

Acknowledgements

I am deeply grateful to my advisor, Prof. Mark A. Snyder. Without his patient guidance, discussion, encouragement, and support, my research work would not have been possible. I would like to take this opportunity to thank my committee members, Prof. James F. Gilchrsit, Prof. Jeetain Mittal, and Prof. H. Daniel Ou-Yang, for their insightful discussion and guidance in my research work.

I owe my gratitude to all my colleagues in Prof. Snyder's group and friends in the department who had made this dissertation possible. Especially, I shall thank Zheng Tian, and Qianying Guo for helping me be familiar with the lab and sharing the theoretical and experimental knowledge with me in my research, Daniel Gregory for his creative ideas and supportive discussion, Minseok Song for his thoughtful suggestion and inspiration, and Midhun Joy for supporting my research work. I also want to thank Tanyakorn Muangnapoh, Fan Ni, Yajun Ding, and Zhou Yang for helping me out whenever needed. Without the continuous support from Prof. Wei Fan and his group at Department of Chemical Engineering in University of Massachusetts Amherst, this thesis would not be possible.

The steady progress of my work would not have been possible without the continuous support from the staff in Department of Chemical Engineering. I'd like to thank John Caffrey for helping set up the hardware of my experiment, and Paul N. Bader for electronics support and trouble-shooting. I would also like to thank Barbara Kesslar, Tracey Lopez, and Janine Jekels for their kindly support throughout the course of my research work.

I'd like to acknowledge the funding for portions of the research in this thesis provided by the Donors of the American Chemical Society Petroleum Research Fund

through grant ACS-PRF-50429-DNI5, as part of the Catalysis Center for Energy Innovation, an Energy Frontier Research Center funded by the U.S. Department of Energy Office of Science, Office of Basic Energy Sciences under award # DE-SC0001004, and by the National Science Foundation grant CBET-1351613.

Finally, I wish to thank my wife, Chin-Wen Wu, for her constantly support in my life, and my family for everything that cannot put into words.

Table of Contents

List of Tables

List of Figures

Abstract

Nanoporous materials have attracted extensive research interest owing to their potential for applications spanning arenas as diverse as energy (e.g., catalysts, separations), the environment (e.g., sorbents), and health (e.g., drug delivery). The ability to achieve tunable control over pore size, dimensionality, and specific pore topology is a persistent challenge when it comes to rational synthesis of micro-, meso-, and/or hierarchically-porous materials. In this thesis, we develop a multiscale synthetic strategy and its fundamental physicochemical underpinnings for realizing nanoporous and hierarchically porous materials with three-dimensionally ordered pores spanning classes of nanoporous materials as diverse as amorphous mesoporous silicas, micro-mesoporous carbons, and crystalline microporous zeolites. We also demonstrate the versatility of this approach in terms of material morphology from porous particles/powders to thin films.

We establish strategies for bottom-up assembly of binary silica nanoparticles for realizing template-free ordered mesoporous silicas (OMSs). We first study the phase behavior of evaporation-induced convective assembly of binary silica nanoparticles, and show that even without specific solvent index matching or stabilization beyond intrinsic properties of the amino acid nanoparticle synthesis solution, symmetry of the binary assemblies is governed solely by particle size ratio, consistent with binary hard-sphere predictions. The demonstrated robustness of the binary nanoparticle assembly and the control over silica particle size translate to a facile, template-free approach to OMSs with independently tunable pore topology associated with the interstices of AB, AB_2 , AB_{13}, and AB interstitial nanoparticle crystals that are isostructural with NaCl, AlB_2, and $NaZn_{13}$. Moreover, we elucidate the role of the amino acid, L-lysine, employed in the nanoparticle

synthesis, the structural evolution of the silica network upon aging of dialyzed nanoparticle sols, and substrate character in tuning particle stability and thereby the yield of ordered binary assemblies achievable in both bulk and thin film morphologies.

We subsequently employ these novel multi-modal OMSs as sacrificial hard templates in realizing a facile method to synthesize a new class of bimodal three-dimensionally ordered mesoporous (b-3DOm) carbons with tunable bimodal mesoporosity. Continuously adjustable bimodal mesoporosity in the range of 15-23 nm for small pores and 40-50 nm for large pores with controlled pore topology is confirmed. Attractive textural properties result, including high surface areas (>1000 m^2/g), narrow pore size distributions, and large pore volumes (2-5 cm^3/g). The structural stability of these large-pore volume materials is underscored by the pore robustness upon removal of the hard sacrificial silica template and even in the face of carbon loss during subsequent activation of microporosity in the carbon walls.

We conclude the thesis by demonstrating a top-down strategy to scaffold the growth of ultra-thin crystalline microporous (zeolite) films. Here, we combine nanoparticle crystal-templated carbon thin films to force in-plane crystal growth. Through tuning of nucleation and growth within the carbon film scaffolds, the strategy developed in this thesis enables realization of large silicalite-1 crystal regions formed by intergrowth of separately nucleated crystal domains. The thickness of the silicalite-1 domains can be tuned and scaled down to the order of 10 nm by controlling the carbon scaffold thickness, with remarkable flexibility of the inorganic films observed.

Chapter 1:

Introduction

1.1 Motivation and Objectives

1.1.1 Promise and challenges of nanoporous materials

Nanoporous materials have attracted extensive research interest owing to their potential for applications spanning separations, catalysis, adsorption, and drug delivery, among others.[1-7] There are three categories of nanoporous materials (**Figure 1-1**) classified on the basis of their pore sizes: 1) micro-, 2) meso-, and 3) macroporous materials with the pore size 1) smaller than 2 nm, 2) between 2 to 50 nm, and 3) larger than 50 nm, respectively. The physical and chemical properties (e.g., morphology, pore architecture, surface area and functionality) defining nanoporous materials dictate their applicability among various fields.

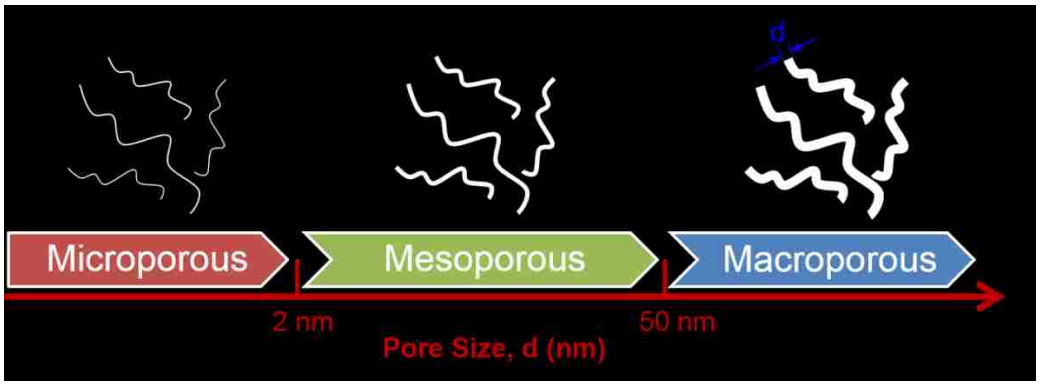

Figure 1-1. Three categories of nanoporous materials classified by pore size.

In most applications, it is the way in which these structural and functional features modulate the transport of molecular species within the nanoporous network that determines material applicability, e.g. drug release profile in therapeutic applications, molecular uptake and loading in adsorption-based separations, molecular transport in continuous membrane-based separations, matched transport and reactivity in catalysis, etc. Yet, the ability to achieve tunable control over pore size, dimensionality, and specific pore topology is a persistent challenge when it comes to rational synthesis of micro-, meso-, and/or hierarchically-porous materials of a range of compositions such as metal oxides, zeolites, and carbons, among others.

The **overarching goal** of this dissertation is to develop a versatile synthetic strategy and its fundamental physicochemical underpinnings for realizing nanoporous and hierarchically porous materials with three-dimensionally ordered pores across classes of nanoporous materials as diverse as amorphous mesoporous silicas, micro-mesoporous carbons, and crystalline microporous zeolites. In order to meet this goal, we have developed integrated bottom-up nanoparticle assembly and top-down template-assisted synthesis approaches. The integrated nature of this strategy and the resulting insight it provides across material classes represents a significant step forward in the rational design of inorganic nanoporous materials to better meet requirements of their applications.

1.1.2 Role of diffusivity and diffusion length scale for practical applications

A primary motivating factor for controlling the pore size, topology, and order in bulk and thin-film micro- and meso-porous materials derives from the desire to realize rapid molecular transport since diffusion is a common rate-limiting step in many

technological processes. Namely, the ability to enhance the diffusivity and/or to control the diffusion length scale of porous materials in either bulk (e.g., powder) or thin film morphology is essential to enhance the throughput and efficiency of processes spanning heterogeneous catalysis to adsorption- and membrane-based separations, respectively.

Figure 1-2 illustrates the concept of diffusivity and diffusion length scales in both of these material morphologies. For example, in the context of porous adsorbents and/or catalysts (i.e., particulate/powder morphology) performance depends strongly on the diffusivity (rate of exchange) of reactants (sorbates) and products (adsorbed species) between the active (adsorption) sites of the catalyst (sorbent) and the surroundings. Here, the relationship between diffusion and adsorption/reaction rates can be rationalized by the plot of effectiveness factor (η) as a function of Thiele modulus (ϕ_n), as illustrated in **Figure 1-2**a. Specifically, the larger the diffusivity is, the smaller the ϕ_n is, the faster the internal diffusion rate is. The relation between diffusivity and pore size is shown in **Figure 1-3** (reprinted from Ref.[8]). When the pore size decreases from the macroporous to microporous region, the diffusivity drops dramatically due to the molecule mobility in the pore channels. In order to optimize the density of active sites and the accessibility to the active sites (**Figure 1-4**), especially for the mass transport of large molecules, mesoporous or micro-mesoporous materials would be a better candidate for facilitating rapid mass transport of large molecules. In the case of molecular separations by microporous membranes, Fick's law underscores how the diffusion flux is inversely proportional to the membrane thickness (**Figure 1-2**b). Thus there is a desire to realize rational strategies for synthesizing ultra-thin microporous films for use as membranes capable of high-flux, high-selectivity molecular separations.

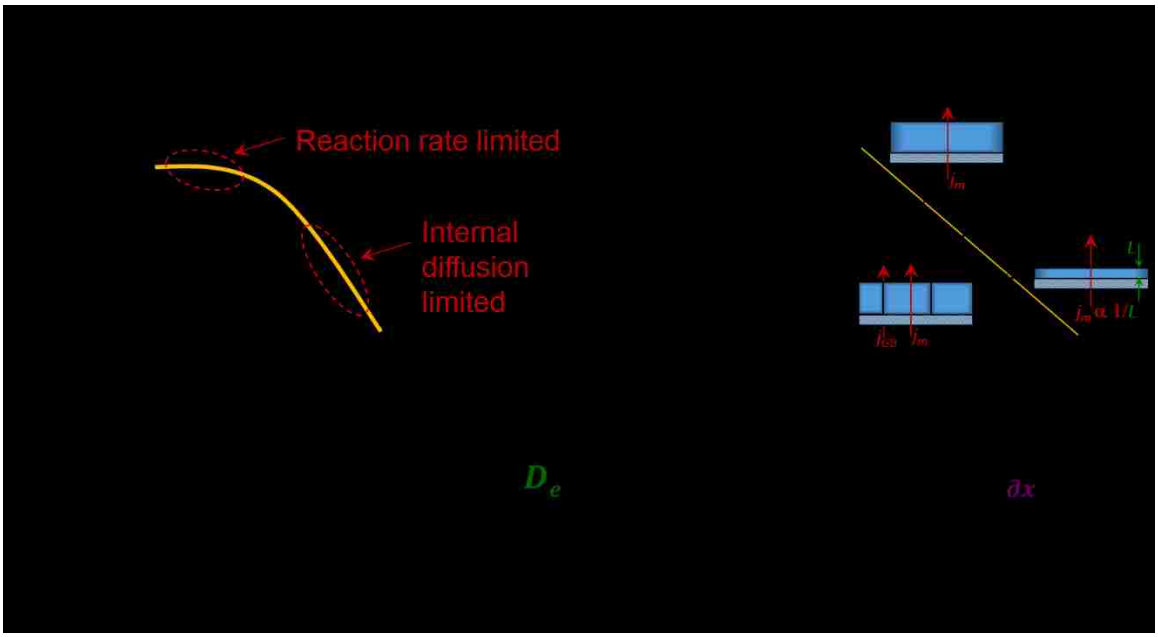

Figure 1-2. Role of diffusivity and diffusion length in separation and catalysis

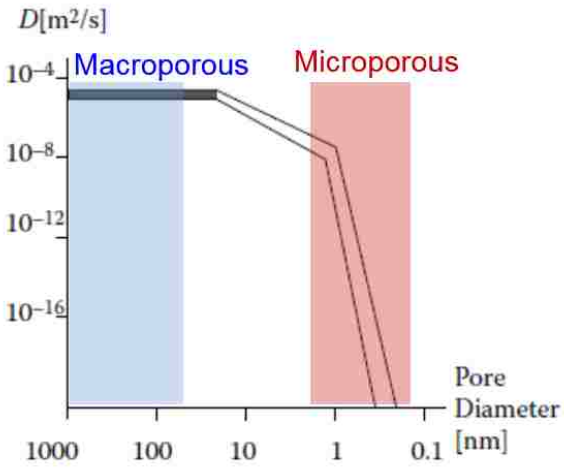

Figure 1-3. Relation between diffusivity and pore size (reprinted from Ref.[8])

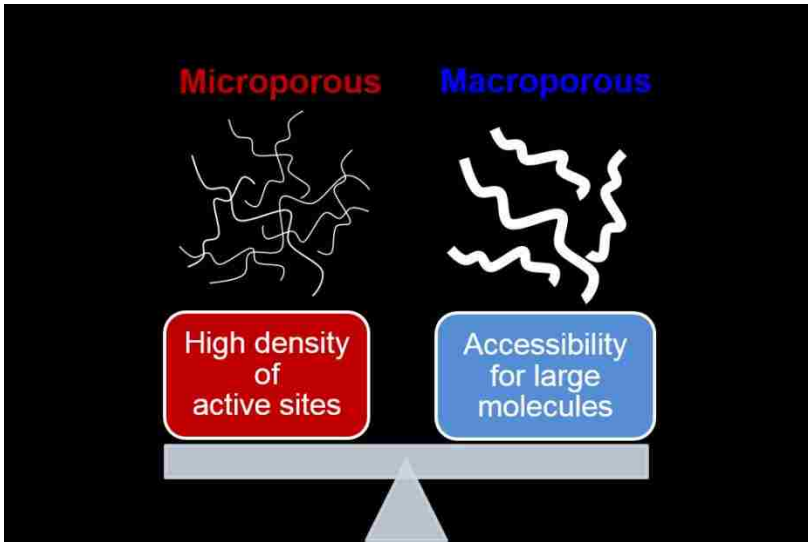

Figure 1-4. Optimum between density of active sites and accessibility for large molecules

1.1.3 Approach: Hierarchical Engineering of Porous Materials

In this thesis, we develop integrated bottom-up and top-down strategies aimed at enhancing the diffusivity and controlling the diffusion length scales in porous materials morphologies including powders/particles and thin microporous films as illustrated in **Figure 1-5**. The fabrication of mesoporous materials and incorporation of mesoporosity into microporous materials aims to enhance the diffusivity of molecules in the porous structures. Scaling down the thickness of microporous films leads to high molecular flux for small molecule separations.

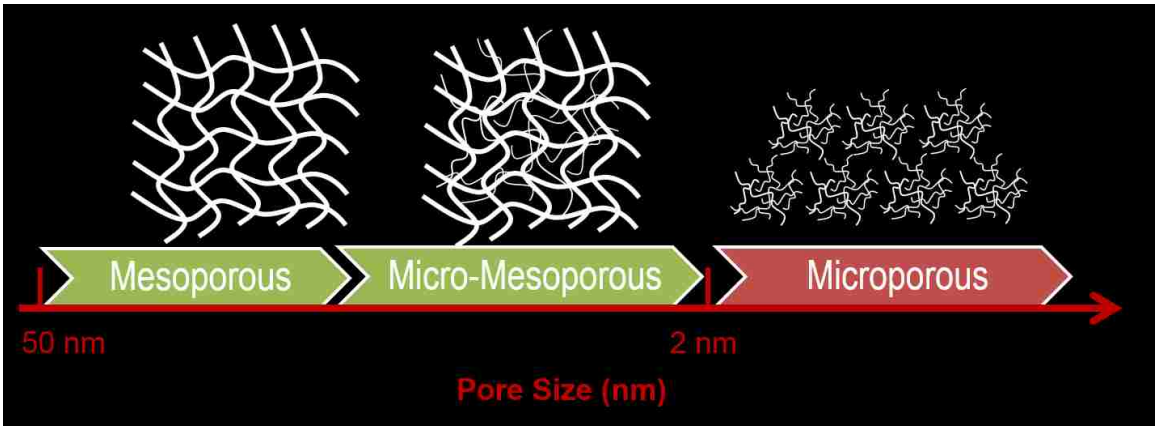

Figure 1-5. Controlling diffusion length scale of functional nanoporous materials

Specifically, we exploit a hierarchical engineering approach, which includes a bottom-up growth of multi-modal mesoporous materials, and a top-down templating of amorphous (i.e., carbon) and crystalline (i.e., zeolite) microporous materials, as schematized in **Figure 1-6**. This includes (Chapters 2-3) efforts to realize template-free ordered mesoporous silicas (OMSs) with promising properties relative to conventional surfactant-templated OMSs by bottom-up nanoparticle assembly, (Chapter 4) facile templating of a new class of hierarchically porous, three-dimensionally ordered microporous/bi-modal mesoporous carbons, and (Chapter 5) nanoscaffolding of ultra-thin zeolite films that hold potential for high-performance molecular separations.

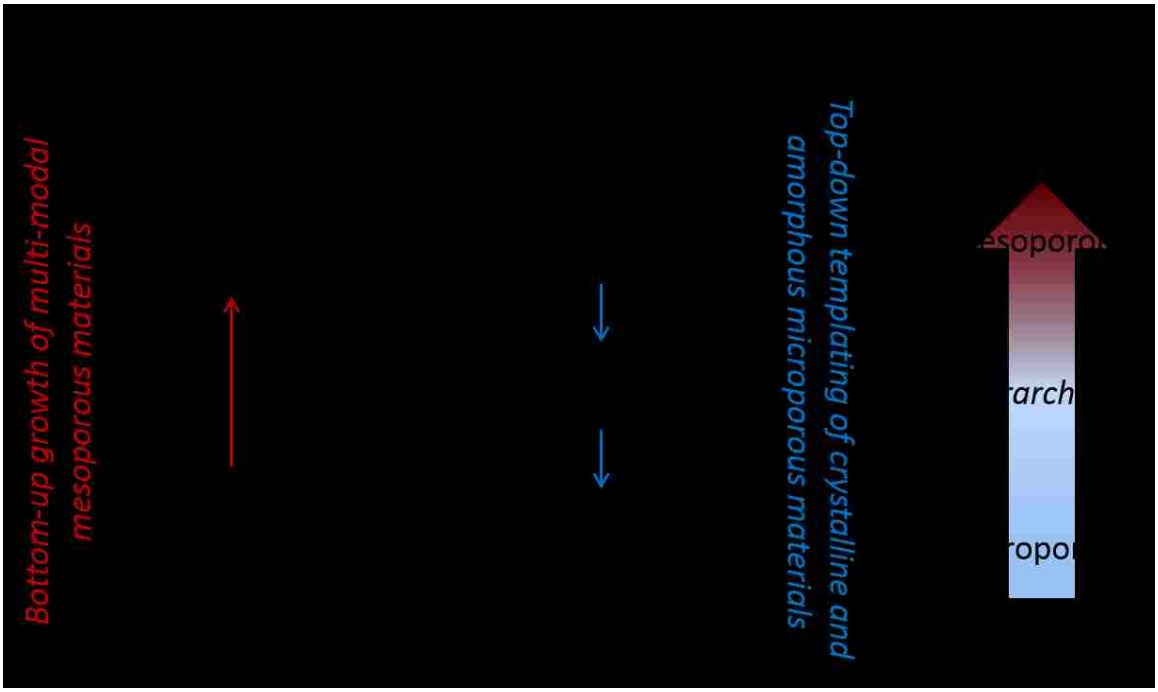

Figure 1-6. Hierarchical engineering of porous materials

1.2 Background

In order to appropriately frame the work in this thesis associated with the integrated bottom-up synthesis of mesoporous materials and top-down templating of amorphous and crystalline microporous materials, in the following sections we provide a brief background on the state-of-the-art associated with each of these material classes. In doing so, we attempt to clearly highlight *current challenges associated with facile control over material properties.*

1.2.1 Bottom-up growth of multi-modal mesoporous materials

Conventional ordered mesoporous materials are derived by an effective bottom-up strategy in which molecular precursors are co-assembled with pore-forming materials.

Specifically, the synthesis, material properties and applications of conventional ordered mesoporous silicas (OMS) will be briefly reviewed. Compared with conventional OMSs, the assembly of binary colloidal particles is an alternative route that we have specifically developed and explored in this Thesis for rational design and realization of multifunctional ordered mesoporous materials. Finally, state-of-the-art ordered mesoporous carbons (OMC) fabricated by various methods will be discussed as well.

1.2.1.1 Surfactant-templated ordered mesoporous silicas

Ordered mesoporous silicas with open framework structures were first reported in the early 1990s.[9, 10] The invention of the M41S family from Mobil, such as MCM-41, MCM-48, and MCM-50, triggered extensive research in the area of ordered mesoporous silicas.[11] Generally, the OMS synthesis involves four steps: 1) formation of assembled amphiphilic surfactants (micelles) used as templates with controllable configurations (spherical, cylindrical, cubic, and lamellar micelles), 2) cooperative self-assembly of surfactants and silica source in aqueous solution reacted between room temperature and 130 ℃, 3) hydrothermal treatment between 100 and 130 ℃, and 4) removal of templates by calcination in air/oxygen or solvent extraction. Post-synthesis treatment is occasionally needed to improve the thermal stability and regularity of mesoporous silicas by secondary synthesis and recrystallization, respectively.

The liquid-crystal mesophase of aggregated surfactants is the key factor for forming diverse micellar mesostructures, and, consequently, the ordered mesoporous silicas with different mesostructures (2D hexagonal, 3D hexagonal, 3D cubic, and bicontinuous cubic, etc.) are formed after removal of templates. Control of pore size mainly depends on the

surfactant types (cationic, anionic, and nonionic) with different hydrophobic groups in surfactants. In general, nonionic surfactants, such as PEO-PPO-PEO block copolymers, create larger pore sizes, from 4 to 20 nm, than cationic and anionic surfactants, from 2 to 7 nm. Swelling agents can be added to expand the pore sizes, but only within a limited range.[11] While OMSs provide tunable pore sizes, the size range over which the wall thickness of these materials can be tuned is quite limited.

Replication by, e.g. carbon, is often used as a means to realize more stable materials, with replica pores being templated by OMS walls. Therefore, OMS-based replica materials possess very similar pore sizes. The degree and window size of pore interconnectivity are strongly limited by the surfactants used in OMS synthesis. For example, there is *no interconnectivity* between 2D mesopore channels of MCM-41, which is templated by cationic SDAs. Instead, using nonionic block copolymers as SDAs, *disordered micropores* exist in SBA-15 to connect the mesopore channels,[12, 13] with evidence of the replica materials, such as metal oxides, metal sulfides, and carbons, remaining in the ordered 2D hexagonal mesostructures after removing the SBA-15 silicate templates.[14]

The applications of mesoporous silicas in the field of catalysis and adsorption are hampered by their amorphous nature with no catalytic active sites. Amorphous pore walls and thin wall thickness, such as in the case of MCM-41, result in limits on thermal and hydrothermal stability. It is reported that mesoporous silicas with relatively thick pore walls templated by nonionic surfactants, such as SBA-15, have relatively higher hydrothermal stability.[15] In order to improve the hydrothermal stability, much research has been done in this area, such as post-hydrothermal treatment[16, 17], increasing calcination temperature[15],

and incorporating atomic Al into the mesoporous silica materials[18-20], *but the overall catalytic performance still falls short for industrial applications.*

Catalytic activity of OMSs can be introduced by incorporating catalytically active heteroatoms or nanoparticles into the mesoporous silica materials by two methods: 1) introducing/doping heteroatoms, mainly trivalent elements (e.g. Al, B, Ga, Fe), in the preformed mesostructured frameworks, and 2) adding heteroatom or catalytic NP sources in the reaction mixture. The latter method is often preferred because of potential for homogeneous distribution of the heteroatoms.[6] However, while incorporating the heteroatoms, several deleterious effects converge, such as reduced long-range structural ordering, and decreased pore volume and average pore size.[21, 22] Migration-coalescence and/or Ostwald ripening of the heteroatoms between adjacent pores of OMS will be another issue on catalytic performance.[23]

In summary, key challenges faced with OMSs for practical applications include:

1) *Limited tunability of wall thickness*
2) *No or disordered microporous interconnectivity between the mesopore bodies*
3) *Low thermal and hydrothermal stability due to thin pore wall thickness*
4) *Instability of catalytic NPs in OMS mesostructures*

1.2.1.2 Assembly of uni- and multi- modal nanoparticles

While the surfactant-directed OMSs have been studied for quite some time, other 3D ordered mesoporous materials, which are not thought of as conventional ordered mesoporous materials, can be realized by bottom-up nanoparticle assembly, i.e. 3D ordered

colloidal crystals. 3D ordered colloidal crystals have been attractive in the past two decades due to their potential applications in photonics[24], catalysis[25], lithography[26], and sensing.[27] These ordered structures are comprised of close-packed particles, with the degree of ordering related, in part, to the narrowness of the particle size distribution. The interstitial spacing between particles in colloidal crystals is controlled by the size of the primary particles. Thus, assemblies of nanoparticles can yield three-dimensionally ordered micro- and meso-porous materials with corresponding pores of less than 2 nm and between 2-50 nm, respectively. The 3D pore structures within close-packed colloidal crystal structures are composed of tetrahedrally and octahedrally coordinated pore bodies, as illustrated in **Figure 1-7**.

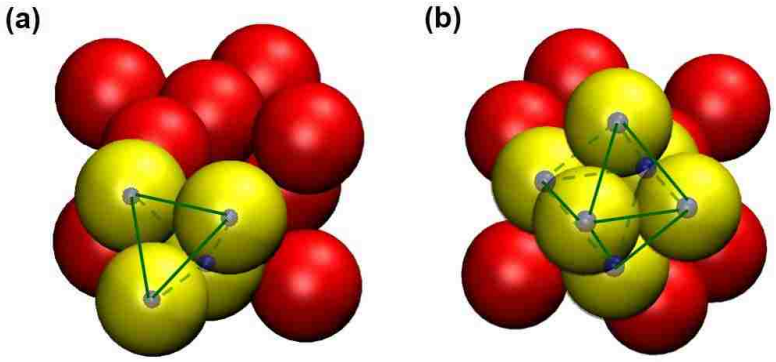

Figure 1-7. 3D pore structures within close-packed colloidal crystal structures. Tetrahedral pore (a), and octahedral pore (b)

When populations of particles of distinctly different size or complementary function are co-assembled, highly ordered multi-modal particle assemblies can be realized. The resulting so-called binary colloidal crystals increase the level of diversity of both the crystal structure and the resulting pore topology (interstices), and, thus, provide additional handles for tuning porosity, pore topology, and pore coordination for practical applications

such as 3D photonic crystals with full photonic bandgaps (PBGs)[28] and fundamental crystallography studies.[29] *What has been less explored to date is how this 3D particle assembly could be exploited as a means for realizing template-free, 3D-ordered mesoporous materials potentially suitable even for shape- and size-selective sorbents and catalysts capable of selectively accommodating bulky molecules.*

The majority of efforts reported on binary colloidal crystals to date have been divided into two regimes. One is assembly of nanoscale metal and/or metal oxide particles sterically stabilized by capping organic surfactants in organic solvent. More than 15 different binary nanoparticle superlattice (BNSL) structures[30] have been identified recently with factors controlling the diverse BNSL structures[31, 32] including size ratio, temperature, and ligand shell interactions. The other regime is assembly of micron and sub-micron scale primary particles, such as polystyrene (PS), polymethylmethacrylate (PMMA) and silica particles. In this regime, studies have thoroughly investigated the role of particle size over moderate to large size ratios (i.e, the largest size ratios coming from mixtures of sub-micron and nanoscale particles), particle number ratios, and surface chemistry of both particles and substrates in the formation of binary colloidal crystals. In addition, inverse opal structures using binary colloidal crystals as hard templates have also been widely studied at the micron and sub-micron scale.[33-41]

In binary silica particle assembly, dramatic scaling down of colloidal crystal component size to particles on the order of 10 nm holds promise for realizing novel mesoporous and even microporous materials. Recently, binary silica nanoparticle assembly in bulk form isostructural with AlB_2 (26/51 nm) and $NaZn_{13}$ (19/35 nm) was reported.[42] However, to our best knowledge, a comprehensive experimental study of

structural diversity of binary silica nanoparticle assemblies has not been reported elsewhere and the fundamental underpinnings of the binary assembly phenomenon have not been fully elucidated.

Assembly of template-free 3D-ordered binary silica nanoparticle superlattices not only opens a new window for realizing multi-functional 3D-interconnected ordered mesoporous silica materials, but establishes a model system for further fundamental crystallographic study.

1.2.1.3 Conventional hard- and soft-templated ordered mesoporous carbons

Another type of porous material, porous carbon, has potential applications spanning adsorption[34, 43, 44], energy conversion and storage[45-48], catalysis[49-51], and electrodes[52, 53] owing to its chemical and mechanical stability, corrosion resistance and electrical conductivity. Among various porous carbon materials, ordered mesoporous carbons (OMCs), with well-defined porosity and pore topology along with high surface areas and pore volumes, hold the potential for practical applications involving large guest molecules[54-59].

Conventionally, ordered mesoporous carbons (OMCs) are synthesized by using surfactant-templated ordered mesoporous silicas (OMSs) as the hard templates[14, 55, 60-63], generally including four major steps: 1) synthesis of OMSs by surfactant-templating methods, 2) infiltration of carbon precursor into the meso- and/or micropores of the OMS, 3) polymerization and carbonization of infiltrated carbon precursor, and 4) removal of the OMS template. The mesopores in carbon replicas are templated by the OMS walls, which

are a few nanometers thick and difficult to tune in size, leading to limited control over pore sizes of OMCs of less than 5 nm[64, 65].

As an alternative to hard-templating methods, the soft-templating method to fabricate OMCs, which is similar to surfactant-templated OMS synthesis, is commonly exploited. The one-pot evaporation-induced co-assembly of amphiphilic surfactants (soft templates) and phenolic resins (carbon precursors)[66-68] offers a facile way to synthesize OMCs by simply carbonizing the polymer framework and remove the surfactant templates, with the tunability of pore sizes up to 15nm. However, during the pyrolysis process, high pore shrinkage and/or pore collapse were reported due to the thermal instability of the polymer framework, which hampered this soft-templating method for practical applications[45].

In addition to the pore size control of OMCs, incorporation of secondary mesoporosity in porous carbons hold the potential to improve the accessibility and pore connections of porous carbons which is favorable for practical applications, especially for large-molecule mass transport, by using dual hard-templates[69-72], soft-templates[73], agglomerate of silica templates[74, 75], and partial filling of carbon precursors[76-79]. However, the tunability of pore sizes and pore interconnectivity are still quite limited by using these methods with complex synthesis procedures.

In summary, key challenges faced with conventional OMCs include:

1) *Limited tunability of unary and/or binary mesopores*
2) *Limited 3D-ordered pore interconnectivity between mesopores*
3) *Complicated and/or costly synthesis procedures*

A facile method to fabricate three-dimensionally ordered multimodal mesoporous carbons with controllable pore topology, independently tunable mesopore sizes and three-dimensionally interconnected pore bodies is needed to enhance the performance of porous carbons for practical applications.

1.2.2 Top-down templating of crystalline microporous materials

As discussed previously, zeolitic materials represent a different class of nanoporous materials than OMSs owing to their crystallinity and pores of less than 2 nm in diameter. Zeolites are microporous crystalline aluminosilicates that have been employed in applications such as separations, catalysis, adsorption, and ion exchange[80, 81]. More than 200 different zeolite frameworks (i.e., different pore topologies and primary pore sizes) exist, with numerous studies for membrane applications including separations of small gases (e.g., CO_2, H_2, CH_4, etc.), isomeric aromatics and alkanes (e.g., *o*-/*p*-xylenes, butanes), and water/alcohol pervaporations, among others.[82-85]

Over the past several decades, considerable research effort has focused on the fabrication of zeolite membranes with potential for liquid or gas separations, owing to their potential as attractive alternatives to current energy-intensive and costly separation processes such as distillation, fractional crystallization, and others.[86-89] Compared with polymeric films, inorganic zeolite membranes are chemically, thermally and mechanically stable, and hold promise for high-resolution selectivity and high flux for gas or liquid separations.

Conventionally, *in situ* growth[86, 90] is an easy one-step synthesis method to form zeolite membranes on porous supports, but it is not an ideal method to fabricate high performance zeolite membranes because of the large film thickness caused by a low nucleation site density and undesired penetration of synthesis mixture into the porous support. Secondary seeded growth[80, 81, 91-95], which decouples nucleation from crystal growth, is the current state-of-the-art technique on a laboratory scale. It comprises three subprocesses: 1) preparation of a colloidal suspension of precisely shaped zeolite particles,

2) deposition of zeolite particles serving as seed layer on a porous support, and 3) secondary growth of the zeolite particles to form a continuous film.

A large membrane thickness, however, results upon sufficient secondary growth to realize continuous membranes. Specifically, these *large membrane thicknesses* are due, in part, to *multi-dimensional growth of large seed crystals* (i.e., both in plane and out-of-plane growth) until continuous polycrystalline films are realized. It is one of the key factors limiting the performance of these zeolite membranes for practical membrane applications, given the stringent industrial demands for simultaneous realization of high selectivity and high flux. In order to realize industrially relevant fluxes, efforts to reduce membrane thickness, and thereby diffusion length scale, have focused until very recently on the synthesis of preferentially oriented and/or smaller seed crystals for secondary seeded growth.

Secondary hydrothermal growth, however, is required to seal interstitial spaces between adjacent single crystal structures within the seed layer for realization of dense oriented membranes. Efforts to minimize the resulting film thickness, derived from fast out-of-plane zeolite growth and slower in-plane growth, have commonly employed expensive customized structure-directing agents[80, 91, 96] or complex synthesis procedures[97-100].

As an alternative to molecular-scale structure direction, physical confinement of zeolite crystal growth has been successfully demonstrated to lead to mesopore-imprinted zeolite single crystals[101, 102] comprised of nanosized zeolite particles[101, 103, 104]. Dispersion and deposition of the templated zeolite nanoparticles as primary seeds for subsequent secondary film growth has been employed as a possible approach to realizing thin zeolite

films. More recent efforts to scale down membrane thickness have exploited nanosized zeolite crystals or exfoliated zeolite nanosheets as the seed crystals primary precursors for secondary film growth.[105-107] All of these innovative research results demonstrated the implications for realizing a new, continuous zeolite membrane with better separation performance, but need still exists for facile synthesis procedures with high cost-performance value

In summary, commercialization of current state-of-the-art zeolite membranes for gas or liquid separations encounters several challenges including:

1) Insufficient performance caused by the large film thickness and the defects such as cracks and grain boundaries

2) High cost and difficulties in scale up attributed to the complicated and unreliable manufacturing processes.

A top-down scaffolding of zeolite crystal growth in pre-formed 3D ordered mesoporous carbon films of controllable film thickness on the order of 10-100 nm stands to address the above challenges.

1.3 Outlines

Chapter 2

In Chapter 2, evaporation-induced convective binary assembly of large (A) and small (B) silica nanoparticles is demonstrated as a template-free route to three-dimensionally ordered mesoporous silicas (OMSs), the pore topology of which derives from the interconnected interstices of the resulting ordered nanoparticulate structures. Even without explicit solvent index matching or stabilization (e.g., charge or steric) beyond intrinsic properties of the amino acid nanoparticle synthesis solution, assembly of binary mixtures of silica nanoparticles of ca. 10-50 nm in diameter primarily obeys hard-sphere phase behavior despite differences in electrostatic character of the particles. Specifically, the particle size ratio, γ, governs symmetry of the assemblies among AB_2 and AB_{13} phases, and enables access of the AB phase. Small-angle X-ray scattering (SAXS) reveals the high-yield of ordered binary assemblies, and confirms, in combination with transmission electron microscopy, the AlB_2, $NaZn_{13}$, and NaCl crystalline isostructures. Interstitial solid solutions result for the smallest γ considered ($\gamma \leq 0.3$), wherein cubic crystallization of the large particles is templated by interstitially mobile small particles. New mechanistic insight into factors influencing the yield of ordered binary structures includes the degree to which the smaller particles (ca. 15-24 nm) within the mixture undergo unary crystallization, as influenced by lysine or other basic amino acids used in the nanoparticle synthesis, as well as matching of the time scales for convective nanoparticle assembly and crystallization. Ultimately, the demonstrated robustness of the binary nanoparticle assembly and the control over silica particle size translates to a facile, template-free approach to OMSs with independently tunable pore topology and pore size.

Chapter 3

Continuing the work in Chapter 2, we further investigated the effect of composition of Lys-Sil sols and the role of electrostatic forces on colloidal assembly of silica nanoparticles, revealing that destabilization of the silica particles within the binary mixture by removal of solvated amino acids via dialysis can lead to destruction of the crystallinity of the binary assembly even if the silica particles remain colloidally stable after dialysis and can assemble on their own into unary nanoparticle crystals. Simple replenishment of lysine (or arginine) re-establishes the ordered binary phase behavior. Yet, so also does the introduction of NaOH for titration of the sol pH back to that consistent with the buffering action of Lysine (and arginine). This seems to imply that the ability to realize binary silica nanoparticle assemblies may be less contingent upon lysine (or arginine) as a steric stabilizer, and more a result electrostatic forces to counterbalance van der Waals forces such that entropic effects, and thus hard sphere phase behavior, dominate the Lys-Sil binary assembly.

We also identify transient stability of the system upon aging, correlating changes in the stability of the smallest particles, marked by disordered aggregation in the unary system, with molecular-scale evolution of the silica network owing possibly to water diffusion and association with internal siloxane bonds and silanol groups. Additionally, sensitivities of the binary assembly to the substrate upon which they are formed are identified and investigated, with implications in translation of bulk binary assembly to binary thin films. Convective assembly of silica sols on the substrates with low and high surface energy was carried out showing disordered binary silica structures, which indicated that matching the rates of particle assembly and evaporation as well as the interaction forces

between particle and substrate will play an important role to realize large-scale ordered binary silica films.

Chapter 4

In this chapter, a facile method to synthesize a new class of bimodal three-dimensionally ordered micro-mesoporous (b-3DOm) carbons with tunable bimodal, 3D-interconnected mesopores is demonstrated. Template-free ordered mesoporous silicas (OMSs) prepared by bottom-up evaporation-induced convective assembly of binary silica nanoparticles (i.e., Chapters 2 and 3) are used as hard sacrificial templates to synthesize b-3DOm carbon replicas. Continuously adjustable bimodal mesoporosity in the range of 15-23 nm for small pores and 40-50 nm for large pores with controlled pore topology isostructural with NaCl, AlB_2, and $NaZn_{13}$ are confirmed by TEM, and 2D-SAXS analysis. The textural properties including high surface areas (>1000 m^2/g), narrow pore size distributions, and large and tunable pore volumes (2-5 cm^3/g) are estimated from nitrogen physisorption analysis. The ability to finely and independently control mesopore size, interconnectivity, and topology within ordered porous carbons should prove critical in the rational design of these materials for applications spanning catalysis, adsorption, and even batteries.

Chapter 5

Motivated by the need to develop methods for facilitating in-plane over out-of-plane growth of zeolite films, this chapter exploits materials discussed in earlier chapters for the top-down templating of crystalline microporous thin films. Namely, we develop an approach that employs three-dimensionally ordered mesoporous (3DOm) carbon films of

tunable thickness down to tens of nanometers as scaffolds for confined crystal growth of ultra-thin zeolite films. Confined growth techniques using 40 nm 3DOm carbon films as templates have been successfully exploited to synthesize not only micron-sized domains of silicalite-1 crystals, but large silicalite-1 crystal regions formed by intergrowth of separately nucleated crystal domains, which are characterized by SEM, TEM and XRD. The thickness of the silicalite-1 domains can be tuned and scaled down to the order of 10 nm by controlling the carbon scaffold thickness. The flexibility of these brittle inorganic thin films was observed. The morphology of silicalite-1 domains, from micron-sized silicalite-1 domains to continuous films, can be controlled by zeolite synthesis time during hydrothermal growth. This confined crystal growth of thin zeolite films holds potential for realization of high flux, high-selectivity microporous zeolite membranes.

Chapter 6

We conclude the thesis with a critical summary of new insights established herein for realizing multimodal ordered mesoporous silicas and carbons by bottom-up colloidal assembly strategies, and ultra-thin zeolite films by top-down hard-templating methods. We also discuss concepts and even proof-of-concept data for future work. This includes further extension of strategies established in this thesis for realizing novel multi-functional porous materials including structurally diverse ordered mesoporous silicas, and compositionally diverse binary metal/silica nanoparticle assembly. In addition, we highlight the future potential for bimodal ordered mesoporous carbons templated by binary OMSs discussed in Chapter 2.

1.4 Reference

1. Corma, A., From microporous to mesoporous molecular sieve materials and their use in catalysis. *Chem. Rev.* **1997,** 97, (6), 2373-2419.

2. Barton, T. J.; Bull, L. M.; Klemperer, W. G.; Loy, D. A.; McEnaney, B.; Misono, M.; Monson, P. A.; Pez, G.; Scherer, G. W.; Vartuli, J. C.; Yaghi, O. M., Tailored porous materials. *Chemistry of Materials* **1999,** 11, (10), 2633-2656.

3. Ciesla, U.; Schuth, F., Ordered mesoporous materials. *Microporous and Mesoporous Materials* **1999,** 27, (2-3), 131-149.

4. Davis, M. E., Ordered porous materials for emerging applications. *Nature* **2002,** 417, (6891), 813-821.

5. Schuth, F., Engineered porous catalytic materials. In *Annual Review of Materials Research*, Annual Reviews: Palo Alto, 2005; Vol. 35, pp 209-238.

6. Perego, C.; Millini, R., Porous materials in catalysis: challenges for mesoporous materials. *Chemical Society Reviews* **2013,** 42, (9), 3956-3976.

7. Wang, S. B., Ordered mesoporous materials for drug delivery. *Microporous and Mesoporous Materials* **2009,** 117, (1-2), 1-9.

8. Roque-Malherbe, R. M. A., *Adsorption and Diffusion in Nanoporous Materials*. CRC Press: 2007.

9. Beck, J. S.; Vartuli, J. C.; Roth, W. J.; Leonowicz, M. E.; Kresge, C. T.; Schmitt, K. D.; Chu, C. T. W.; Olson, D. H.; Sheppard, E. W.; McCullen, S. B.; Higgins, J. B.; Schlenker, J. L., A new family of mesoporous molecular-sieves prepared with liquid-crystal templates. *Journal of the American Chemical Society* **1992,** 114, (27), 10834-10843.

10. Yanagisawa, T.; Shimizu, T.; Kuroda, K.; Kato, C., The preparation of alkyltrimethylammonium-kanemite complexes and their conversion to microporous materials. *Bulletin of the Chemical Society of Japan* **1990,** 63, (4), 988-992.

11. Wan, Y.; Zhao, D. Y., On the controllable soft-templating approach to mesoporous silicates. *Chem. Rev.* **2007,** 107, (7), 2821-2860.

12. Joo, S. H.; Ryoo, R.; Kruk, M.; Jaroniec, M., Evidence for general nature of pore interconnectivity in 2-dimensional hexagonal mesoporous silicas prepared using block copolymer templates. *Journal of Physical Chemistry B* **2002,** 106, (18), 4640-4646.

13. Lukens, W. W.; Schmidt-Winkel, P.; Zhao, D. Y.; Feng, J. L.; Stucky, G. D., Evaluating pore sizes in mesoporous materials: A simplified standard adsorption method and a simplified Broekhoff-de Boer method. *Langmuir* **1999,** 15, (16), 5403-5409.

14. Ryoo, R.; Joo, S. H.; Jun, S., Synthesis of highly ordered carbon molecular sieves via template-mediated structural transformation. *Journal of Physical Chemistry B* **1999,** 103, (37), 7743-7746.

15. Zhang, F. Q.; Yan, Y.; Yang, H. F.; Meng, Y.; Yu, C. Z.; Tu, B.; Zhao, D. Y., Understanding effect of wall structure on the hydrothermal stability of mesostructured silica SBA-15. *Journal of Physical Chemistry B* **2005,** 109, (18), 8723-8732.

16. Mokaya, R., Hydrothermally stable restructured mesoporous silica. *Chemical Communications* **2001**, (10), 933-934.

17. Chen, L. Y.; Horiuchi, T.; Mori, T.; Maeda, K., Postsynthesis hydrothermal restructuring of M41S mesoporous molecular sieves in water. *Journal of Physical Chemistry B* **1999,** 103, (8), 1216-1222.

18. Pauly, T. R.; Petkov, V.; Liu, Y.; Billinge, S. J. L.; Pinnavaia, T. J., Role of framework sodium versus local framework structure in determining the hydrothermal stability of MCM-41 mesostructures. *Journal of the American Chemical Society* **2002,** 124, (1), 97-103.

19. O'Neil, A. S.; Mokaya, R.; Poliakoff, M., Supercritical fluid-mediated alumination of mesoporous silica and its beneficial effect on hydrothermal stability. *Journal of the American Chemical Society* **2002,** 124, (36), 10636-10637.

20. Zhang, Z. T.; Han, Y.; Zhu, L.; Wang, R. W.; Yu, Y.; Qiu, S. L.; Zhao, D. Y.; Xiao, F. S., Strongly acidic and high-temperature hydrothermally stable mesoporous aluminosilicates with ordered hexagonal structure. *Angewandte Chemie-International Edition* **2001,** 40, (7), 1258-+.

21. Mokaya, R., Al content dependent hydrothermal stability of directly synthesized aluminosilicate MCM-41. *Journal of Physical Chemistry B* **2000,** 104, (34), 8279-8286.

22. Occelli, M. L.; Biz, S.; Auroux, A.; Ray, G. J., Effects of the nature of the aluminum source on the acidic properties of some mesostructured materials. *Microporous and Mesoporous Materials* **1998,** 26, (1-3), 193-213.

23. Yu, N. Y.; Ding, Y.; Lo, A. Y.; Huang, S. J.; Wu, P. H.; Liu, C.; Yin, D. H.; Fu, Z. H.; Yin, D. L.; Hung, C. T.; Lei, Z. B.; Liu, S. B., Gold nanoparticles supported on periodic mesoporous organosilicas for epoxidation of olefins: Effects of pore architecture and surface modification method of the supports. *Microporous and Mesoporous Materials* **2011,** 143, (2-3), 426-434.

24. Bardosova, M.; Pemble, M. E.; Povey, I. M.; Tredgold, R. H., The Langmuir-Blodgett Approach to Making Colloidal Photonic Crystals from Silica Spheres. *Adv. Mater.* **2010,** 22, (29), 3104-3124.

25. Yuan, Z. Y.; Su, B. L., Insights into hierarchically meso-macroporous structured materials. *J. Mater. Chem.* **2006,** 16, (7), 663-677.

26. Evers, W. H.; De Nijs, B.; Filion, L.; Castillo, S.; Dijkstra, M.; Vanmaekelbergh, D., Entropy-Driven Formation of Binary Semiconductor-Nanocrystal Superlattices. *Nano Lett.* **2010,** 10, (10), 4235-4241.

27. Mukhopadhyay, R.; Al-Hanbali, O.; Pillai, S.; Hemmersam, A. G.; Meyer, R. L.; Hunter, A. C.; Rutt, K. J.; Besenbacher, F.; Moghimi, S. M.; Kingshott, P., Ordering of binary polymeric nanoparticles on hydrophobic surfaces assembled from low volume fraction dispersions. *Journal of the American Chemical Society* **2007,** 129, (44), 13390-+.

28. Dai, Z. F.; Li, Y.; Duan, G. T.; Jia, L. C.; Cai, W. P., Phase Diagram, Design of Monolayer Binary Colloidal Crystals, and Their Fabrication Based on Ethanol-Assisted Self-Assembly at the Air/Water Interface. *Acs Nano* **2012,** 6, (8), 6706-6716.

29. Vermolen, E. C. M.; Kuijk, A.; Filion, L. C.; Hermes, M.; Thijssen, J. H. J.; Dijkstra, M.; van Blaaderen, A., Fabrication of large binary colloidal crystals with a NaCl structure. *Proc. Natl. Acad. Sci. U. S. A.* **2009,** 106, (38), 16063-16067.

30. Shevchenko, E. V.; Talapin, D. V.; Murray, C. B.; O'Brien, S., Structural characterization of self-assembled multifunctional binary nanoparticle superlattices. *Journal of the American Chemical Society* **2006,** 128, (11), 3620-3637.

31. Chen, Z.; O'Brien, S., Structure direction of II-VI semiconductor quantum dot binary nanoparticle superlattices by tuning radius ratio. *Acs Nano* **2008,** 2, (6), 1219-1229.

32. Chen, Z. Y.; Moore, J.; Radtke, G.; Sirringhaus, H.; O'Brien, S., Binary nanoparticle superlattices in the semiconductor-semiconductor system: CdTe and CdSe. *Journal of the American Chemical Society* **2007,** 129, (50), 15702-15709.

33. Vogel, N.; de Viguerie, L.; Jonas, U.; Weiss, C. K.; Landfester, K., Wafer-Scale Fabrication of Ordered Binary Colloidal Monolayers with Adjustable Stoichiometries. *Advanced Functional Materials* **2011,** 21, (16), 3064-3073.

34. Wu, Z. X.; Webley, P. A.; Zhao, D. Y., Comprehensive Study of Pore Evolution, Mesostructural Stability, and Simultaneous Surface Functionalization of Ordered Mesoporous Carbon (FDU-15) by Wet Oxidation as a Promising Adsorbent. *Langmuir* **2010,** 26, (12), 10277-10286.

35. Detrich, A.; Deak, A.; Hild, E.; Kovacs, A. L.; Horvolgyi, Z., Langmuir and Langmuir-Blodgett Films of Bidisperse Silica Nanoparticles. *Langmuir* **2010,** 26, (4), 2694-2699.

36. Wang, L. K.; Wan, Y.; Li, Y. Q.; Cai, Z. Y.; Li, H. L.; Zhao, X. S.; Li, Q., Binary Colloidal Crystals Fabricated with a Horizontal Deposition Method. *Langmuir* **2009,** 25, (12), 6753-6759.

37. Wang, J. J.; Li, Q.; Knoll, W.; Jonas, U., Preparation of multilayered trimodal colloid crystals and binary inverse opals. *Journal of the American Chemical Society* **2006,** 128, (49), 15606-15607.

38. Kim, M. H.; Im, S. H.; Park, O. O., Rapid fabrication of two- and three-dimensional colloidal crystal films via confined convective assembly. *Advanced Functional Materials* **2005,** 15, (8), 1329-1335.

39. Cong, H. L.; Cao, W. X., Array patterns of binary colloidal crystals. *Journal of Physical Chemistry B* **2005,** 109, (5), 1695-1698.

40. Bartlett, P.; Campbell, A. I., Three-dimensional binary superlattices of oppositely charged colloids. *Phys. Rev. Lett.* **2005,** 95, (12), 4.

41. Kitaev, V.; Ozin, G. A., Self-assembled surface patterns of binary colloidal crystals. *Adv. Mater.* **2003,** 15, (1), 75-+.

42. Kuroda, Y.; Sakamoto, Y.; Kuroda, K., Selective Cleavage of Periodic Mesoscale Structures: Two-Dimensional Replication of Binary Colloidal Crystals into Dimpled Gold Nanoplates. *Journal of the American Chemical Society* **2012,** 134, (20), 8684-8692.

43. Zhuang, X.; Wan, Y.; Feng, C. M.; Shen, Y.; Zhao, D. Y., Highly Efficient Adsorption of Bulky Dye Molecules in Wastewater on Ordered Mesoporous Carbons. *Chemistry of Materials* **2009,** 21, (4), 706-716.

44. Vinu, A.; Miyahara, M.; Sivamurugan, V.; Mori, T.; Ariga, K., Large pore cage type mesoporous carbon, carbon nanocage: a superior adsorbent for biomaterials. *J. Mater. Chem.* **2005,** 15, (48), 5122-5127.

45. Zhai, Y. P.; Dou, Y. Q.; Zhao, D. Y.; Fulvio, P. F.; Mayes, R. T.; Dai, S., Carbon Materials for Chemical Capacitive Energy Storage. *Adv. Mater.* **2011,** 23, (42), 4828-4850.

46. Li, Y.; Fu, Z. Y.; Su, B. L., Hierarchically Structured Porous Materials for Energy Conversion and Storage. *Advanced Functional Materials* **2012,** 22, (22), 4634-4667.

47. Nishihara, H.; Kyotani, T., Templated Nanocarbons for Energy Storage. *Adv. Mater.* **2012,** 24, (33), 4473-4498.

48. Wang, J. C.; Kaskel, S., KOH activation of carbon-based materials for energy storage. *J. Mater. Chem.* **2012,** 22, (45), 23710-23725.

49. Chai, G. S.; Yoon, S. B.; Yu, J. S.; Choi, J. H.; Sung, Y. E., Ordered porous carbons with tunable pore sizes as catalyst supports in direct methanol fuel cell. *Journal of Physical Chemistry B* **2004,** 108, (22), 7074-7079.

50. Shao, Y. Y.; Sui, J. H.; Yin, G. P.; Gao, Y. Z., Nitrogen-doped carbon nanostructures and their composites as catalytic materials for proton exchange membrane fuel cell. *Appl Catal B-Environ* **2008,** 79, (1-2), 89-99.

51. Zhang, S. L.; Chen, L.; Zhou, S. X.; Zhao, D. Y.; Wu, L. M., Facile Synthesis of Hierarchically Ordered Porous Carbon via in Situ Self-Assembly of Colloidal Polymer and Silica Spheres and Its Use as a Catalyst Support. *Chemistry of Materials* **2010,** 22, (11), 3433-3440.

52. Chaudhari, S.; Kwon, S. Y.; Yu, J. S., Ordered multimodal porous carbon with hierarchical nanostructure as high performance electrode material for supercapacitors. *Rsc Advances* **2014,** 4, (73), 38931-38938.

53. Xie, K.; Qin, X. T.; Wang, X. Z.; Wang, Y. N.; Tao, H. S.; Wu, Q.; Yang, L. J.; Hu, Z., Carbon Nanocages as Supercapacitor Electrode Materials. *Adv. Mater.* **2012,** 24, (3), 347-+.

54. Ryoo, R.; Joo, S. H.; Kruk, M.; Jaroniec, M., Ordered mesoporous carbons. *Adv. Mater.* **2001,** 13, (9), 677-681.

55. Lee, J.; Kim, J.; Hyeon, T., Recent progress in the synthesis of porous carbon materials. *Adv. Mater.* **2006,** 18, (16), 2073-2094.

56. Xing, W.; Qiao, S. Z.; Ding, R. G.; Li, F.; Lu, G. Q.; Yan, Z. F.; Cheng, H. M., Superior electric double layer capacitors using ordered mesoporous carbons. *Carbon* **2006,** 44, (2), 216-224.

57. Deng, Y. H.; Yu, T.; Wan, Y.; Shi, Y. F.; Meng, Y.; Gu, D.; Zhang, L. J.; Huang, Y.; Liu, C.; Wu, X. J.; Zhao, D. Y., Ordered mesoporous silicas and carbons with large accessible pores templated from amphiphilic diblock copolymer poly(ethylene oxide)-b-polystyrene. *Journal of the American Chemical Society* **2007,** 129, (6), 1690-1697.

58. Ndamanisha, J. C.; Guo, L. P., Ordered mesoporous carbon for electrochemical sensing: A review. *Analytica Chimica Acta* **2012,** 747, 19-28.

59. Schuster, J.; He, G.; Mandlmeier, B.; Yim, T.; Lee, K. T.; Bein, T.; Nazar, L. F., Spherical Ordered Mesoporous Carbon Nanoparticles with High Porosity for Lithium-Sulfur Batteries. *Angewandte Chemie-International Edition* **2012,** 51, (15), 3591-3595.

60. Jun, S.; Joo, S. H.; Ryoo, R.; Kruk, M.; Jaroniec, M.; Liu, Z.; Ohsuna, T.; Terasaki, O., Synthesis of new, nanoporous carbon with hexagonally ordered mesostructure. *Journal of the American Chemical Society* **2000,** 122, (43), 10712-10713.

61. Lee, J.; Yoon, S.; Oh, S. M.; Shin, C. H.; Hyeon, T., Development of a new mesoporous carbon using an HMS aluminosilicate template. *Adv. Mater.* **2000,** 12, (5), 359-+.

62. Lee, J.; Han, S.; Hyeon, T., Synthesis of new nanoporous carbon materials using nanostructured silica materials as templates. *J. Mater. Chem.* **2004,** 14, (4), 478-486.

63. Lu, A. H.; Schuth, F., Nanocasting: A versatile strategy for creating nanostructured porous materials. *Adv. Mater.* **2006,** 18, (14), 1793-1805.

64. Kruk, M.; Jaroniec, M.; Ryoo, R.; Joo, S. H., Characterization of ordered mesoporous carbons synthesized using MCM-48 silicas as templates. *Journal of Physical Chemistry B* **2000,** 104, (33), 7960-7968.

65. Lee, J. S.; Joo, S. H.; Ryoo, R., Synthesis of mesoporous silicas of controlled pore wall thickness and their replication to ordered nanoporous carbons with various pore diameters. *Journal of the American Chemical Society* **2002,** 124, (7), 1156-1157.

66. Liang, C. D.; Li, Z. J.; Dai, S., Mesoporous carbon materials: Synthesis and modification. *Angewandte Chemie-International Edition* **2008,** 47, (20), 3696-3717.

67. Chuenchom, L.; Kraehnert, R.; Smarsly, B. M., Recent progress in soft-templating of porous carbon materials. *Soft Matter* **2012,** 8, (42), 10801-10812.

68. Ma, T. Y.; Liu, L.; Yuan, Z. Y., Direct synthesis of ordered mesoporous carbons. *Chemical Society Reviews* **2013,** 42, (9), 3977-4003.

69. Gierszal, K. P.; Jaroniec, M., Novel pitch-based carbons with bimodal distribution of uniform mesopores. *Chemical Communications* **2004**, (22), 2576-2577.

70. Pang, J. B.; Hu, Q. Y.; Wu, Z. W.; Hampsey, J. E.; He, J. B.; Lu, Y. F., Direct synthesis of unimodal and bimodal nanoporous carbon. *Microporous and Mesoporous Materials* **2004,** 74, (1-3), 73-78.

71. Lee, H. I.; Pak, C.; Shin, C. H.; Chang, H.; Seung, D.; Yie, J. E.; Kim, J. M., Rational design of ordered mesoporous carbon with controlled bimodal porosity via dual silica templating route. *Chemical Communications* **2005**, (48), 6035-6037.

72. Kwon, T. H.; Jung, S.; Kim, H. J.; Park, S.; Kim, S. J.; Huh, S., Preparation of Mesoporous Silica and Carbon Materials with Multilength-Scale Pores and Hydrogen Sorption Application. *European Journal of Inorganic Chemistry* **2009**, (19), 2811-2816.

73. Huang, Y.; Cai, H. Q.; Yu, T.; Zhang, F. Q.; Zhang, F.; Meng, Y.; Gu, D.; Wan, Y.; Sun, X. L.; Tu, B.; Zhao, D. Y., Formation of mesoporous carbon with a face-centered-cubic Fd(3)over-barm structure and bimodal architectural pores from the reverse amphiphilic triblock copolymer PPO-PEO-PPO. *Angewandte Chemie-International Edition* **2007,** 46, (7), 1089-1093.

74. Wu, D. C.; Liang, Y. R.; Yang, X. Q.; Li, Z. H.; Zou, C.; Zeng, X. H.; Lv, G. F.; Fu, R. W., Direct fabrication of bimodal mesoporous carbon by nanocasting. *Microporous and Mesoporous Materials* **2008,** 116, (1-3), 91-94.

75. Liang, Y. R.; Liang, F. X.; Li, Z. H.; Wu, D. C.; Yan, F. Y.; Li, S. Y.; Fu, R. W., The role of mass transport pathway in wormholelike mesoporous carbon for supercapacitors. *Phys Chem Chem Phys* **2010,** 12, (36), 10842-10845.

76. Fuertes, A. B.; Nevskaia, D. M., Control of mesoporous structure of carbons synthesised using a mesostructured silica as template. *Microporous and Mesoporous Materials* **2003,** 62, (3), 177-190.

77. Lu, A. H.; Schmidt, W.; Spliethoff, B.; Schuth, F., Synthesis of ordered mesoporous carbon with bimodal pore system and high pore volume. *Adv. Mater.* **2003,** 15, (19), 1602-+.

78. Fuertes, A. B., Low-cost synthetic route to mesoporous carbons with narrow pore size distributions and tunable porosity through silica xerogel templates. *Chemistry of Materials* **2004,** 16, (3), 449-455.

79. Lu, A. H.; Li, W. C.; Schmidt, W.; Schuth, F., Template synthesis of large pore ordered mesoporous carbon. *Microporous and Mesoporous Materials* **2005,** 80, (1-3), 117-128.

80. Lai, Z. P.; Bonilla, G.; Diaz, I.; Nery, J. G.; Sujaoti, K.; Amat, M. A.; Kokkoli, E.; Terasaki, O.; Thompson, R. W.; Tsapatsis, M.; Vlachos, D. G., Microstructural optimization of a zeolite membrane for organic vapor separation. *Science* **2003,** 300, (5618), 456-460.

81. Snyder, M. A.; Tsapatsis, M., Hierarchical nanomanufacturing: From shaped zeolite nanoparticles to high-performance separation membranes. *Angewandte Chemie-International Edition* **2007,** 46, (40), 7560-7573.

82. Himeno, S.; Tomita, T.; Suzuki, K.; Nakayama, K.; Yajima, K.; Yoshida, S., Synthesis and permeation properties of a DDR-type zeolite membrane for separation of CO2/CH4 gaseous mixtures. *Ind. Eng. Chem. Res.* **2007,** 46, (21), 6989-6997.

83. Xomeritakis, G.; Tsapatsis, M., Permeation of aromatic isomer vapors through oriented MFI-type membranes made by secondary growth. *Chemistry of Materials* **1999,** 11, (4), 875-+.

84. Bowen, T. C.; Noble, R. D.; Falconer, J. L., Fundamentals and applications of pervaporation through zeolite membranes. *J. Membr. Sci.* **2004,** 245, (1-2), 1-33.

85. Coronas, J.; Santamaria, J., Separations using zeolite membranes. *Sep. Purif. Methods* **1999,** 28, (2), 127-177.

86. Hedlund, J.; Sterte, J.; Anthonis, M.; Bons, A. J.; Carstensen, B.; Corcoran, N.; Cox, D.; Deckman, H.; De Gijnst, W.; de Moor, P. P.; Lai, F.; McHenry, J.; Mortier, W.; Reinoso, J., High-flux MFI membranes. *Microporous and Mesoporous Materials* **2002,** 52, (3), 179-189.

87. Hedlund, J.; Jareman, F.; Bons, A. J.; Anthonis, M., A masking technique for high quality MFI membranes. *J. Membr. Sci.* **2003,** 222, (1-2), 163-179.

88. Gardner, T. Q.; Martinek, J. G.; Falconer, J. L.; Noble, R. D., Enhanced flux through double-sided zeolite membranes. *J. Membr. Sci.* **2007,** 304, (1-2), 112-117.

89. Sato, K.; Nakane, T., A high reproducible fabrication method for industrial production of high flux NaA zeolite membrane. *J. Membr. Sci.* **2007,** 301, (1-2), 151-161.

90. Kusakabe, K.; Murata, A.; Kuroda, T.; Morooka, S., Preparation of MFI-type zeolite membranes and their use in separating n-butane and i-butane. *J. Chem. Eng. Jpn.* **1997,** 30, (1), 72-78.

91. Lai, Z. P.; Tsapatsis, M.; Nicolich, J. R., Siliceous ZSM-5 membranes by secondary growth of b-oriented seed layers. *Advanced Functional Materials* **2004,** 14, (7), 716-729.

92. Ha, K.; Lee, Y. J.; Lee, H. J.; Yoon, K. B., Facile assembly of zeolite monolayers on glass, silica, alumina, and other zeolites using 3-halopropylsilyl reagents as covalent linkers. *Adv. Mater.* **2000,** 12, (15), 1114-+.

93. Xomeritakis, G.; Gouzinis, A.; Nair, S.; Okubo, T.; He, M. Y.; Overney, R. M.; Tsapatsis, M., Growth, microstructure, and permeation properties of supported zeolite (MFI) films and membranes prepared by secondary growth. *Chemical Engineering Science* **1999,** 54, (15-16), 3521-3531.

94. Lovallo, M. C.; Gouzinis, A.; Tsapatsis, M., Synthesis and characterization of oriented MFI membranes prepared by secondary growth. *Aiche Journal* **1998,** 44, (8), 1903-1913.

95. Lu, Y. F.; Ganguli, R.; Drewien, C. A.; Anderson, M. T.; Brinker, C. J.; Gong, W. L.; Guo, Y. X.; Soyez, H.; Dunn, B.; Huang, M. H.; Zink, J. I., Continuous formation of supported cubic and hexagonal mesoporous films by sol gel dip-coating. *Nature* **1997,** 389, (6649), 364-368.

96. Choi, J.; Ghosh, S.; King, L.; Tsapatsis, M., MFI zeolite membranes from a- and randomly oriented monolayers. *Adsorption-Journal of the International Adsorption Society* **2006,** 12, (5-6), 339-360.

97. Lee, I.; Buday, J. L.; Jeong, H. K., mu-Tiles and mortar approach: A simple technique for the facile fabrication of continuous b-oriented MFI silicalite-1 thin films. *Microporous and Mesoporous Materials* **2009,** 122, (1-3), 288-293.

98. Liu, Y.; Li, Y. S.; Yang, W., Fabrication of highly b-oriented MFI monolayers on various substrates. *Chemical Communications* **2009**, (12), 1520-1522.

99. Liu, Y.; Li, Y. S.; Yang, W. S., Fabrication of Highly b-Oriented MFI Film with Molecular Sieving Properties by Controlled In-Plane Secondary Growth. *Journal of the American Chemical Society* **2010,** 132, (6), 1768-+.

100. Lee, I.; Jeong, H. K., Synthesis and gas permeation properties of highly b-oriented MFI silicalite-1 thin membranes with controlled microstructure. *Microporous and Mesoporous Materials* **2011,** 141, (1-3), 175-183.

101. Jacobsen, C. J. H.; Madsen, C.; Janssens, T. V. W.; Jakobsen, H. J.; Skibsted, J., Zeolites by confined space synthesis - characterization of the acid sites in nanosized ZSM-5 by ammonia desorption and Al-27/Si-29-MAS NMR spectroscopy. *Microporous and Mesoporous Materials* **2000,** 39, (1-2), 393-401.

102. Tao, Y. S.; Kanoh, H.; Kaneko, K., ZSM-5 monolith of uniform mesoporous channels. *Journal of the American Chemical Society* **2003,** 125, (20), 6044-6045.

103. Madsen, C.; Jacobsen, C. J. H., Nanosized zeolite crystals - convenient control of crystal size distribution by confined space synthesis. *Chemical Communications* **1999**, (8), 673-674.

104. Schmidt, I.; Madsen, C.; Jacobsen, C. J. H., Confined space synthesis. A novel route to nanosized zeolites. *Inorganic Chemistry* **2000,** 39, (11), 2279-2283.

105. Yoo, W. C.; Stoeger, J. A.; Lee, P. S.; Tsapatsis, M.; Stein, A., High-Performance Randomly Oriented Zeolite Membranes Using Brittle Seeds and Rapid Thermal Processing. *Angewandte Chemie-International Edition* **2010,** 49, (46), 8699-8703.

106. Lee, P. S.; Zhang, X. Y.; Stoeger, J. A.; Malek, A.; Fan, W.; Kumar, S.; Yoo, W. C.; Al Hashimi, S.; Penn, R. L.; Stein, A.; Tsapatsis, M., Sub-40 nm Zeolite Suspensions via Disassembly of Three-Dimensionally Ordered Mesoporous-Imprinted Silicalite-1. *Journal of the American Chemical Society* **2011,** 133, (3), 493-502.

107. Varoon, K.; Zhang, X. Y.; Elyassi, B.; Brewer, D. D.; Gettel, M.; Kumar, S.; Lee, J. A.; Maheshwari, S.; Mittal, A.; Sung, C. Y.; Cococcioni, M.; Francis, L. F.; McCormick, A. V.; Mkhoyan, K. A.; Tsapatsis, M., Dispersible Exfoliated Zeolite Nanosheets and Their Application as a Selective Membrane. *Science* **2011,** 333, (6052), 72-75.

Chapter 2:

Template-free Ordered Mesoporous Silicas by Binary Silica Nanoparticle Assembly

This chapter closely follows the publication:

Kung, S.-C., Chang, C.-C., Fan, W., Snyder, M.A.*, "Template-free ordered mesoporous silicas by binary nanoparticle assembly," *Langmuir* 2014, **30**, 11802-11811.

2.1 Introduction

Since the discovery and development of the M41S family of ordered mesoporous silicas (e.g., MCM-41, MCM-48, MCM-50) by Mobil researchers[1] in 1992, more than two decades after comparable mesoporous materials were first patented by Chiola and co-workers as novel ultra-low-density structures[2], significant research efforts have been spent on the development of ordered mesoporous silicas (OMSs) of various pore topologies and pore sizes. The result has been an expansion of OMSs to include the SBA[3-5], MCM[1], FDU[6], KIT[7, 8], MSU-H[9], HMS[10], and other[11] families of mesoporous materials. Linking most of these material classes is their common reliance on silica/alumina precursor hydrolysis and condensation in the presence of self-assembling lyotropic phases of cationic, anionic, or nonionic surfactants. This results in size-tunable, ordered mesopore topologies upon template sacrifice (e.g., calcination, solvent extraction). Despite pore size tunability

spanning ca. 1.5 to 20 nm, pore walls of conventional OMSs tend to be thin and suffer from hydrothermal instability. Together with the wormy pores and intrinsic heterogeneity in surface silanol distribution, both of which challenge efforts to uniformly disperse molecular or particulate moieties by conventional incipient wetness techniques, these materials have proven more challenging than originally perceived for application, for example, as novel catalytic supports.

As an alternative to conventional surfactant-templated OMSs, the ability to realize complex structures by assembly of pre-formed constituent building blocks holds promise for template-free, bottom-up materials synthesis. To this end, colloidal assembly offers a promising approach wherein interstices between crystallized spherical particles effectively provide a 3D-interconnected pore space, opposite that of FDU-16[6, 12, 13] and SBA-16[4, 14] OMSs, which exhibit 3D cubic structures comprised of spherical pores. Yet, realizing ordered mesoporous rather than macroporous silicas requires the assembly of silica nanoparticles in lieu of micron or even sub-micron particles, the latter of which have been more commonly studied due to their novel optical properties[15, 16]. The recent demonstration by us[17-19] and others[20, 21] of how colloidal crystal silica component size can be scaled down to particles on the order of 10 nm (termed Lys-Sil nanoparticles) via aqueous-phase amino acid-assisted synthesis, has enabled realization of mesoporous and even microporous silicas via unary nanoparticle crystallization. Specifically, unary Lys-Sil nanoparticle crystalline powders can be achieved by simple evaporative drying of nanoparticle sols. While such unary assemblies result in three-dimensionally ordered porous materials with thicker walls than conventional OMSs, albeit of lower specific surface area, the extent to which the pore topology can be tuned and tailored depends on

the ability to expand the achievable structural diversity. This represents a challenge for unary nanoparticle assembly, for which free energy effects limit assembly to only close packed structures (e.g., hcp, fcc).

In 1980, Murray and Sanders[22, 23] identified the unique naturally occurring structure of a Brazilian opal with coexisting binary colloidal crystalline phases (AB_2 an AB_{13}) comprised of ordered assemblies of large (A) and small (B) sub-micrometer silica particles. That work demonstrated that without relying on complex and possibly costly template- or ligand-mediated assembly, structural diversity may be achieved by introduction of one or more additional, distinctly sized building blocks capable of modulating multi-modal assembly while also contributing to the resulting solid structure. The specific binary colloidal crystalline phases in that natural sample were subsequently predicted by geometric space-filling arguments[23] as well as statistical thermodynamic models[24-27] of entropy-driven hard-sphere assembly. These early findings and the theoretical predictions of hard sphere phase behavior, depicted in **Figure 2-1**a, have motivated diverse laboratory studies to realize bimodal particle assemblies.

Up to now, these efforts have primarily focused on two particle scales: 1) assembly of ligand-mediated nano-scale metal and/or metal oxide particles (hydrodynamic diameter less than 10 nm) from organic solvents into a structurally diverse range of so-called binary nanoparticle superlattices (BNSLs)[28-32] and 2) assembly of sterically stabilized (i.e., by polymeric ligands) micron and sub-micron polystyrene (PS),[33, 34] polymethylmethacrylate (PMMA),[35, 36] and silica particles,[37, 38] focused primarily on binary particle mixtures spanning moderate to large size ratios (i.e, the largest size ratios coming from mixtures of sub-micron and nanoscale particles). Only recently, has proof-of-concept binary assembly

been realized with silica nanoparticles,[39] yielding two examples of AB_2 (26/51 nm) and AB_{13} (19/35 nm) phases akin to those observed previously in natural opals, and consistent with predicted hard-sphere phase behavior (X symbols, **Figure 2-1**a), albeit for a limited slice of that phase space.

The tentative agreement of the silica nanoparticle assembly with hard-sphere phase space is especially striking given i) the lack of specific steric stabilization of the Lys-Sil nanoparticles, ii) the absence of specific charge stabilization or refractive index-matching to minimize van der Waals attractions beyond intrinsic solution conditions, and iii) the recognized differences in interaction potentials for nanometer scale relative to sub-micron particles[40] for which hard-sphere predictions generally apply. In order to establish a fundamental platform from which to achieve rational, bottom-up assembly of a range of template-free OMSs, more comprehensive analysis of the silica nanoparticle phase behavior, insight into parametric sensitivity and robustness, and development of a mechanistic understanding of assembly and dominant kinetic factors is required.

Here, we employ so-called Lys-Sil[17-19] silica nanoparticles, synthesized through an amino acid (e.g., Lysine) mediated route with near nanometer resolution over particle size, as a model for developing insight into the corresponding binary phase behavior. We have previously employed complementary SAXS and cryo-transmission electron microscopy (cryo-TEM) analysis of dilute sols of Lys-Sil nanoparticles to confirm the spherical geometry of these nanoparticles.[17, 18] Through a systematic study of assembly in which particle size and stoichiometry are controlled, we establish synthesis-structure relations that may be exploited in the future for the rational design of novel OMSs with function tailored by bottom-up in situ (e.g., co-assembly) rather than ex situ (e.g., incipient wetness)

strategies. We first fully map the phase space describing binary silica nanoparticle assembly relative to hard-sphere predictions, and then systematically study the sensitivity of the resulting structures to tunable factors such as solution stoichiometry, solution composition (e.g., amino acids used in the nanoparticle synthesis), and particle size. Study of the role of conditions employed for assembly (e.g., temperature, pressure) help to begin elucidating kinetic sensitivity of the system, specifically to apparent time scales for bulk convective assembly and local reorganization/crystallization. Ultimately, we demonstrate robust assembly of a range of 3D-ordered mesopore topologies (AB, AB_2, AB_{13}, and interstitial solids) of independently tunable pore size.

2.2 Experimental

2.2.1 Synthesis of size-tunable silica nanoparticles

Silica nanoparticles (Lys-Sil nanoparticles) of different particle sizes were synthesized using lysine (Sigma Aldrich, 98%)-mediated hydrolysis of tetraethylorthosilicate (TEOS, 98%, Sigma-Aldrich) in aqueous solutions as reported previously.[17-19] Specifically, Lys-Sil nanoparticles of nominal diameters of ca. 20 nm or less were synthesized by addition of prescribed amounts of TEOS to an aqueous solution of L-lysine that was heated to 90^{o}C. Hydrolysis was carried out under vigorous stirring for 24 hrs, liberating ethanol and yielding solutions of final molar composition (x SiO_2/y lysine/9500 water/4x ethanol) specified in **Table 2-1** according to particle size. Larger Lys-Sil particles were synthesized by employing the ca. 20 nm particles as seeds as described in Ref. [19]. Specifically, sequential aliquots of TEOS were hydrolyzed directly in the ca. 20 nm seed sol at 90^{o}C under vigorous stirring for 24 hrs until the total prescribed

amount of TEOS was reached. The final molar compositions of sols of Lys-Sil particles of ca. 10 nm to 50 nm are tabulated in **Table 2-1**.

Table 2-1. Final molar compositions, ***x*** SiO_2/***y*** lysine/9500 water/4***x*** ethanol, of Lys-Sil nanoparticles yielding particles of specified diameter by direct or seeded growth (TEOS split into specified number of equal-volume aliquots).

Nominal particle size [nm]	**Measured particle size [nm][a]**	**Seed size and molar composition**			**Final molar composition**		
		Nominal seed size [nm]	***x*** **(SiO_2)**	***y*** **(L-lysine)**	***x*** **(SiO_2)**	***y*** **(L-lysine)**	**TEOS aliquots**
10[b]	10.8 ± 0.4	--	--	--	61.5	5.8	1
15	14.7 ± 1.0	--	--	--	26.9	1.23	1
17	17.1 ± 0.4	--	--	--	31.5	1.23	1
19	19.4 ± 0.7	--	--	--	61.5	1.23	1
23	22.5 ± 1.1	19	61.5	1.23	98.9	1.23	1
24	24.3 ± 1.1	19	61.5	1.23	106.3	1.23	1
32	32.2 ± 1.1	19	61.5	1.23	252	1.23	3
41	41.2 ± 1.4	19	61.5	1.23	492	1.23	3
43	43.1 ± 1.7	19	61.5	1.23	611.2	1.23	3
50	49.9 ± 1.1	19	61.5	1.23	950	1.23	4

[a] Average and standard deviation based upon measurement of more than 60-100 particles in TEM images.
[b] The synthesis temperature of 10 nm silica nanoparticles is 60°C, while all other particles were synthesized at 90°C.

2.2.2 Mixing and drying of binary silica nanoparticle mixtures

The nominal size, *D*, of batches of silica nanoparticles was measured directly from TEM images of the dried sols, with an average and standard deviation calculated from measurements of 60-100 particles. The number density (ϕ_i) of particles in each Lys-Sil sol was measured by drying and weighing, assuming a silica density of 1.8 cm^3/g.[41] Targeted binary mixtures were prepared by mixing appropriate volumes (V_A, V_B) of each of two sols containing large (D_A) and small particles (D_B), respectively, in order to achieve a desired small-to-large stoichiometry, $N = (V_B\phi_B D_A^3)/(V_A\phi_A D_B^3)$, and a specific particle size ratio, $\gamma = D_B / D_A$, respectively. Once formed, the mixtures were sonicated for 15 minutes followed by evaporation at prescribed temperatures and pressures. Nominally, evaporation was carried out at ambient temperature and pressure, but temperatures as high as 40 °C and vacuum conditions (i.e., 0.03 atm) were employed to elucidate competing kinetics, and were imposed using a vacuum oven in which the temperature was stabilized at the prescribed set point for ca. 2 hrs prior to addition of the sample.

2.2.3 Characterization

Scanning electron microscope (SEM) and TEM images were collected on a Hitachi S-4300 and a JEOL 2000FX, respectively, to study the morphology and microstructure of the samples. In the case of SEM, dried silica powders were lightly crushed using a mortar and pestle, and dispersed on an aluminum SEM stub covered with adhesive carbon tape. Samples were sputter coated with iridium to improve conductivity and thereby reduce charging during imaging. Carbon-coated copper grids (Ted Pella) were employed for TEM. 2D small angle x-ray scattering data (2D-SAXS, Rigaku S-Max3000) were collected for

insight into sample mesostructure. Simulated X-ray reflections were calculated with PowderCell software[42] to aid in indexing 2D-SAXS patterns based upon corresponding isostructures for the binary assemblies (see SI for determination of lattice constants). Nitrogen physisorption analysis was carried out on a Micromeritics ASAP-2020 analyzer at 77 K to assess textural properties of the samples. All samples were degassed at 350 °C for at least 12 hours prior to analysis. The Brunauer-Emmett-Teller (BET) method was applied to estimate the total specific surface area. The total pore volume (V_t) was estimated from the adsorbed amount at a relative pressure P/P_0~0.995. Mesopore analysis was based on the t-plot method. Barrett-Joyner-Halenda (BJH) analysis of the desorption branch of the isotherm was applied for estimation of the pore size distribution within the silica assemblies, as done previously for unary Lys-Sil nanoparticle crystals,[43] recognizing that the cylindrical pore basis for BJH analysis makes the pore sizes only approximate.

2.3 Results and Discussion

2.3.1 Binary hard-sphere phase behavior of Lys-Sil nanoparticle assembly

In order to better understand the factors controlling the phase behavior of binary silica nanoparticle superlattices and to gain insight into the robustness of the corresponding assembly for realizing ordered mesoporous silicas with tunable pore topology and size, we have carried out a comprehensive experimental investigation leveraging size-tunable monodisperse silica nanoparticles (Lys-Sil nanoparticles) ranging from ca. 10 to 50 nm in size. Sols of monodisperse silica nanoparticles were synthesized by the previously established amino acid assisted hydrolysis of TEOS through direct and seeded techniques[17-19], enabling particle size control with nanometer resolution. Free lysine within the as-made

Lys-Sil nanoparticle sols effectively buffers the solution to pH~9-10, far from the isoelectric point for silica at pH~2.[41] As shown in **Figure 2-1**b (solid circles), in these as-made Lys-Sil solutions, the zeta potential of the smallest (ca. 15 nm) silica particles is strongly negative (ca. ζ=-100 mV), while the magnitude of the zeta potential systematically decreases with increasing particle size. It is conceivable that the zwitterionic and cationic Lysine may associate in two ways with the silica particles, either through surface adsorption[44-46] or by physical encapsulation within the volume of the silica particle during the seeded particle growth. We discuss later (Chapter 3) how intrinsic differences in the zeta potential of smaller and larger particles (**Figure 2-1**b), the latter achieved by sequential seeded growth without the replenishment of lysine, may result from differences in the amount of lysine adsorbed onto and/or physically encapsulated within the particle.

The larger implication of the concomitant size-dependent particle stability is the unclear relative roles of electrostatic, dispersion, and hard sphere interactions in modulating co-assembly of Lys-Sil nanoparticles without specific steric stabilization, especially where assemblies of particles of dramatically different size are considered. **Figure 2-1**a shows predictions of hard-sphere phase behavior, dominated by entropic effects, for stoichiometric AB, AB_2, and AB_{13} binary assemblies as a function of the ratio, γ, of small (B) to large (A) particle sizes based upon geometric space-filling predictions[23] and more rigorous statistical mechanics approaches including Monte Carlo simulations[24-26] and cell calculations.[27] Here, guided by these predictions, we first selected particle size ratios (open squares (i)-(iii), **Figure 2-1**a) falling well within each of the three predicted hard sphere phase boundaries (AB_2, AB_{13}, and AB). We held the size of the largest particle nearly constant (ca. 42 nm), and systematically adjusted the size of the smallest particle

while tuning the small-to-large particle stoichiometry of the binary solution, N, to match that of the predicted solid (i.e., AB_N): AB_2 (γ =19 nm/41 nm=0.47, N=2), AB_{13} (γ =24 nm/41 nm=0.59, N=13), AB (γ =15 nm/43 nm=0.34, N=1).

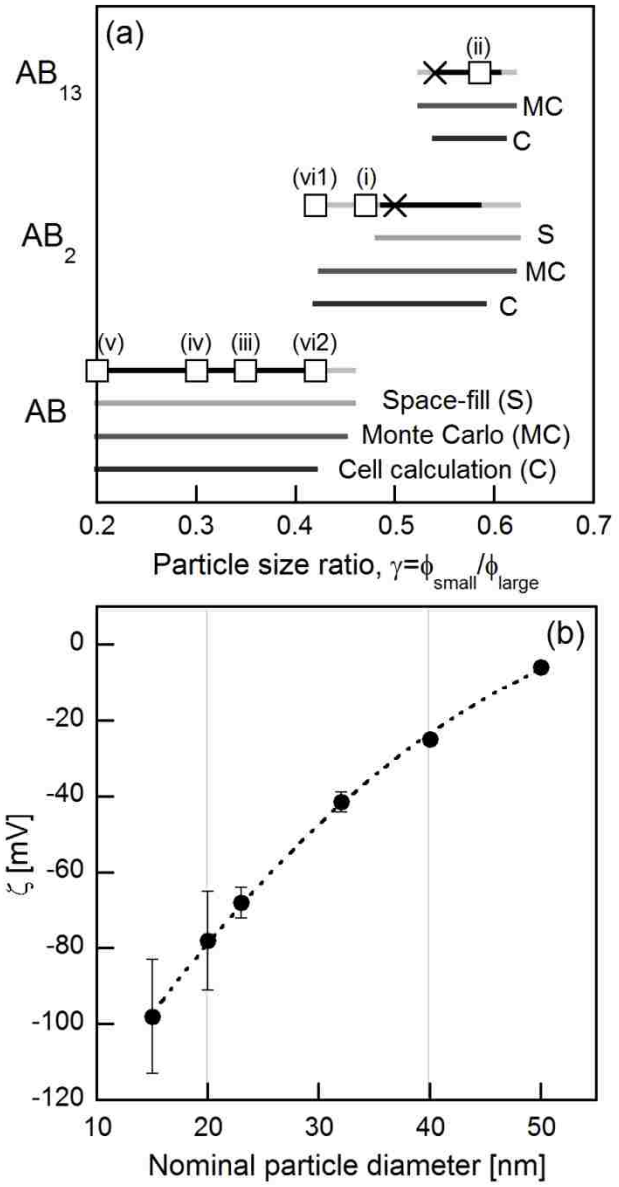

Figure 2-1. Depiction of (a) stability windows for AB, AB_2, and AB_{13} binary hard-sphere structures for given particle size ratios, γ, as predicted by geometric space-filling arguments (S)[23], Monte Carlo simulations (MC)[24-26], and cell calculations (C)[27]. The top-most trace for each of the three phases represents a composite of all predictions, showing the minimum (black region) and maximum (gray region) limits according to predictions. Open square symbols labeled (i)-(vi) denote specific particle size ratios explored in this work, whereas the X symbols denote work from Ref. [39]. Panel (b) shows zeta potential measurements of as-made (dashed line for visual aide) lysine-silica nanoparticle sols of various sizes.

TEM surveys (not shown) of the resulting binary nanoparticle assemblies prepared at ambient temperature and pressure reveal remarkable yields of the binary nanoparticle crystalline structures, in most cases estimated to exceed 70%. These ordered assemblies coexist with minor fractions of disordered binary nanoparticle assemblies and/or segregated ordered and disordered unary nanoparticle assemblies. Representative TEM images taken along the [001] zone axes of the resulting ordered binary colloidal crystals are shown in **Figure 2-2**a-c. The images reveal distinct binary assemblies associated with the three particle size ratios. For the larger particle size ratios (i.e., γ=0.47, 0.59), hard-sphere phase behavior predicts respective AB_2 and AB_{13} crystalline stoichiometries. Geometric models of AlB_2 and $NaZn_{13}$ isostructures, which are reported to be the most stable among the respective AB_2 and AB_{13} phases,[28, 36] are shown for visual comparison as overlays within the corresponding TEM images. The good registry of the models with the binary periodicity of each sample provides tacit indication, complementary to that reported previously by Kuroda and co-workers[39] (X symbols, **Figure 2-1**a), of the possible applicability of hard sphere predictions for accurately describing at least some of the binary phase behavior of solid solutions derived from multi-modal mixtures of Lys-Sil nanoparticle sols.

We have further exploited particle size tunability of the Lys-Sil nanoparticle system to explore values of γ below the theoretically predicted lower limit for the AB_2 phase (i.e., γ<0.42), where hard sphere phase behavior predicts AB-type structures (**Figure 2-1**a). In the case of binary Lys-Sil nanoparticle assembly at γ=0.34 and N=1 (point (iii), **Figure 2-1** a), we have found stable binary structures with symmetries distinct from the AB_2 and AB_{13} phases as shown by the representative TEM image along the [001] zone axis of the resulting

binary powder in **Figure 2-2**c. While NaCl and NiAs are predicted to be the most stable isostructures of the AB phase on the basis of maximum packing density,[47] they have distinctly different particle arrangements. The good agreement between the TEM image and an overlay model of the NaCl isostructures, comprised of interpenetrating face-centered cubic (fcc) lattices of large and small particles, provides first confirmation of the stability and accessibility of the AB binary phase in addition to the AB_2 and AB_{13} phases for the Lys-Sil system.

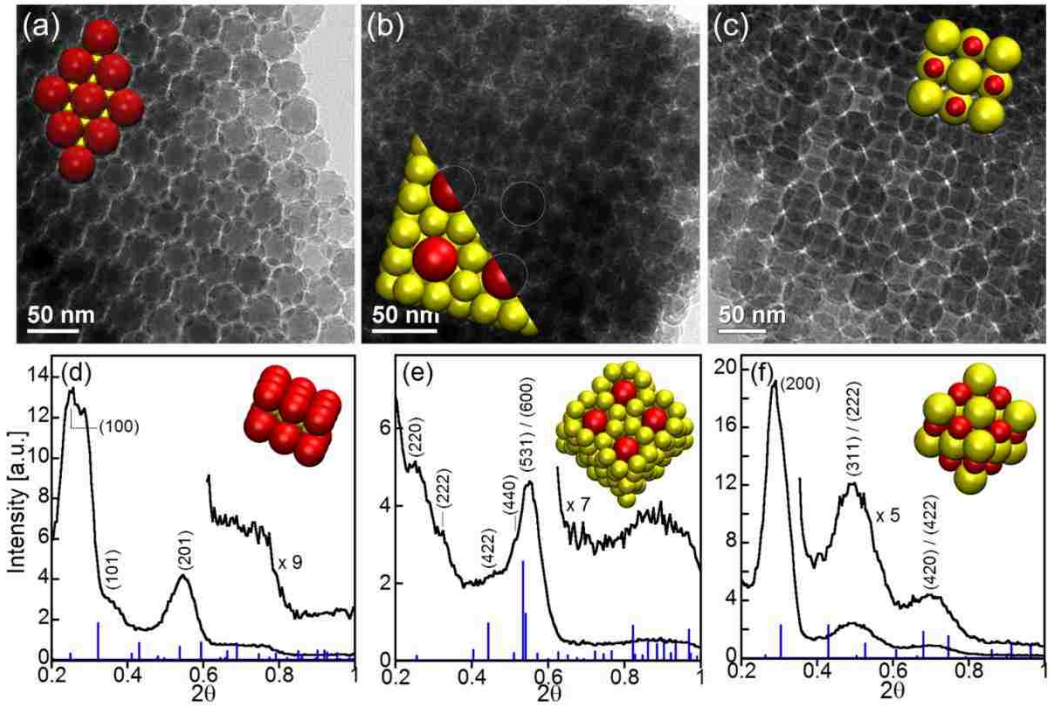

Figure 2-2. TEM images along the [001] zone axis and corresponding 2D-SAXS data collected from binary silica nanoparticle assemblies prepared from particle size ratios, γ, depicted as (i)-(iii) in **Figure 2-1**, and solution stoichiometries, N, of (a) γ=0.47 (19nm/41nm), N=2, (b) γ=0.59 (24nm/41nm), N=13, and (c) γ=0.34 (15nm/43nm), N=1. The TEM images and SAXS patterns (see indexing) are consistent with (a,d) AlB2, (b,e) NaZn13, and (c,f) NaCl isostructures, with corresponding geometric models (red particles: large, yellow particles: small in (a,d) and (b,e); yellow particles: large, red particles: small in (c,f)) and simulated diffraction patterns shown for reference.

2D-SAXS of the bulk binary powders (**Figure 2-2**d-f) provides additional assessment of the bulk 3D structure in complement to the local structural insight achievable by TEM. 2D-SAXS reveals 3D crystallinity in all cases studied. Despite confounding effects of the minor fraction (<30%) of coexisting disordered binary phases and ordered and disordered unary phases, the measured SAXS data bear reflections that are in reasonable agreement with ones simulated for NaCl (AB), AlB_2 (AB_2), and $NaZn_{13}$ (AB_{13}) isostructures, supporting the good agreement observed between geometric models of those isostructures and the TEM images in **Figure 2-2**a-c.

While smaller domains (i.e., 500 nm) of binary nanoparticle superlattices are observed in the case of the AB_{13} assemblies by TEM, attributed to the complexity of this particular phase from an imaging standpoint, large single crystalline regions extending over more than 1 μm in the case of AB and AB_2 structures are observed (see **Figure 2-3** and **Figure 2-4**, respectively). Ultimately, the large single-crystalline binary NaCl- and AlB_2-type structures observed for the Lys-Sil systems are consistent with the intrinsic stability of those structures, owing to corresponding packing densities for γ=0.34 and γ=0.47 in excess of that for both face-centered cubic (fcc) and hexagonally close-packed (hcp) crystal structures.

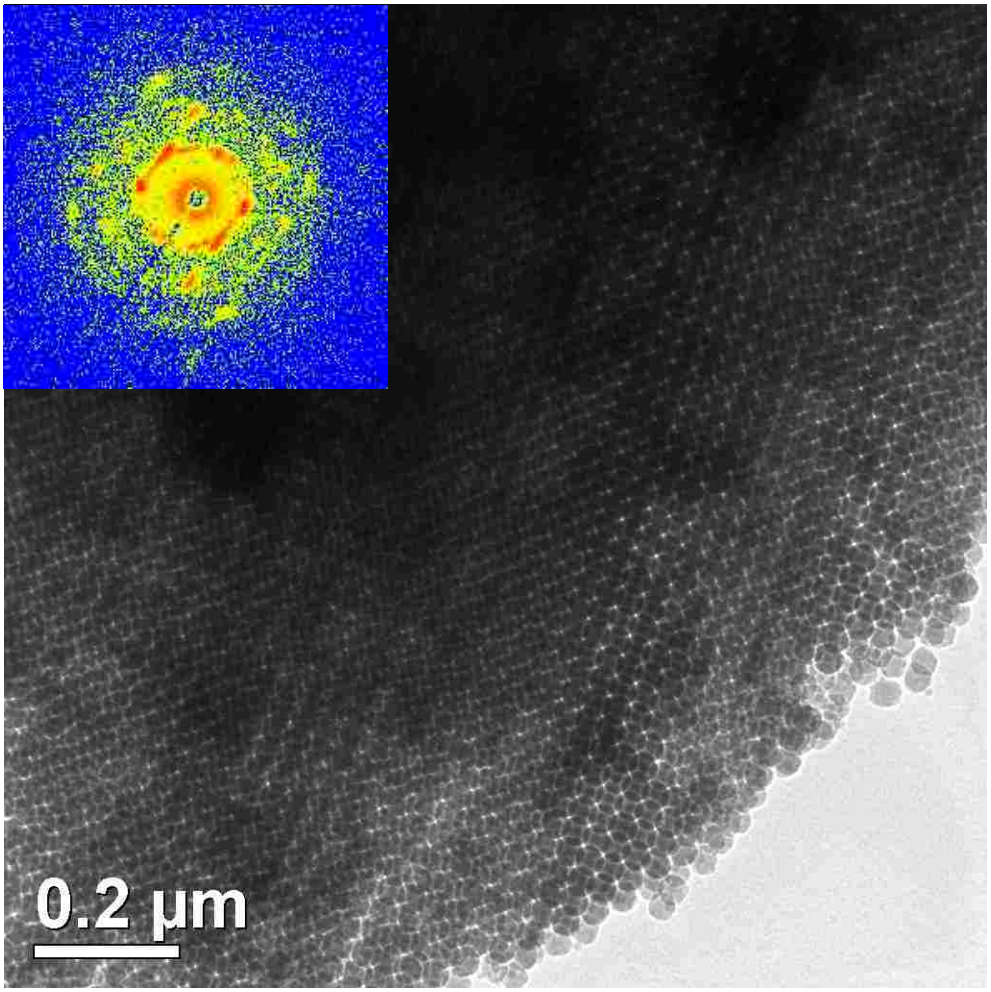

Figure 2-3. Single crystal of binary silica nanoparticle superlattice with 15/43 nm NaCl-type structure (γ=0.34, and N=1). Inset shows 2D-SAXS diffraction pattern underscoring the extent of single crystallinity.

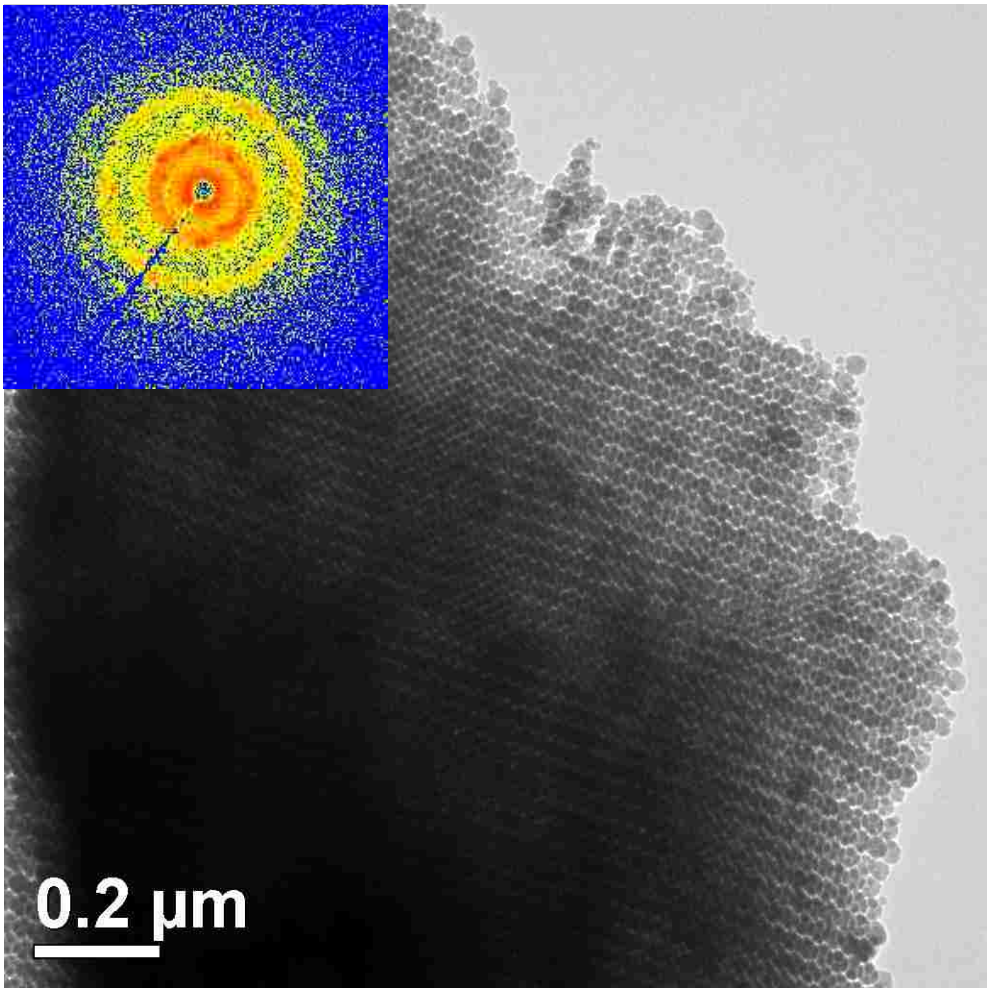

Figure 2-4. Single crystal of binary silica nanoparticle superlattice with 19/41nm AlB_2-type structure (γ=0.47, and N=2). The inset shows the 2D-SAXS diffraction pattern.

By further tuning the particle size ratio over the predicted breadth of the AB phase window, previously unexplored for the Lys-Sil system, we have observed persistent stability of a pseudo-AB phase at smaller γ. Namely, as shown by TEM images in **Figure 2-5**, NaCl-like structures result from γ=0.2 and γ=0.3 (N=1) binary assemblies (points (v) and (iv), **Figure 2-1**a), albeit of lower yields. Here, the largest particles are packed on an fcc lattice as expected for the NaCl-like system, with an interpenetrating fcc/ccp sub-lattice of "Cl"-associated interstices that are heterogeneously occupied by the smaller particles

such that vacancies as well as single- and even double-occupancy of these interstices is observed. Here, the fact that the smallest particles are smaller than the interstitial pores formed between the assembled larger particles, allows for their interstitial migration and, thereby, formation of a NaCl-like interstitial solid solution. What is perhaps most striking is that, in the case of the lower γ, fcc/ccp arrangement of the largest particles seems to persist despite apparent interstitial mobility of the smaller particles.

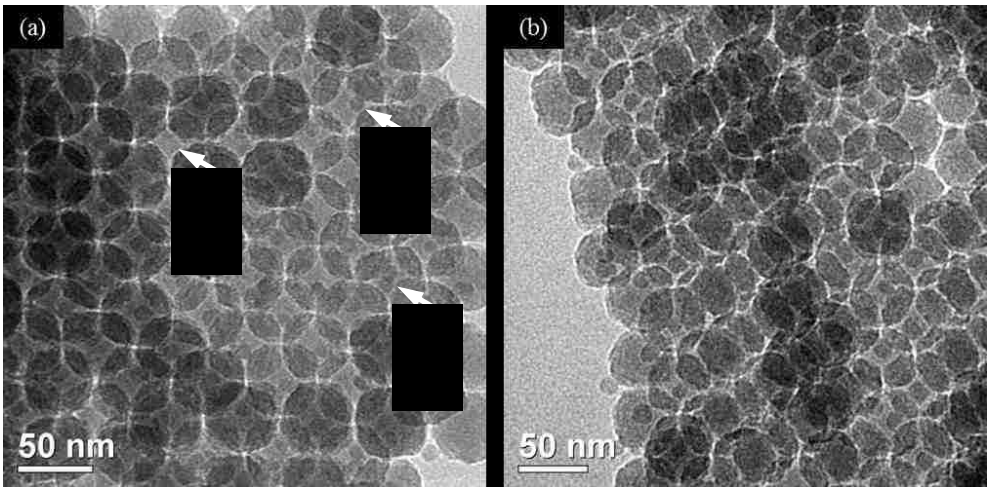

Figure 2-5. NaCl-like binary interstitial solid solutions with (a) γ=0.2 (10/50nm), and (b) γ=0.3 (15/50nm) templated by apparently mobile smaller particles leading to vacant (V arrow, panel a) up to two smaller particles (1, 2 arrow, panel a) occupying octahedral interstices of the cubically arranged larger particles.

Up to now, we have separately confirmed the accessibility of each of the three phases predicted by hard-sphere approximations, and have clarified the existence of an interstitial solid solution at small enough γ. In order to further assess the relevance of hard-sphere approximations for describing the Lys-Sil nanoparticle system, we have also probed the predicted boundary between the two stable phases, AB and AB_2. This phase boundary

marks one of the largest discrepancies among the three models for hard-sphere phase behavior. Namely, space-filling arguments suggest a finite break in the phase diagram, while Monte Carlo calculations predict a significant overlap between the AB and AB_2 phases and cell calculations predict their discrete coexistence (**Figure 2-1**a).

We have explored this phase boundary by increasing the particle size ratio to the predicted upper limit for the AB-type system while also raising N from unity to 2. Specifically, for binary Lys-Sil nanoparticle assemblies with γ=0.42 and N=2, we find coexisting AB (NaCl) and AB_2 (AlB_2) binary structures (respective points (vi2) and (vi1), **Figure 2-1**a). The coexistence of these two phases is revealed by the corresponding TEM images in **Figure 2-6**, both of which have been collected from the same sample. This finding provides experimental confirmation of the AB/AB_2 phase boundary predicted by Monte Carlo simulations and cell calculations that is not captured by simple space-filling arguments.

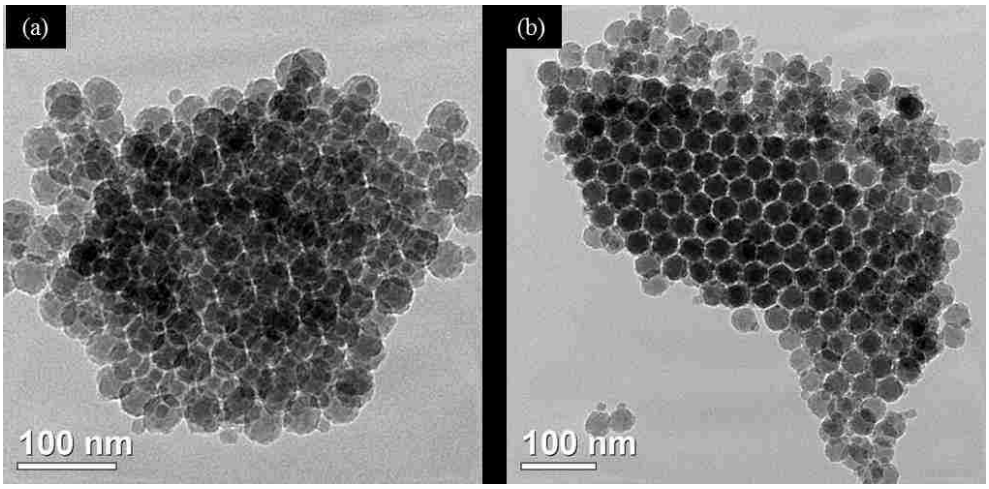

Figure 2-6. Coexisting (a) NaCl-like and (b) AlB2-like binary assemblies marking the AB/AB2 phase boundary for γ=0.42 (17/41nm).

2.3.2 Sensitivity of binary Lys-Sil assembly to incipient solution stoichiometry, N

An interesting implication of this coexistence of the AB phase with the AB_2 phase is that both phases were derived from a solution having an AB_2 (i.e, N=2) rather than an AB (i.e., N=1) solution stoichiometry. This provides first insight into the apparent insensitivity of the binary phase behavior to the incipient solution stoichiometry or specific number density, N, of small relative to large particles. **Figure 2-7** explores this further by studying the binary crystal structures assembled from solutions with tailored particle number ratios, N, for a fixed γ=0.47. Ultimately, this γ was previously identified (point (i), **Figure 2-1**; **Figure 2-2**ad) to result in AlB_2 isostructures when the stoichiometry of the solution (N=2) was matched with that of the solid phase (AB_2).

Figure 2-7 shows corresponding SAXS data collected on binary powders assembled from super-stoichiometric (N=5) to sub-stoichiometric solutions (N=1) compared to the nominal AB_2 stoichiometry (N=2). In addition to consistency of TEM images (**Figure 2-7** b-d) along various specified zone axes with the AlB_2 isostructure,

comparison of SAXS data among the three samples shows relative insensitivity of the mesostructure, symmetry, and order of the binary powders over the range of incipient solution stoichiometry explored. Here, of course, non-stoichiometric conditions must be accommodated during assembly. TEM survey scans show that the binary nanoparticle crystalline structures coexist with unary ordered and disordered assemblies, defective binary lattices (i.e., with small particle vacancies), and disordered non-stoichiometric binary assemblies for sub- (N=1) and super-stoichiometric (N=5) conditions (see **Figure 2-8** and **Figure 2-9**, respectively). Thus, effective self-selection of the final binary phase occurs, and appears to be fixed by the particle size ratio, γ. No measured sensitivity to incipient solution stoichiometry beyond the overall percent yield is observed.

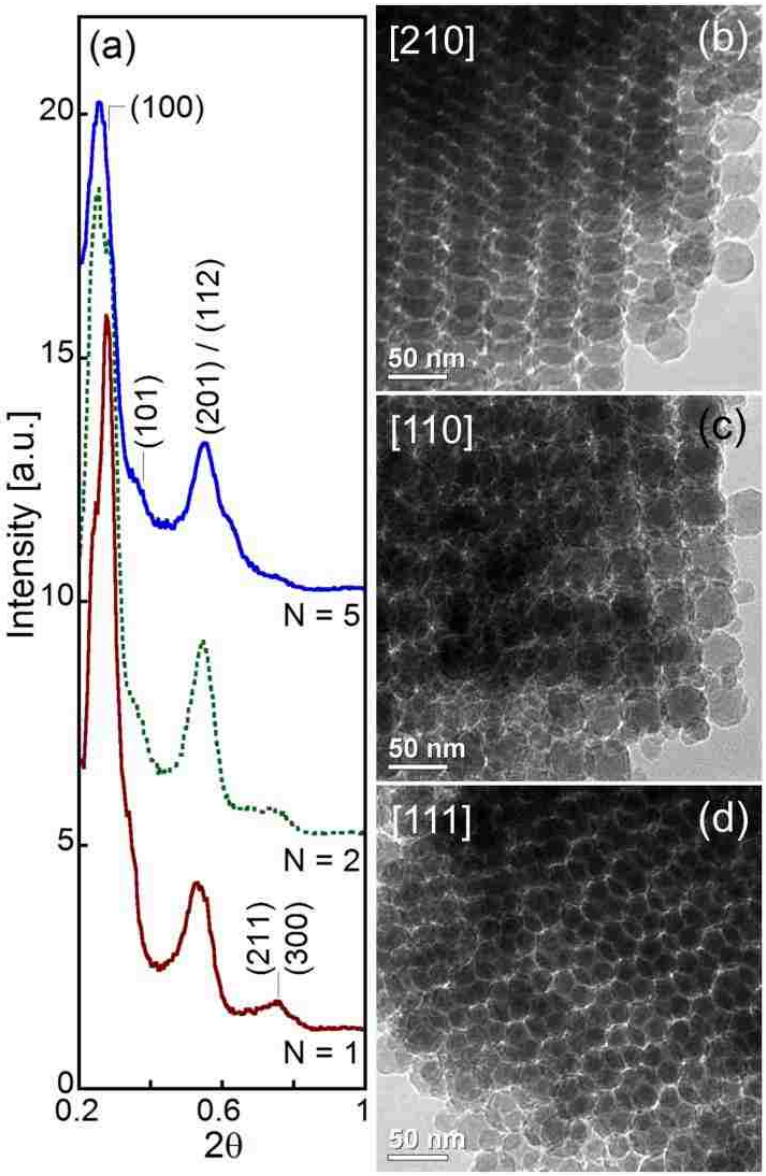

Figure 2-7. (a) 2D-SAXS data and (b-d) representative TEM images along specified zone axes showing the structural insensitivity of binary silica nanoparticle assembly to both super- (N=5) and sub-stoichiometric (N=1) solution conditions for a fixed size ratio of γ=0.47 (19nm/41nm) that has been shown to yield AB2 materials isostructural with AlB2 under stoichiometric (N=2) conditions.

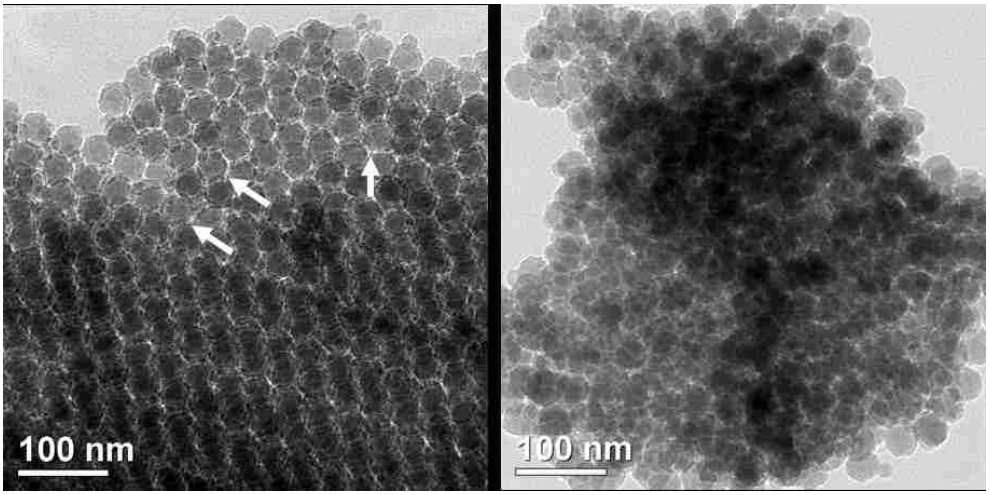

Figure 2-8. Defects of binary silica nanoparticle superlattices with 19/41nm AlB2-type structure (γ=0.47, N=1) indicated by white arrows: (a) vacancy of interstitial space between large particles; (b) disordered binary silica assembly.

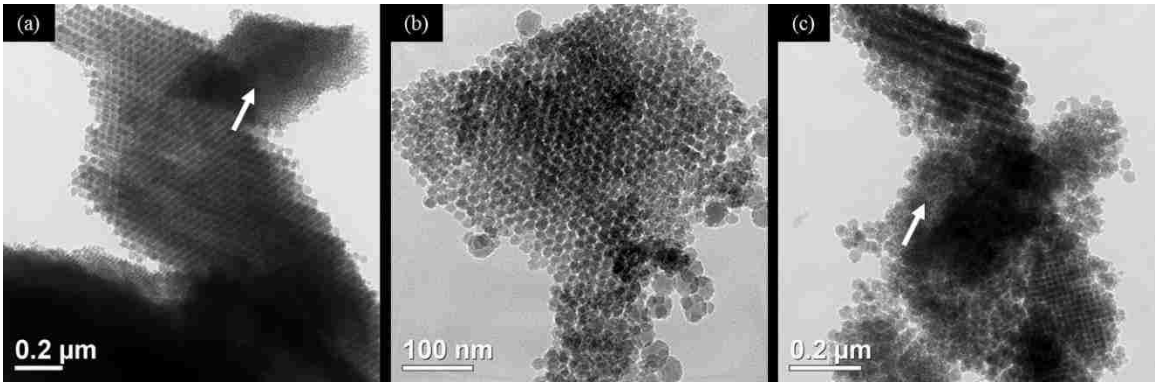

Figure 2-9. Defects of binary silica nanoparticle superlattices with 19/41nm AlB2-type structure (γ=0.47, N=5) indicated by white arrows. (a), (b) segregated domain of small particles, and (c) disordered binary silica assembly.

2.3.3 Template-free pore size tunability of OMSs derived from binary Lys-Sil assembly

Beyond this insensitivity of the binary nanoparticle phases to varying *N*, we have also studied the robustness of the assembly process to systematic changes in particle size. To this end, we have fixed the particle size ratio at approximately γ=0.46 and have

systematically perturbed the size of the large and small silica particles, both by ca. ±20% relative to the nominal particle sizes used previously for exploring the AB_2 phase (19/41 nm, point (i) in **Figure 2-1**). **Figure 2-10** shows TEM images along the [001] zone axis of the resulting binary crystals and corresponding 2D-SAXS analysis of the powders, the latter compared to the nominal case (dashed spectra, **Figure 2-10**a). The TEM images clearly show the persistent AB_2-type assemblies that display long-range 3D order and again appear isostructural with AlB_2 as confirmed by the corresponding SAXS data. Specifically, the systematic shift of the primary small-angle reflections to larger 2θ as particle size is decreased, is consistent with the concomitant decrease in lattice spacing within the binary assemblies, and underscores the robustness of the binary assembly of Lys-Sil nanoparticles. The persistence of the nominal AlB_2 isostructure for a given particle size ratio, the latter achieved by systematically tuning the size of both the large and small particles, further highlights how the corresponding phase behavior appears to be controlled exclusively by the ratio rather than specific sizes of the particles. Ultimately, the ability to control the size of the constituent particles and, thereby, the lattice spacing of the final assembly, while maintaining a specific phase, should lead to tunability of the pore size of the derived OMS.

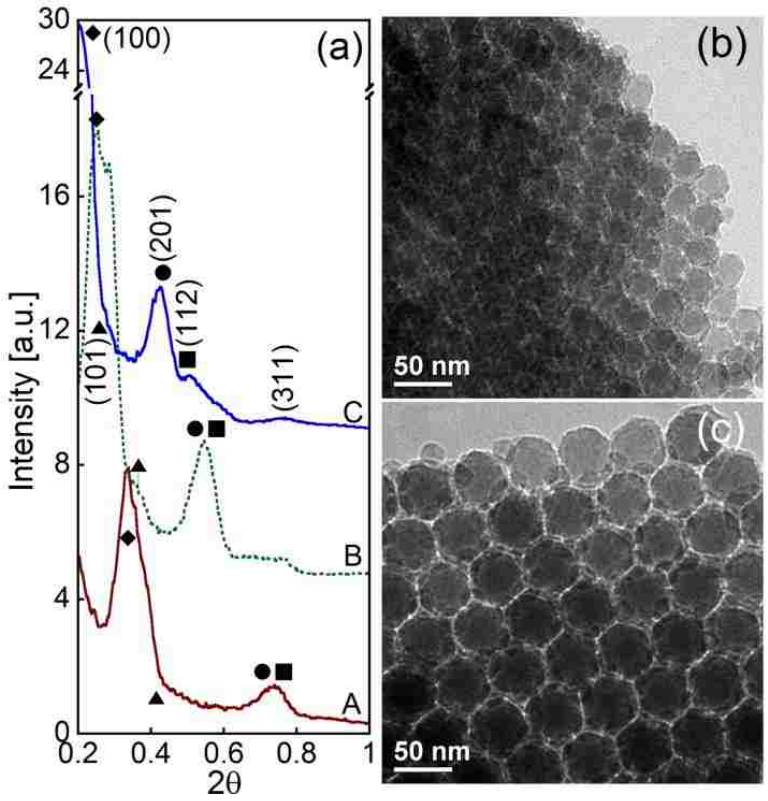

Figure 2-10. (a) 2D-SAXS data collected on binary silica nanoparticle assemblies showing persistence of AB_2-type AlB_2 isostructure upon tuning of constituent particle size (A: 15/32 nm, B: 19/41 nm, C: 23/50 nm) for a particle size ratio of approximately 0.46, and solution stoichiometry, N=2. Dominant reflections are indexed for case C, with symbols (diamond, circle, square, triangle) used to identify corresponding reflections in cases A and B. Representative TEM images along the [001] zone axis are shown for the case of (b) 15/32 nm and (c) 23/50 nm binary powders.

Confirmation of and insight into the independent tunability of pore topology and pore size of these materials is established by the nitrogen physisorption isotherms collected on representative AB-, AB_2-, and AB_{13}-structured powders (**Figure 2-11**a). Characteristic hysteresis loops observed in all cases are indicative of mesoporosity associated with the three-dimensionally interconnected interstices of the binary nanoparticle crystals. Corresponding BJH pore size distributions are shown for AB- and AB_{13}-type materials in **Figure 2-11**b and a series of AB_2-type materials compared with corresponding unary assemblies in **Figure 2-11**c. Specific textural properties are summarized in **Table 2-2**. In

general, the distribution of pore sizes is relatively narrow among all binary samples, consistent with the packing of highly monodisperse (i.e., polydispersity of ca. 5% or less) approximately spherical Lys-Sil particles.

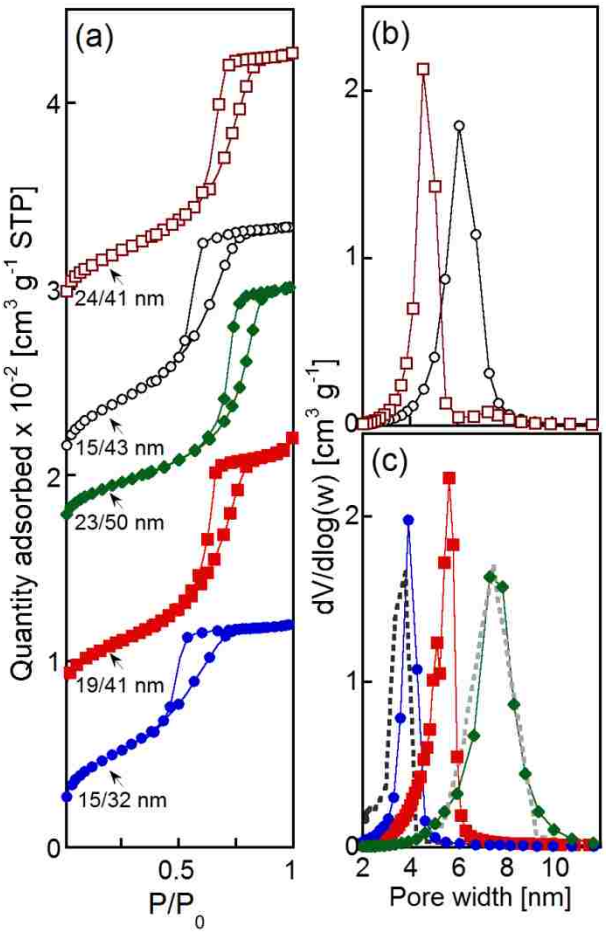

Figure 2-11. (a) Nitrogen physisorption isotherms collected on binary silica powders (shifted vertically for clarity) comprised of specified constituent particle sizes, with solid symbols, open circles, and open squares denoting stoichiometric AB2- (γ=0.47, N=2), AB- (γ=0.34, N=1), and AB13-type (γ=0.59, N=13) structures, respectively. BJH-based pore size distributions are shown for (b) AB and AB13-type structures as well as for (c) the three AB2 structures achieved by tuning particle size with γ~0.46. Dashed black and gray pore size distributions in (c) associated with unary colloidal crystal assemblies of 19 nm and 41 nm particles, respectively, are provided for reference.

Table 2-2. Textural properties of unary and binary silica colloidal crystals measured from nitrogen adsorption.

Nominal particle size [nm]	Total surface area [m^2/g][a]	Total pore volume [cm^3/g][b]	Mesopore volume [cm^3/g][c]
19	218.9	0.21	0.20
41	129.4	0.25	0.23
50	115.9	0.27	0.25
15/32	173.5	0.19	0.18
19/41	151.2	0.24	0.21
23/50	120.5	0.22	0.20
15/43	151.8	0.23	0.22
24/41	167.2	0.22	0.21

[a] Measured by BET analysis
[b] Calculated from the quantity adsorbed at P/P_0=0.995
[c] Calculated from t-plot analysis of the adsorption branch

Using the case of AB_2-type structures as a binary surrogate, we draw specific comparisons between the pore size distribution of the nominal binary 19/41 nm assembly and that measured for corresponding unary colloidal crystals, assembled from the individual constituent nanoparticles (see **Figure 2-12** for the corresponding adsorption isotherms collected for the unary crystals). The nominal pore size for the binary structure falls between those of the reference unary structures as a result of the difference in pore topology associated with the binary versus unary particle packing.

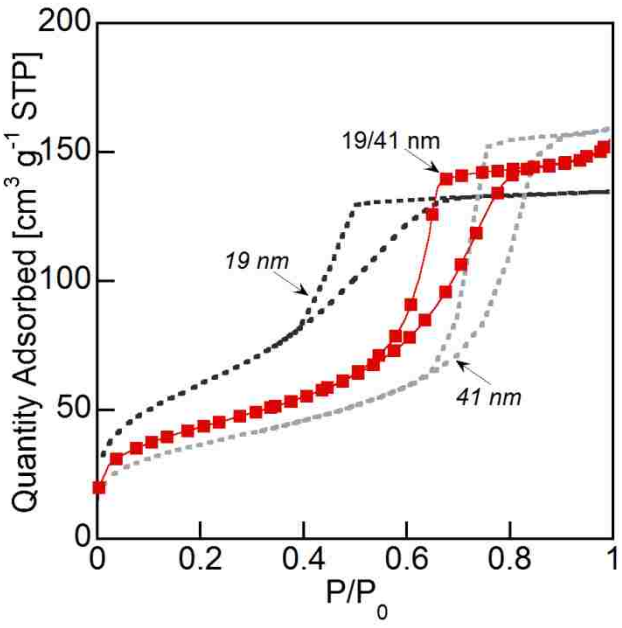

Figure 2-12. Comparison of nitrogen adsorption isotherms collected on unary colloidal crystal powders composed, separately, of 19 nm and 41 nm silica particles and the corresponding binary colloidal crystal powders achieved from co-assembly of the same silica particles from solutions of *N*=2 incipient stoichiometry.

Nitrogen adsorption also provides insight into the tunability of the pore size of the derived OMSs that is achievable by controlling the constituent particle size. **Figure 2-11**a shows nitrogen physisorption data collected for the AB_2 binary OMSs synthesized with ±20% perturbations in the nominal constituent particle sizes, but with fixed γ=0.47 and *N*=2. The concomitant increase in relative pressure, P/P_0, of the hysteresis loops with increasing particle size is consistent with the systematic tunability of pore size indicated by BJH analysis (**Figure 2-11**c). The pore size distributions for the two AB_2 structures, derived from the smallest and largest constituent particles studied, agree well with the respective pore size distributions measured on the small (19 nm) and large (41 nm) unary structures despite dramatic differences in pore topology. This ability to dial in a specific pore topology (e.g., AA, AB, AB_2., AB_{13}, solid AB solution) on the basis of particle size

ratio while independently tuning the pore size therein by simply controlling the size of both the small and large particles, underscores the versatility of the binary assembly process for realizing tunable OMSs.

2.3.4 Kinetic sensitivities of Lys-Sil binary assemblies

While we have shown how thermodynamics can be leveraged for realizing siliceous ordered binary assemblies in the case of Lys-Sil nanoparticles, mechanistic insight into competing kinetic effects is of practical importance for future applications. As such, we have studied how temperature and solvent evaporation may play a key role in tuning binary crystallinity. We have done this by perturbing the solvent evaporation temperature and pressure away from the nominal ambient conditions for which extensive single crystalline binary assembly is possible as demonstrated by the SEM and TEM images in **Figure 2-13**ab. Specifically, we have carried out stoichiometric (N=2) binary assembly by solvent evaporation for γ=19nm/41nm=0.47 under higher-temperature (40^{o}C) and lower-pressure/vacuum conditions (0.03 atm). Binary nanoparticle structures prepared by near doubling of the temperature during evaporative nanoparticle assembly display increased polycrystallinity (**Figure 2-13**c). This moderate temperature increase translates to enhanced diffusivity of the nanoparticles during assembly and a relatively moderate increase in the rate of solvent evaporation. Alternatively, as shown in **Figure 2-13**d, when vacuum conditions (P=0.03 atm) are imposed under ambient temperatures, completely disordered binary nanoparticle assemblies result. Here, introduction of vacuum conditions enhances solvent evaporation, driving more rapid particle assembly relative to the nominal case without enhancing nanoparticle diffusivity.

The results seem to elucidate two critical time scales dominating the kinetics of the system: the time scale associated with crystallization or local particle rearrangement required for realization of long-range ordered binary assembly, and the time scale associated with convective particle motion, driven by solvent evaporation, which delivers particles from the solution to the crystallization front. The qualitative analysis presented here suggests that the shorter the time scale for crystallization is relative to the time scale for nanoparticle convection, the greater is the achievable degree of single-crystallinity of the binary nanoparticle domains. In cases where the time scale for convection is reduced below that for crystallization (i.e., by driving fast solvent evaporation), we find that nanoparticles can be arrested in disordered binary states.

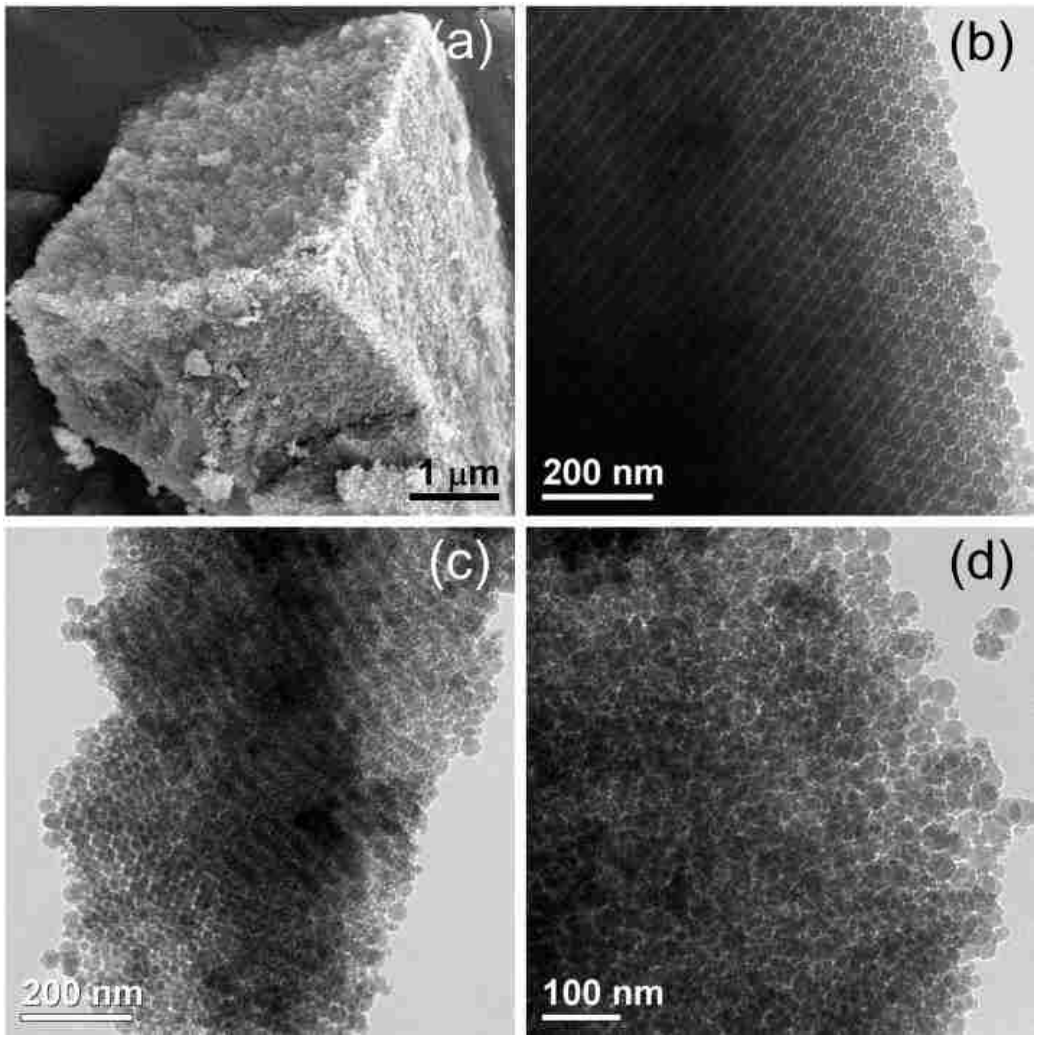

Figure 2-13. (a) SEM and (b) TEM images of bulk AB_2-type (γ=0.47 (19nm/41nm), *N*=2) binary silica colloidal crystals achievable through nominal evaporation-induced assembly at ambient temperature and pressure. TEM of polycrystalline and disordered binary colloidal crystals assembled, respectively, through solvent evaporation at (c) 40ºC and ambient pressure and (d) ambient temperature and vacuum conditions (P=0.03 atm).

2.4 Conclusions

By exploiting nanometer-resolved control over silica particle size ranging from ca. 10-50 nm, we have demonstrated a template-free route to a class of ordered mesoporous silicas (OMSs) comprised of assemblies of specific binary combinations of large (32-50 nm) and small (15-24 nm) spherical nanoparticles. Systematic control of the ratio of

particle size, γ, confirms the accessibility of AB_2 ($0.42 \leq \gamma <$ ca. 0.5) and AB_{13} ($0.54 \leq \gamma < 0.59$) phases predicted for hard-sphere systems. The additional accessibility of the AB phase at low γ ($\gamma < 0.42$), demonstrated here for the first time for the Lys-Sil system, gives rise to an AB-like interstitial solid solution wherein the cubic arrangement of the largest particles persists despite interstitially mobile smaller particles. 2D-SAXS and complementary TEM analysis reveal the long-range 3D order of the assemblies (e.g., binary-crystals of more than 1 μm in size), and help to identify the formation of NaCl, AlB_2, and $NaZn_{13}$ isostructures. The tunability of particle size enables independent control over pore size within the binary structures, demonstrated here for the ca. 2-10 nm pore size range, and selection of pore topology among AB, AB_2, AB_{13}, AB interstitial solid, and unary structures.

Ultimately, 1) the consistency of the experimentally-derived phase behavior (i.e., AB interstitial solids, AB, AB_2, AB_{13}) and phase boundaries (e.g., AB-AB_2 phase boundary at $\gamma = 0.42$) with hard-sphere predictions, 2) the measured insensitivity of the accessible binary solid phases to perturbations from half to twice the nominal particle stoichiometry in solution, and 3) the solid phase-selection based on the ratio, γ, rather than absolute size of the constituent particles, provide strong evidence that nanoparticle assembly within the Lys-Sil system is dominated by hard-sphere entropic effects. In addition, the processes of particle convection and local particle rearrangement (i.e., crystallization) offer competing time scales that tune the extent of binary crystallinity. Extended single crystals (> 1μm), as opposed to disordered binary aggregates, are achieved when the time scale for rearrangement is shorter than the time scale for particle convection to the drying/crystallization front, as controlled by temperature and vacuum/atmospheric

conditions. Together, these findings help elucidate the necessary theoretical framework and design rules for possible future exploitation of Lys-Sil nanoparticle assembly as a bottom-up route to a new class of OMS materials with independently tunable pore size and topology.

2.5 Reference

1. Beck, J. S.; Vartuli, J. C.; Roth, W. J.; Leonowicz, M. E.; Kresge, C. T.; Schmitt, K. D.; Chu, C. T. W.; Olson, D. H.; Sheppard, E. W.; McCullen, S. B.; Higgins, J. B.; Schlenker, J. L., A new family of mesoporous molecular-sieves prepared with liquid-crystal templates. *Journal of the American Chemical Society* **1992,** 114, (27), 10834-10843.

2. Chiola, V. R., J. E. and Vanderpool, C. D. Process for producing low-bulk density silica. US 3556725, Jan-19, 1971.

3. Zhao, D. Y.; Huo, Q. S.; Feng, J. L.; Chmelka, B. F.; Stucky, G. D., Nonionic triblock and star diblock copolymer and oligomeric surfactant syntheses of highly ordered, hydrothermally stable, mesoporous silica structures. *Journal of the American Chemical Society* **1998,** 120, (24), 6024-6036.

4. Zhao, D. Y.; Feng, J. L.; Huo, Q. S.; Melosh, N.; Fredrickson, G. H.; Chmelka, B. F.; Stucky, G. D., Triblock copolymer syntheses of mesoporous silica with periodic 50 to 300 angstrom pores. *Science* **1998,** 279, (5350), 548-552.

5. Huo, Q. S.; Margolese, D. I.; Ciesla, U.; Feng, P. Y.; Gier, T. E.; Sieger, P.; Leon, R.; Petroff, P. M.; Schuth, F.; Stucky, G. D., Generalized synthesis of periodic surfactant inorganic composite-materials. *Nature* **1994,** 368, (6469), 317-321.

6. Matos, J. R.; Kruk, M.; Mercuri, L. P.; Jaroniec, M.; Zhao, L.; Kamiyama, T.; Terasaki, O.; Pinnavaia, T. J.; Liu, Y., Ordered mesoporous silica with large cage-like pores: Structural identification and pore connectivity design by controlling the synthesis temperature and time. *Journal of the American Chemical Society* **2003,** 125, (3), 821-829.

7. Kleitz, F.; Liu, D. N.; Anilkumar, G. M.; Park, I. S.; Solovyov, L. A.; Shmakov, A. N.; Ryoo, R., Large cage face-centered-cubic Fm3m mesoporous silica: Synthesis and structure. *Journal of Physical Chemistry B* **2003,** 107, (51), 14296-14300.

8. Fan, J.; Yu, C. Z.; Gao, T.; Lei, J.; Tian, B. Z.; Wang, L. M.; Luo, Q.; Tu, B.; Zhou, W. Z.; Zhao, D. Y., Cubic mesoporous silica with large controllable entrance sizes and advanced adsorption properties. *Angewandte Chemie-International Edition* **2003,** 42, (27), 3146-3150.

9. Kim, S. S.; Karkamkar, A.; Pinnavaia, T. J.; Kruk, M.; Jaroniec, M., Synthesis and characterization of ordered, very large pore MSU-H silicas assembled from water-soluble silicates. *Journal of Physical Chemistry B* **2001,** 105, (32), 7663-7670.

10. Tanev, P. T.; Pinnavaia, T. J., A neutral templating route to mesoporous molecular-sieves. *Science* **1995,** 267, (5199), 865-867.

11. Poyraz, A. S.; Kuo, C. H.; Biswas, S.; King'ondu, C. K.; Suib, S. L., A general approach to crystalline and monomodal pore size mesoporous materials. *Nature Communications* **2013,** 4, 10.

12. Yu, C. Z.; Yu, Y. H.; Zhao, D. Y., Highly ordered large caged cubic mesoporous silica structures templated by triblock PEO-PBO-PEO copolymer. *Chemical Communications* **2000**, (7), 575-576.

13. Matos, J. R.; Kruk, M.; Mercuri, L. P.; Jaoniec, M.; Asefa, T.; Coombs, N.; Ozin, G. A.; Kamiyama, T.; Terasaki, O., Periodic mesoporous organosilica with large cagelike pores. *Chemistry of Materials* **2002,** 14, (5), 1903-1905.

14. Kim, T. W.; Ryoo, R.; Kruk, M.; Gierszal, K. P.; Jaroniec, M.; Kamiya, S.; Terasaki, O., Tailoring the pore structure of SBA-16 silica molecular sieve through the use of copolymer blends and control of synthesis temperature and time. *Journal of Physical Chemistry B* **2004,** 108, (31), 11480-11489.

15. Bardosova, M.; Pemble, M. E.; Povey, I. M.; Tredgold, R. H., The Langmuir-Blodgett Approach to Making Colloidal Photonic Crystals from Silica Spheres. *Adv. Mater.* **2010,** 22, (29), 3104-3124.

16. Li, F.; Josephson, D. P.; Stein, A., Colloidal Assembly: The Road from Particles to Colloidal Molecules and Crystals. *Angewandte Chemie-International Edition* **2011,** 50, (2), 360-388.

17. Davis, T. M.; Snyder, M. A.; Krohn, J. E.; Tsapatsis, M., Nanoparticles in lysine-silica sols. *Chemistry of Materials* **2006,** 18, (25), 5814-5816.

18. Snyder, M. A.; Lee, J. A.; Davis, T. M.; Scriven, L. E.; Tsapatsis, M., Silica nanoparticle crystals and ordered coatings using lys-sil and a novel coating device. *Langmuir* **2007,** 23, (20), 9924-9928.

19. Fan, W.; Snyder, M. A.; Kumar, S.; Lee, P. S.; Yoo, W. C.; McCormick, A. V.; Penn, R. L.; Stein, A.; Tsapatsis, M., Hierarchical nanofabrication of microporous crystals with ordered mesoporosity. *Nature Materials* **2008,** 7, (12), 984-991.

20. Yokoi, T.; Sakamoto, Y.; Terasaki, O.; Kubota, Y.; Okubo, T.; Tatsumi, T., Periodic arrangement of silica nanospheres assisted by amino acids. *Journal of the American Chemical Society* **2006,** 128, (42), 13664-13665.

21. Yokoi, T.; Wakabayashi, J.; Otsuka, Y.; Fan, W.; Iwama, M.; Watanabe, R.; Aramaki, K.; Shimojima, A.; Tatsumi, T.; Okubo, T., Mechanism of Formation of Uniform-Sized Silica Nanospheres Catalyzed by Basic Amino Acids. *Chemistry of Materials* **2009,** 21, (15), 3719-3729.

22. Sanders, J. V., Close-packed structures of spheres of 2 different sizes. 1. observations on natural opal. *Philosophical Magazine a-Physics of Condensed Matter Structure Defects and Mechanical Properties* **1980,** 42, (6), 705-720.

23. Murray, M. J.; Sanders, J. V., Close-packed structures of spheres of 2 different sizes. 2. the packing densities of likely arrangments. *Philosophical Magazine a-Physics of Condensed Matter Structure Defects and Mechanical Properties* **1980,** 42, (6), 721-740.

24. Eldridge, M. D.; Madden, P. A.; Frenkel, D., Entropy-driven formation of a superlattice in a hard-sphere binary mixture. *Nature* **1993,** 365, (6441), 35-37.

25. Eldridge, M. D.; Madden, P. A.; Frenkel, D., A computer-simulation investigation into the stability of the ab2 superlattice in a binary hard-sphere system. *Mol. Phys.* **1993,** 80, (4), 987-995.

26. Trizac, E.; Eldridge, M. D.; Madden, P. A., Stability of the AB crystal for asymmetric binary hard sphere mixtures. *Mol. Phys.* **1997,** 90, (4), 675-678.

27. Cottin, X.; Monson, P. A., Substitutionally ordered solid-solutions of hard-spheres. *J. Chem. Phys.* **1995,** 102, (8), 3354-3360.

28. Shevchenko, E. V.; Talapin, D. V.; Murray, C. B.; O'Brien, S., Structural characterization of self-assembled multifunctional binary nanoparticle superlattices. *Journal of the American Chemical Society* **2006,** 128, (11), 3620-3637.

29. Chen, Z. Y.; Moore, J.; Radtke, G.; Sirringhaus, H.; O'Brien, S., Binary nanoparticle superlattices in the semiconductor-semiconductor system: CdTe and CdSe. *Journal of the American Chemical Society* **2007,** 129, (50), 15702-15709.

30. Chen, Z.; O'Brien, S., Structure direction of II-VI semiconductor quantum dot binary nanoparticle superlattices by tuning radius ratio. *Acs Nano* **2008,** 2, (6), 1219-1229.

31. Bodnarchuk, M. I.; Kovalenko, M. V.; Heiss, W.; Talapin, D. V., Energetic and Entropic Contributions to Self-Assembly of Binary Nanocrystal Superlattices: Temperature as the Structure-Directing Factor. *Journal of the American Chemical Society* **2010,** 132, (34), 11967-11977.

32. Evers, W. H.; De Nijs, B.; Filion, L.; Castillo, S.; Dijkstra, M.; Vanmaekelbergh, D., Entropy-Driven Formation of Binary Semiconductor-Nanocrystal Superlattices. *Nano Lett.* **2010,** 10, (10), 4235-4241.

33. Kitaev, V.; Ozin, G. A., Self-assembled surface patterns of binary colloidal crystals. *Adv. Mater.* **2003,** 15, (1), 75-+.

34. Kim, M. H.; Im, S. H.; Park, O. O., Rapid fabrication of two- and three-dimensional colloidal crystal films via confined convective assembly. *Advanced Functional Materials* **2005,** 15, (8), 1329-1335.

35. Bartlett, P.; Ottewill, R. H.; Pusey, P. N., Superlattice formation in binary-mixtures of hard-sphere colloids. *Phys. Rev. Lett.* **1992,** 68, (25), 3801-3804.

36. Hunt, N.; Jardine, R.; Bartlett, P., Superlattice formation in mixtures of hard-sphere colloids. *Phys. Rev. E* **2000,** 62, (1), 900-913.

37. Vermolen, E. C. M.; Kuijk, A.; Filion, L. C.; Hermes, M.; Thijssen, J. H. J.; Dijkstra, M.; van Blaaderen, A., Fabrication of large binary colloidal crystals with a NaCl structure. *Proc. Natl. Acad. Sci. U. S. A.* **2009,** 106, (38), 16063-16067.

38. Singh, G.; Pillai, S.; Arpanaei, A.; Kingshott, P., Layer-by-Layer Growth of Multicomponent Colloidal Crystals Over Large Areas. *Advanced Functional Materials* **2011,** 21, (13), 2556-2563.

39. Kuroda, Y.; Sakamoto, Y.; Kuroda, K., Selective Cleavage of Periodic Mesoscale Structures: Two-Dimensional Replication of Binary Colloidal Crystals into Dimpled Gold Nanoplates. *Journal of the American Chemical Society* **2012,** 134, (20), 8684-8692.

40. Saunders, A. E.; Korgel, B. A., Observation of an AB phase in bidisperse nanocrystal superlattices. *ChemPhysChem* **2005,** 6, (1), 61-65.

41. Iler, R. K., *The Chemistry of Silica: Solubility, Polymerization, Colloid and Surface Properties and Biochemistry of Silica*. Wiley-Interscience: 1979.

42. Coronas, J.; Santamaria, J., Separations using zeolite membranes. *Sep. Purif. Methods* **1999,** 28, (2), 127-177.

43. Atchison, N.; Fan, W.; Brewer, D. D.; Arunagirinathan, M. A.; Hering, B. J.; Kumar, S.; Papas, K. K.; Kokkoli, E.; Tsapatsis, M., Silica-Nanoparticle Coatings by Adsorption from Lysine-Silica-Nanoparticle Sols on Inorganic and Biological Surfaces. *Angewandte Chemie-International Edition* **2011,** 50, (7), 1617-1621.

44. Vlasova, N. N.; Golovkova, L. P., The adsorption of amino acids on the surface of highly dispersed silica. *Colloid Journal* **2004,** 66, (6), 657-662.

45. Gao, Q.; Xu, W. J.; Xu, Y.; Wu, D.; Sun, Y. H.; Deng, F.; Shen, W. L., Amino acid adsorption on mesoporous materials: Influence of types of amino acids, modification of mesoporous materials, and solution conditions. *Journal of Physical Chemistry B* **2008,** 112, (7), 2261-2267.

46. Kitadai, N.; Yokoyama, T.; Nakashima, S., ATR-IR spectroscopic study of L-lysine adsorption on amorphous silica. *Journal of Colloid and Interface Science* **2009,** 329, (1), 31-37.

47. Ben-Simon, A.; Eshet, H.; Rabani, E., On the Phase Behavior of Binary Mixtures of Nanoparticles. *Acs Nano* **2013,** 7, (2), 978-986.

Chapter 3:

Elucidation of Stability and Ordered Assembly Limits for Binary Lys-Sil Bulk and Thin-Film Structures

3.1 Introduction

The synthesis of monodispersed colloidal silica spheres in the micron size range was demonstrated by Stöber in 1968 by base-catalyzed hydrolysis and condensation of tetraethylorthosilicate (TEOS) with ammonia in ethanol/water solutions[1], and it has been studied extensively since. Recently we[2-4] and others[5, 6] have demonstrated how the micron to sub-micron colloidal silica particle size achievable via the Stöber process can be scaled down to particles on the order of 10 nm, termed Lys-Sil nanoparticles, via aqueous-phase amino acid-assisted synthesis. The ability to assemble monodisperse colloidal spheres, with particle sizes spanning from several microns to tens of nanometers, into colloidal crystal structures bearing different symmetries (e.g., face-centered cubic (fcc) and hexangonal close-packed (hcp) unary colloidal crystals, binary colloidal crystals isostructural with AB, AB_2, AB_{13}) have found a broad range of applications, including photonic bandgap (PBG) crystals, nanoscale electronics, drug delivery, and hierarchically structured catalysts[7-9].

Colloidal stability plays an important role in particle assembly into highly ordered colloidal crystal structures, and is ultimately dependent upon the interplay between attractive and repulsive forces[10-12]. Specifically, van der Waals forces lead to short-range interparticle attraction, promoting particle aggregation. Depletion forces, owing to increase in osmotic pressure resulting when larger particles come close enough to exclude smaller co-solutes or so-called "depletants" (e.g., particles, molecules), give rise to an additional possible interparticle attraction. These forces can be counterbalanced by repulsive interparticle forces owing to electrostatics and/or steric stabilization. A balance between these attractive and repulsive forces is critical for realization of long-range ordered colloidal crystal assembly instead of disordered aggregation.

In the case of silica nanoparticles, repulsive interparticle forces derive from their intrinsically negative surface charge, the magnitude of which is associated with the degree of dissociation of terminal silanol groups on the particle surface. In general, surface charge on the silica surface increases with increasing pH as an increasing number of silanol groups undergo deprotonation ($Si\text{-}OH \rightarrow Si\text{-}O^- + H^+$). Experimentally, the surface charge can be estimated by measuring the electrostatic surface potential, termed the zeta potential (ζ), of silica sols[13] by the electrophoretic method.

In Chapter 2, we demonstrated how the realization of all three hard-sphere binary phases (AB, AB_2, and AB_{13}) was linked exclusively to the particle size ratio, γ, was insensitive to the solution phase particle stoichiometry, *N*, as well as changing particle sizes (i.e., while holding γ constant), and did not require complex charge stabilization, steric stabilization, or minimization of van der Waals attractions beyond conditions intrinsic to the Lys-Sil solutions. This suggested that nanoparticle assembly in the Lys-Sil system is

governed by entropy-dominated hard-sphere effects. The focus of this chapter is two-fold. First, we aim to further elucidate the theoretical underpinnings that endow the Lys-Sil system with this hard-sphere character despite the apparent particle size dependence of particle charge (see **Figure 2-1**b) and assertion by previous studies (e.g., Refs. [5, 6]) that lysine-mediated hydrogen bonding may be critical in facilitating particle assembly. Second, we describe and study apparent sensitivities of the binary assembly to 1) system aging and 2) chemical composition of the substrate upon which assemblies are prepared.

3.2 Experimental

3.2.1 Synthesis, dialysis, aging and pH titration of silica nanoparticle solutions

Silica nanoparticles (Lys-Sil nanoparticles) of different particle sizes were synthesized using lysine (Sigma Aldrich, 98%)-mediated hydrolysis of tetraethylorthosilicate (TEOS, 98%, Sigma-Aldrich) in aqueous solutions as described in Chapter 2. Dialysis of the Lys-Sil sols was carried out against water using Spectra/Por tubes (Spectrumlabs, Spectra/Por 3, 3.5kD MWCO) to contact the sol with a ca. 1L water bath. The water was exchanged for fresh water daily until the measured pH of the water reached a constant value consistent with that of purified water (i.e., pH~5.5). Millipore water with resistivity 18 MΩ was used for all solutions, dilutions, and dialysis. The aging of dialyzed silica sols at ambient conditions was carried out by storing 10 mL dialyzed silica sol in 50 mL plastic containers with parafilm-sealed caps for prescribed time periods spanning 0 to 28 days.

Studies in which the role of lysine and another basic amino acid, L-arginine, were explored, involved the reloading of lysine and arginine into dialyzed sols. This was carried

out by preparing a concentrated stock solution (0.5M) of each amino acid and adding a prescribed volume of that stock solution to the dialyzed sol in order to reach molar amino acid concentrations of 0.5, 1, and 3 times the nominal molar lysine loading in the synthesis solution, the latter specified in Chapter 2 as 61.5 SiO_2 : 1.23 Lysine : 9500 water : 240 ethanol. Thus, the compositions of the dialyzed solutions with 0.5, 1, and 3 times the nominal molar lysine loading were 61.5 SiO_2 : *y* Lysine : 9500 water, where *y*= 0.615, 1.23, and 3.69, respectively.

Systematic titration of sols to higher and lower pH was also carried out to study the role of pH on the ability to achieve ordered binary and unary nanoparticle assemblies. The pH of the as-made Lys-Sil and dialyzed silica sols were adjusted by drop-wise addition of 0.2M sodium hydroxide (NaOH) or 0.2M hydrochloric acid (HCl) aqueous solutions to the nanoparticle sols until target pH values were reached.

3.2.2 Convective deposition of films of binary Lys-Sil nanoparticles

Bulk unary and binary nanoparticle assemblies discussed in this Chapter were achieved as described in Chapter 2 and Refs. 2, 3, 14 by solvent evaporation under ambient conditions from sols contained in polystyrene containers. Here, we have carried out sensitivity analysis by focusing our attention on the nominal AB_2 assemblies derived, in the nominal case, from stoichiometric mixtures of 40 nm and 20 nm Lys-Sil nanoparticles. In cases where we have explored the structural sensitivity of binary assemblies to thin film casting, we have employed a blade-based convective deposition process detailed in Refs. 15, 16. Generally, the blade coating system setup employs a glass microscope slide as a coating blade, fixed approximately 0.5 mm above and at an angle of 45° to an underlying

substrate. Depositions of the dialyzed silica nanoparticles were prepared on glass slides (76 x 25 x 1 mm, Fisher Scientific), silicon wafers (Silicon Quest), or carbon-coated silicon wafers. In the case of bare glass or silicon wafers, prior to convective deposition the substrates were soaked in piranha solution (4:1 v./v. sulfuric acid/ hydrogen peroxide) for two hours to dissolve any organic impurities, and dried subsequently with dry nitrogen. Binary silica nanoparticle films were prepared by injecting 50μL of pre-made binary silica sols into the wedge between the coating blade and the substrate, the former fixed at an angle of 45° relative to the substrate. Coatings were prepared under ambient conditions by advancing the substrate at a rate 10 μm/s.

Studies of the role of surface energy in the binary deposition involved use of carbon-coated silicon wafers. These were prepared according to Ref. 16 by suspending a silicon wafer horizontally 0.5 inches above a pool of furfuryl (FA) and oxalic acid (OA) solution in a sealed plastic beaker (molar ratio: FA:OA=100:1). The sealed beaker was heated at 90℃ for 72 hrs to deposit FA/OA monomer vapor on the silicon wafer, and to polymerize the deposited monomer. The resulting silicon-wafer-supported polyfurfuryl (PFA) films were carbonized in a tube furnace at 900 ℃ (5 ℃/min ramp) for 3 hours under flowing nitrogen (1.5 L/min).

3.2.3 Characterization

Zeta potential analysis of silica sols was carried out with a ZetaPALS, Brookhaven Instruments Corporation zeta potential analyzer. Silica nanoparticle solutions were loaded in transparent polystyrene cuvettes (SARSTEDT, 67.754) with insertion of the conductive probe for application of an electric field to drive nanoparticles mobility. 35-50 cycles were

collected per run, and the averaged zeta potentials were calculated from the data points from ten runs per measurement. Fourier Transform Infrared (FT-IR) spectroscopy of silica sols was obtained on an FT-IR spectrometer (Thermo Scientific, Nicolet iS 10). Samples were loaded by dropping approximate 1mL of solution on the ZnSe crystal sampling area, and spectrums were collected with wavenumbers between 900 and 4000. Thermal analysis was conducted on a simultaneous thermogravimetric analysis-differential scanning calorimeter (TGA-DSC, TA Instruments SDT Q600). Approximately 20mg of dried fine powder was loaded in the alumina pan, and the sample was heating up to 550 ℃ (10 ℃/min ramp) under flowing dry air (100 mL/min). TEM images of dried silica nanoparticle powders and films were collected on a JEOL 2000FX to study the microstructure of the samples. The pH of each solution was measured by on an ORION 4 STAR (Thermo Scientific) pH/conductivity meter. Contact angle measurements using Millipore water with resistivity 18 MΩ were carried out using a modified Rame-Hart 100 contact angle goniometer. Sample solutions were dropped on the measured surface by manual microsyringe, and the image of the droplet on the surface was recorded by a digital CCD camera and analyzed by ImageJ to estimate the contact angle.

3.3 Results and discussion

3.3.1 Elucidating the role of solution composition on binary assembly: Lysine (arginine) and ethanol

As-made Lys-Sil sols are composed of amorphous silica nanoparticles (10-50 nm), adsorbed lysine on the silica surface[17-19], freely dispersed lysine in solution, water, and ethanol liberated during TEOS hydrolysis. In order to better understand the role of Lysine in the assembly of binary and unary colloidal crystals from Lys-Sil nanoparticle sols, we employed dialysis of the as-made Lys-Sil nanoparticle solutions to remove freely dispersed lysine in addition to ethanol. The resulting purified solutions of silica nanoparticles were found to be structurally and colloidally stable for weeks at a time[20].

Zeta potential analysis was carried out on the representative as-made Lys-Sil dialyzed nanoparticle sols composed of primary silica particles of 20 and 40 nm in diameter as shown in **Figure 3-1**a. The larger ca. 40 nm Lys-Sil nanoparticles, produced by seeded growth, bear a zeta potential of approximately -40 mV that is fairly insensitive to dialysis, and appears sufficient to counterbalance destabilizing dispersion forces during unary assembly. While the 20 nm Lys-Sil nanoparticles in the as-made solution are endowed with a strongly negative zeta potential (ca. -100 mV), lysine removal by dialysis (open circle labeled 'D') leads to a precipitous reduction in the magnitude of the zeta potential (ca. -30 mV).

We hypothesize that the apparent dependence of particle charge on particle size is actually a result of either surface adsorption of lysine or by its physical encapsulation within the volume of the silica particle during the seeded particle growth. Specifically, the seeded growth of particles larger than ca. 20 nm is carried out by sequential hydrolysis of

TEOS without the replenishment of lysine beyond that which was employed in the synthesis of the seed particles. The solvated lysine content in solution is, therefore, anticipated to be higher in the case of the smallest particles than for the largest particles, since less physical encapsulation of lysine should occur. As such, the zeta potential measured for the smallest particles is more dramatically influenced by removal of free lysine by dialysis than in the case of the larger particles.

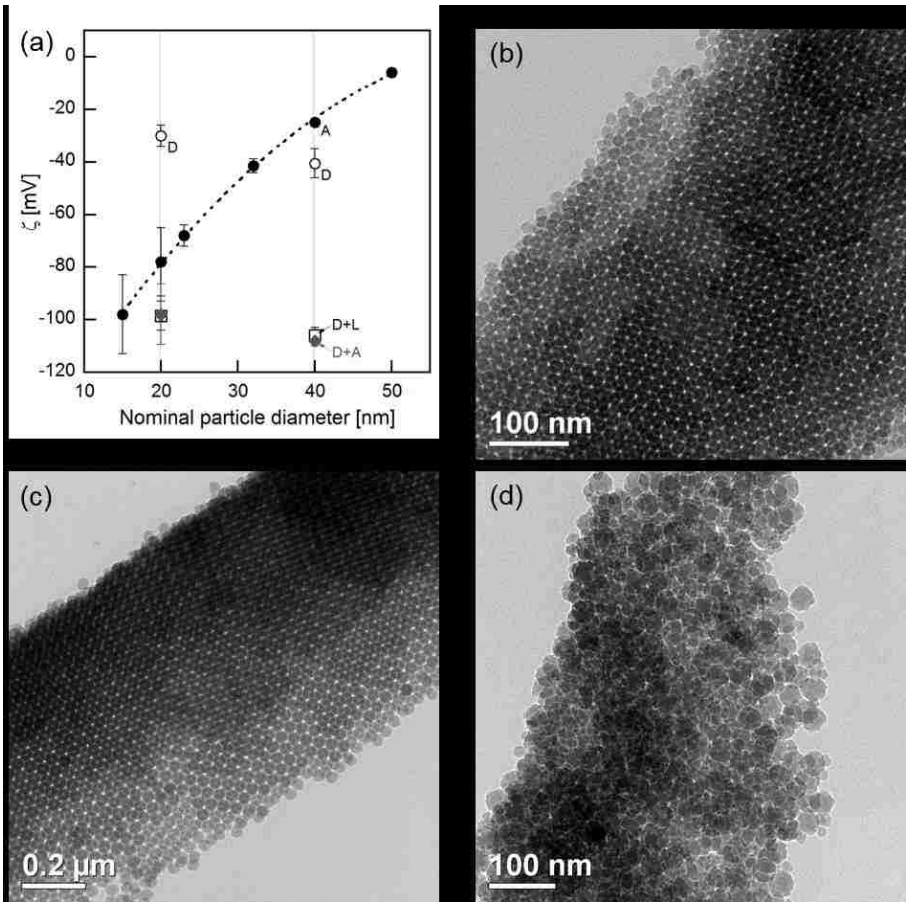

Figure 3-1. (a) Zeta potential of silica sols; where the error bars indicate the standard deviation from each measurement with 10 runs. TEM images of unary (b) 20nm, (c) 40nm, and (d) binary 20/40nm silica assembly

The assembly of dialyzed silica sols was investigated by the evaporation-induced assembly process under ambient conditions and characterized by TEM. **Figure 3-1**bcd show the TEM images of dried dialyzed silica sols composed of unary and binary silica nanoparticles. While unary assembly of the dialyzed small (20nm, **Figure 3-1**b) and large (40nm, **Figure 3-1**c) particles leads to ordered nanoparticle crystals, we find that binary nanoparticle assembly results in disordered binary structures. Specifically, TEM images in **Figure 3-1**d for the representative assembly from an N=2 stoichiometric solution with a particle size ratio of γ~0.5, reveal the resulting disordered binary assemblies. These data suggest that the unary assembly from freshly dialyzed sols is insensitive to purification of the sols of the free lysine and ethanol whereas the binary assembly is highly sensitive to the solution composition.

The purified sols provide the basis for systematic and decoupled study of the role of lysine and ethanol in the system, which has been accomplished by reloading of lysine or ethanol to levels consistent with the as-made sols. Whereas addition of ethanol back into the dialyzed system results also in disordered binary assemblies (not shown), addition of lysine (**Figure 3-2**ab), or even arginine (**Figure 3-2**cd), another basic and zwitterionic amino acid used in earlier[21] studies for complementary synthesis of silica nanoparticles, enables a striking recovery of long-range unary and binary nanoparticle order. This recovery of binary order is achieved for fractional (0.5x) as well as excess (3x) levels (shown in **Figure 3-2**e-h) of the basic amino acid relative to the nominal composition of the as-made sols. As shown in **Figure 3-1**a, re-introduction of either lysine or arginine, at nominal levels employed in the synthesis leads to recovery of the highly negative zeta

potential for the smallest particles (ζ~-100 mV) and dramatically enhanced zeta potential of the largest particles (ζ~-110 mV).

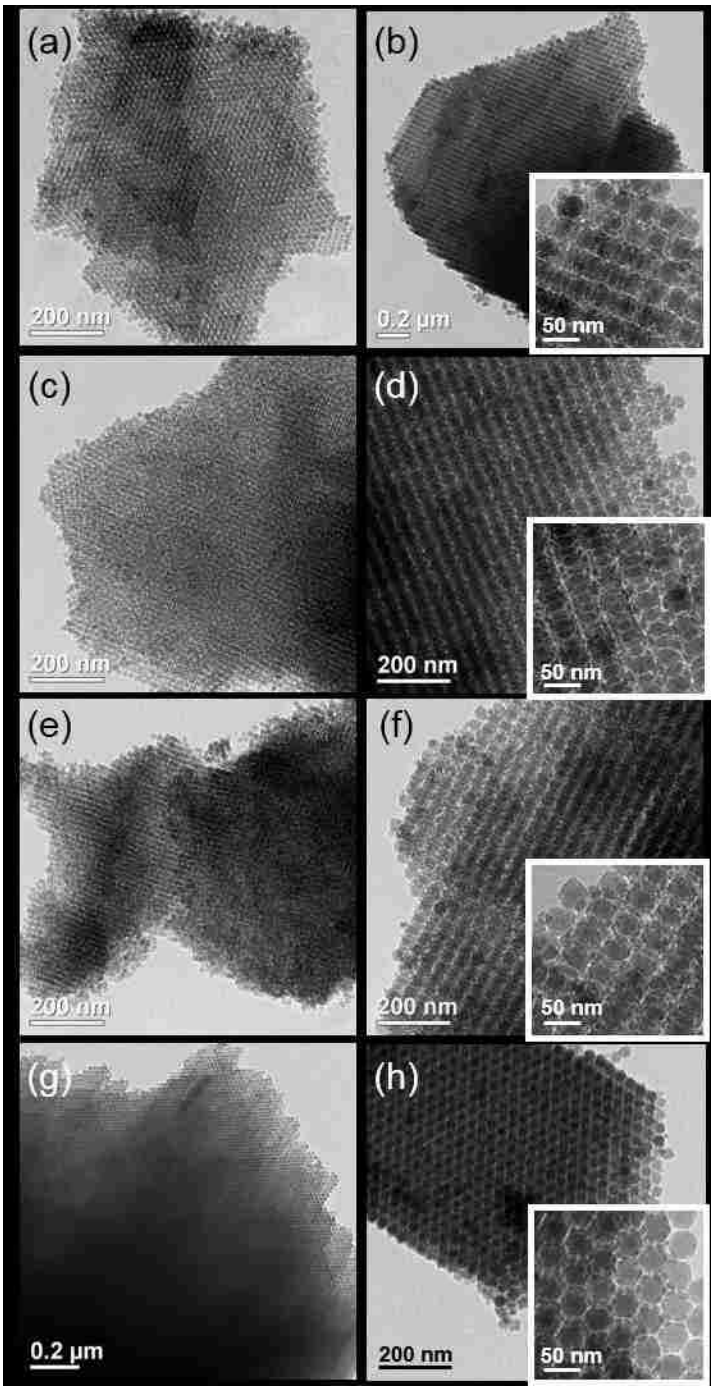

Figure 3-2. TEM images of dialyzed silica sols with back-addition of 1X lysine (a: unary 20nm; b: binary 20/40nm), 1X arginine (c: unary 20nm; d: binary 20/40nm), 0.5X lysine (e: unary 20nm; f: binary 20/40nm), and 3X lysine (g: unary 20nm; h: binary 20/40nm). Insets: ordered binary 20/40nm at higher magnification

Earlier work[6] for unary assembly of Lys-Sil nanoparticles has suggested that lysine contributes hydrogen bonding to aid in the ordered nanoparticle assembly. As a basic amino acid it also buffers the sol to pH~9, conditions for which silanol deprotanation occurs. In addition, the dependence of the dissociation states of lysine on the pH of the solution (see **Figure 3-3** reprinted from Ref.[17]) suggests that at pH~9, zwitterionic and cationic lysine molecules coexist in the silica sols, with a major fraction (~80%) of cationic lysine adsorbing to the silica surface as a result of electrostatic interaction with deprotonated silanol groups[17-19].

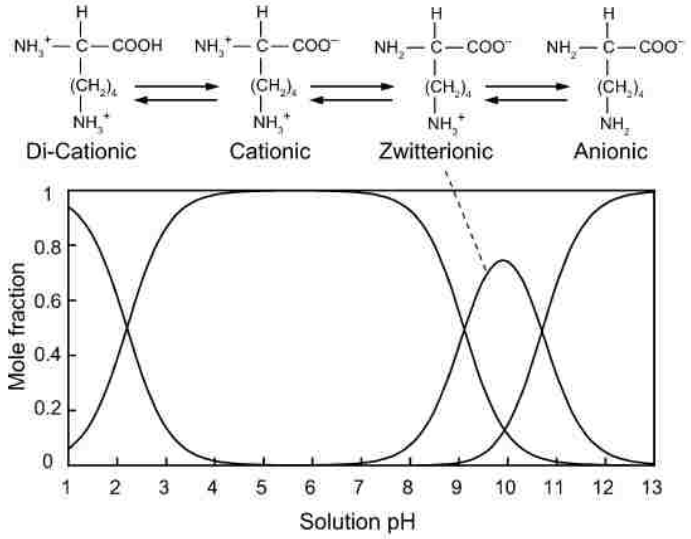

Figure 3-3. Dissociation states of dissolved lysine as a function of pH (reprinted from Ref.[17])

The multicomponent and multifaceted nature of the system motivates efforts to systematically decouple the possible effects of adsorbed lysine (e.g., steric stabilization, inter-particle hydrogen bonding) from electrostatics in, on the one hand, stabilization of the Lys-Sil nanoparticles at levels sufficient to realize ordered binary assemblies, and, on

the other hand, destabilization of binary systems in the absence of lysine. For insight into the role of lysine in the Lys-Sil nanoparticle sols and its fate in dialyzed samples for which concomitant binary assemblies are disordered, **Figure 3-4** shows the result of TGA analysis carried out on as-made and dialyzed 20 and 40nm silica, which were dried at 70 ℃ in the oven. Signature features in this lysine-silica system include desorption of physically adsorbed water beginning at ~100 ℃ (indicated by grey dashed line *2), weight loss due to decomposition of lysine starting from ~225 ℃[22] (see TGA analysis of lysine powders shown in **Figure 3-4**a, indicated by grey dashed line *1), and dehydration of silica (i.e., transformation of silanol groups to siloxane bonds) starting at ~180 ℃[23].

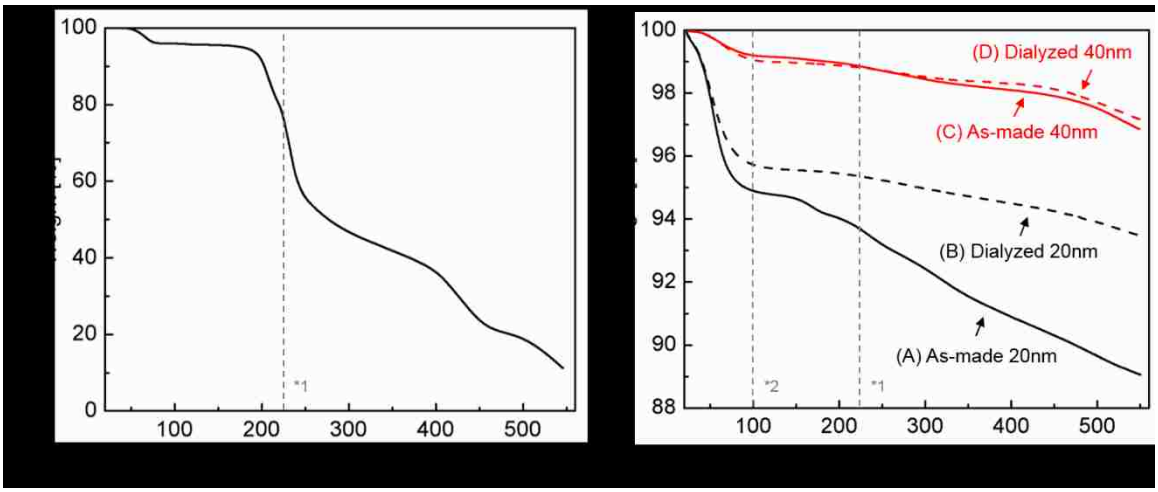

Figure 3-4. TGA analysis of (a) lysine powder, and (b) silica powders dried from (A) as-made 20nm, (B) dialyzed 20nm, (C) as-made 40nm, and (D) dialyzed 40nm silica sols (grey dashed line *1 and *2 indicate decomposition of lysine molecules, and the desorption of physically adsorbed water, respectively)

In the case of the as-made 20nm (A) and dialyzed 20nm (B) silica samples, **Figure 3-4**b shows that both undergo loss of physically adsorbed water between 25 to 100 ℃. Lysine in as-made silica (~4 weight %) starts to decompose after 200 ℃, and this occurs simultaneously with the dehydration of the silica surface (~3 weight %). The lack of significant weight loss in the case of the dialyzed silica around the decomposition point of lysine suggests that the slight subsequent weight loss (~2%) is due to dehydration of the silica surface. These data indicate that there is no or only trace amounts of lysine remaining in the dialyzed silica sols.

In the case of the as-made 40nm (C) and dialyzed 40nm (D) silica samples in **Figure 3-4**b, both weight loss profiles almost overlap until after 200 ℃, indicating lysine in as-made sample starts to decompose. It is worth noting that the weight fraction of lysine in the as-made 40nm silica samples is about 0.6%, and the weight loss difference between as-made and dialyzed 40nm according to TGA analysis is 0.3%, which confirms that part

of lysine molecules are physically encapsulated inside the 40nm particles during the seeded growth synthesis by using 20nm silica nanoparticles as the seeds, and was unable to be removed by the dialysis purification process.

This TGA analysis suggests that lysine is removed from the surface of the Lys-Sil particles upon dialysis. According to the analysis in **Figure 3-1**, the absence of both free and adsorbed lysine corresponds to destabilization of the binary assembly whereas unary assemblies of the large and small particles remain ordered. The absence of adsorbed lysine confirmed by the TGA analysis suggests that the disorder in the binary assembly could derive, at least in part, from the concomitant removal of any steric stabilization imparted by lysine. Yet, the unary assemblies remain ordered, suggesting that electrostatics and pH effects may play a more important role especially given the small size (MW=146.19 g/mol), and thus unclear steric influence, of lysine.

3.3.2 Effect of pH and electrostatic stabilization on unary and binary particle assembly

In order to better understand the role of pH in unary and binary assembly of silica nanoparticles, the measured dependence of zeta-potential on pH for titrated as-made and dialyzed sols is shown in **Figure 3-5**. In the case of as-made 20 and 40 nm Lys-Sil sols (denoted as 20nm-A and 40nm-A, respectively), lysine buffers the solution to pH~9-10 (as indicated by solid points). Such basic conditions lead to strongly dissociated silanol groups ($Si\text{-}OH \rightarrow SiO^- + H^+$) where $[H^+]$ ions were buffered by lysine molecules, thus resulting in highly negatively charged silica. Dialyzed silica sols (denoted as 20nm-D and 40nm-D) were weakly acidic (pH~5) immediately after dialysis due to the lower level of dissociation of $[H^+]$ from silanol groups on the silica surface, resulting in less negatively charged silica.

To decouple the effect of lysine and pH, dialyzed nanoparticle sols were also titrated back to pH~9 by 0.2 M NaOH. The resulting zeta potential in the case of both particle sizes is more highly negative than that of particles in the as-made solution. This is consistent with the expected adsorption of cationic lysine in the as-made samples at this pH on the silica particle surface[17], leading to at least partial neutralization of negatively charged silanol groups, a phenomena that does not occur when the dialyzed solution (i.e., lysine-free) is titrated with NaOH.

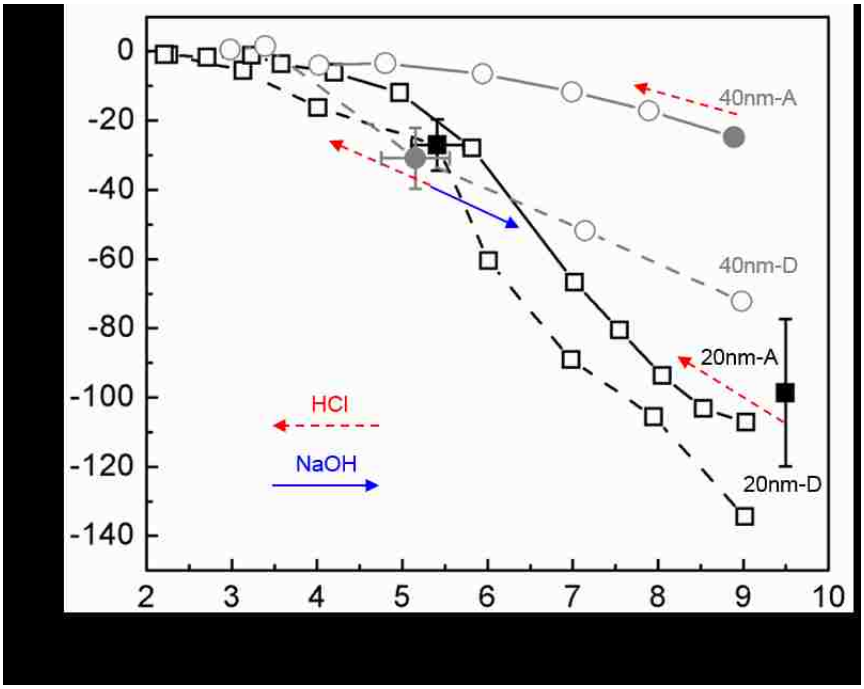

Figure 3-5. Zeta potential as a function of pH for Lys-Sil sols with (denoted as 20nm-D and 40nm-D) and without dialysis (denoted as 20nm-A and 40nm-A) against water Solid symbols indicate the as-made and as-dialyzed silica sols, whereas red dashed and blue solid arrows indicate pH titration by 0.2M HCl and NaOH, respectively. Representative error bars including pH (x-axis) and zeta potential (y-axis) are shown, and were calculated from the standard deviation of data points collected from different batches of silica sols

As in the case of the as-made samples and dialyzed samples following the reloading of lysine, titration of the binary system with NaOH to a comparable pH~9 also results in the recovery of a high degree of ordering of the binary nanoparticle assemblies as shown by the representative TEM images in (**Figure 3-6**). While these data do not preclude the possibility for lysine (or arginine) to contribute a degree of steric stabilization to the system, they underscore the apparent importance of pH-dependent electrostatic repulsive for achieving hard-sphere like character, and thus ordered binary assembly, in the Lys-Sil system.

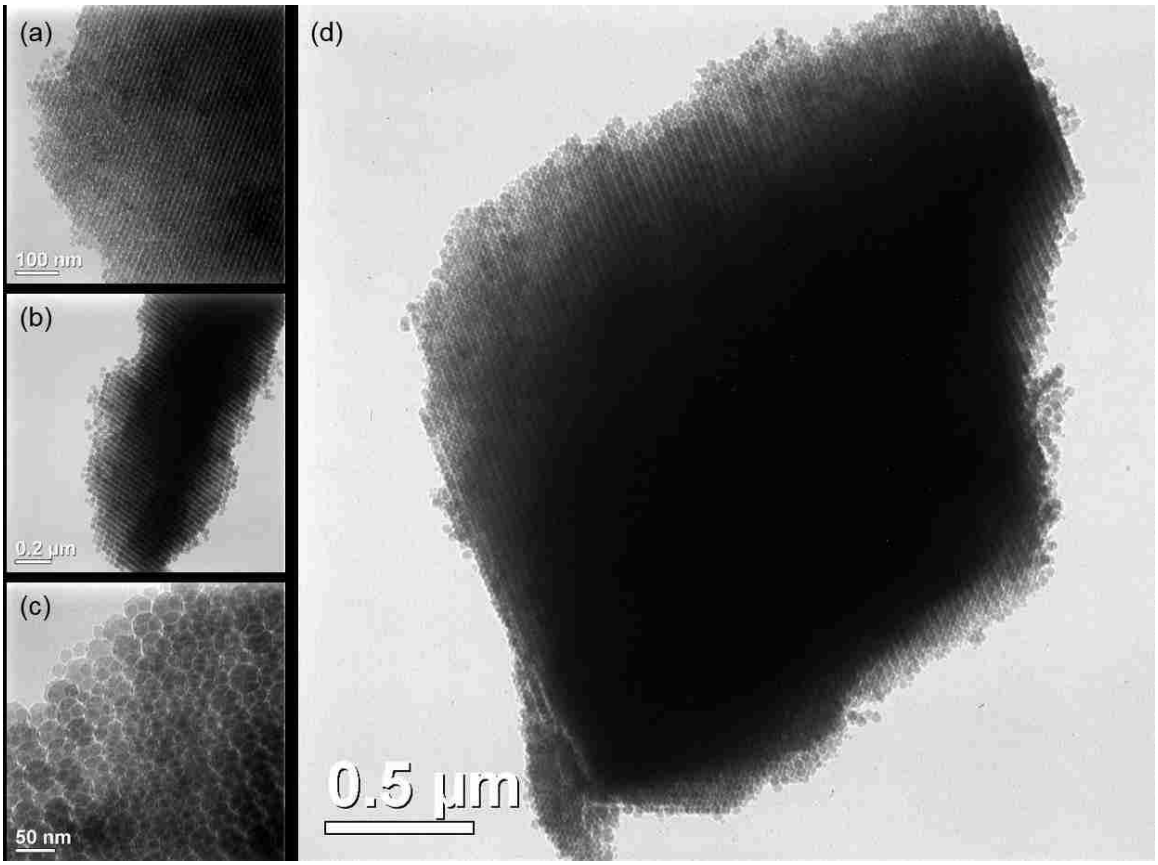

Figure 3-6. TEM images of (a) 20nm, (b) 40nm, (c) and (d) 20/40nm dialyzed silica sols with pH~9 adjusted by 0.2M NaOH

3.3.3 Effects of aging on nanoparticle stability

In addition to the electrostatic stabilization induced and recovered by lysine and NaOH, the long-term stability of dialyzed silica sols was also investigated as a function of aging time following dialysis. In these studies, the dialyzed silica sol was aged statically at room temperature, and analyzed every 7 days over a period of 28 days total. **Figure 3-7** shows representative TEM images of unary 20 nm and 40 nm assemblies as well as binary assemblies of dialyzed silica sols, derived through ambient solvent evaporation at time points throughout the aging period. Unary assembly of 20nm silica nanoparticles in **Figure 3-7**a shows that the degree of ordering was high only in the freshly dialyzed 20nm silica sol, but decreased with increased aging time. Namely, after just 7 days of aging of the sol, the yield of ordered unary 20 nm assemblies reduced to ca. 50%, with elimination of ordering following 14 days of aging. However, a high yield of ordered 40 nm unary assemblies (**Figure 3-7**b) was observed regardless of the aging time. Binary assembly of small and large particles were all disordered as shown in **Figure 3-7**c.

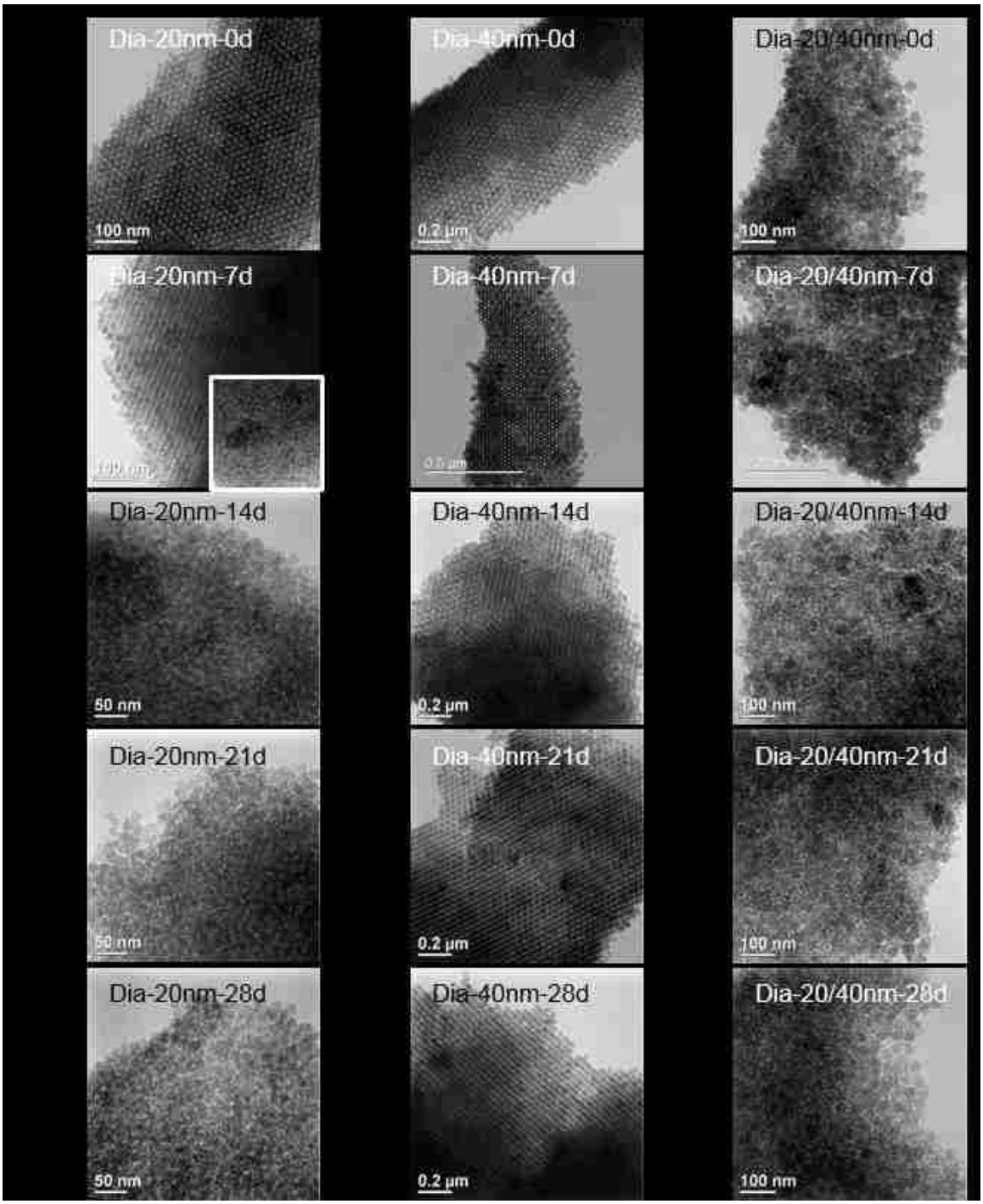

Figure 3-7. TEM images of dried powers from dialyzed silica sols composed of (a) 20nm, (b) 40nm, and (c) 20/40nm primary silica nanoparticles at specified time points during the duration of aging from as made (0d) to 28 day (28d) aging.

In order to further elucidate this apparent effect of aging on particle assembly, zeta potential analysis was carried out as shown in **Figure 3-8**. The zeta potential of 20 and 40 nm silica sols was measured to be weakly negative between -25 and -10 mV over the aging period. Thus, in all cases the particles were poorly stable according to rules of thumb for charge stabilization[6]. This weakly negative zeta potential is consistent with the measured zeta potential of Lys-Sil nanoparticles at the pH of these dialyzed silica sols (i.e., pH~5-5.5) owing to moderate dissociation of silanol groups into charged species.

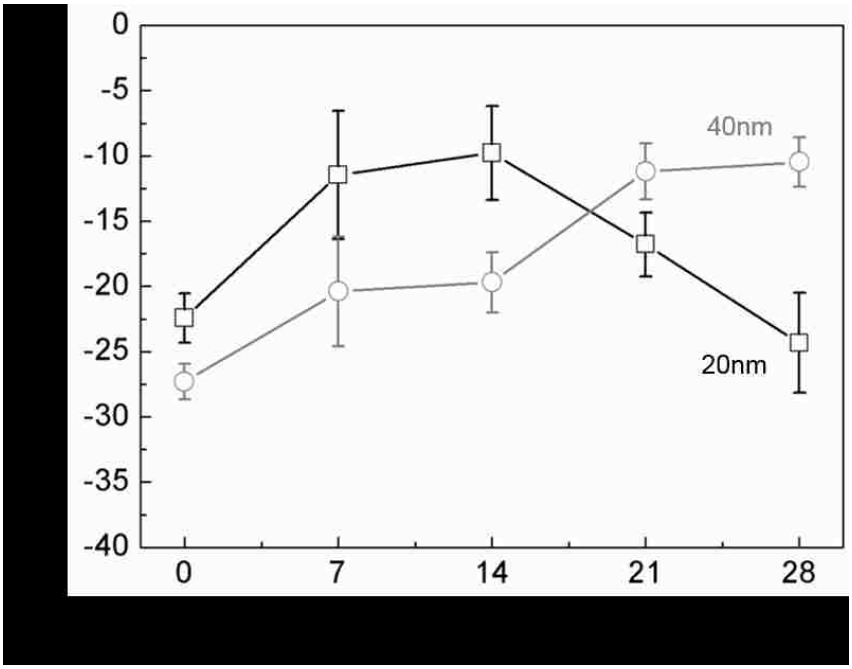

Figure 3-8. Zeta potential of dialyzed 20 and 40 nm silica nanoparticle sols with aging. Error bars indicate the standard deviation per measurement with 10 runs.

While no clear trend is observed in the zeta potential measured specifically for the aged 20 nm particles, complementary ATR-FTIR analysis was carried out in order to gain potential spectroscopic insight into the apparent evolution in colloidal stability. Survey

scans of the 20 nm and 40 nm particles are shown in **Figure 3-9** for as-made, freshly dialyzed (Dia-0d) and aged (Dia-7d to Dia-28d) samples. The very intense and broad band in the region of 3500-3200 cm^{-1} common to all survey profiles (**Figure 3-9**a and c) is due to strong OH stretching vibrations in water and silanol groups of the silica. The band at 1650 cm^{-1} is indicative of physically adsorbed water on silica. Water subtraction, however, was not possible due to the high noise owing to the dilute nature of the Lys-Sil sols.

Bands at wavenumbers between 1200 and 900 cm^{-1} can be assigned to the strong absorbance by the silica network and to C-H and C-O stretching associated with ethanol (3000, and 1100-1000 cm^{-1}) and lysine (1500-1400 cm^{-1}). The absence of the latter bands upon sample dialysis confirms the removal of ethanol and lysine. Magnification of the silica-specific region of the spectra in **Figure 3-9**b and d reveals several noteworthy features. The sharp band at 1120 cm^{-1} results from asymmetric stretching vibrations of siloxane (Si-O-Si) bridging sequences in all samples. The shoulders to the left and right of the siloxane band (i.e., 1115-1300 cm^{-1} and 1075 cm^{-1}) are indicative of bonding in the silica network[24, 25]. Whereas the silica network signature at these wavenumbers remains unchanged upon aging in the case of the 40 nm silica particles, clear evolution of structure is indicated with aging of the 20 nm samples. We attribute this structural evolution upon aging to slow water diffusion through the microporous silica network and association with and disruption of internal siloxane bridges[26] at characteristic penetration depths on the order of ca. 15 nm (i.e., the scale of the particles). While deconvolution of the IR-elucidated structural evolution into specific modes is not possible, it accompanies clear transition in the stability of the 20 nm silica particles with aging that is not indicated by dramatic

changes in the zeta potential, but is manifested in the order to disorder transition in their assembly (**Figure 3-7**).

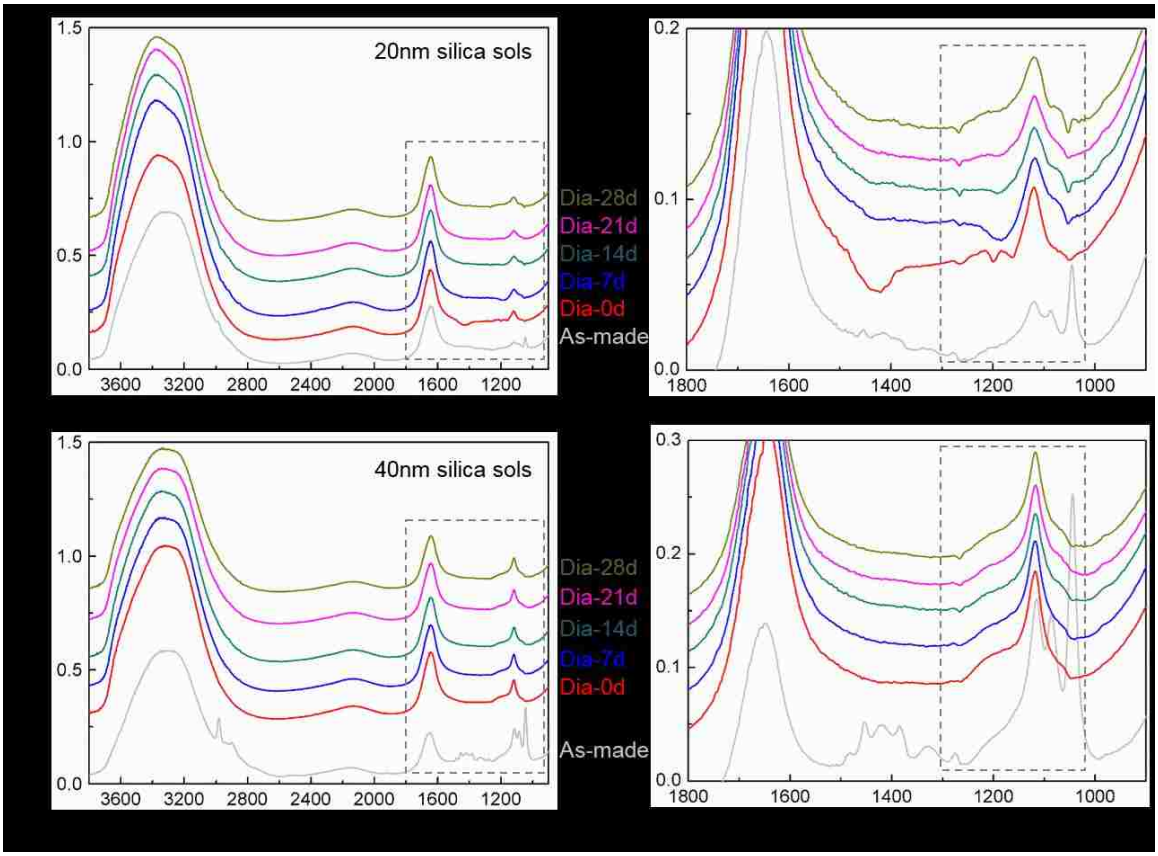

Figure 3-9. ATR-FTIR of (a-b: 20nm and c-d: 40nm) as-made Lys-Sil sol (denoted as As-made) and aged dialyzed silica sols (denoted as Dia-0d to Dia-28d) with peaks at 3500-3200 cm^{-1}: OH stretching, 2981 cm^{-1}: C-H stretching, 1650 cm-1: H_2O bending, 1120 cm^{-1}: Si-O-Si stretching (highlighted in enlarged spectrum by grey dashed lines), 1102 and 1055 cm-1: C-O stretching in ethanol. Panels (b,d) are magnifications of the regions from (a,c) highlighted by a dashed box. The dashed box in panels (b,d) highlight wavenumbers associated with silica network dynamics, with a clear evolution with time in the case of the 20 nm silica particles.

3.3.4 Substrate effect on the ordering of binary assemblies of silica nanoparticles

The evaporation-induced convective assembly of binary Lys-Sil nanoparticles was also found to be influenced by the nature of the substrate upon which the assembly was realized. Representative TEM images in **Figure 3-10** show the result of binary assemblies prepared on various surfaces, including (a) hydrophobic polystyrene (PS) caps, (b) hydrophobic PS films deposited on glass slides, (c) super-hydrophilic glass slides and (d) super-hydrophilic silicon wafers.

Ordered binary structures were only found on PS surfaces, with the highest yield (ca. 90%) obtained when solutions were confined in PS caps/containers during solvent evaporation and medium yield (ca. 50%) when solutions were spread as droplets on PS films. When binary nanoparticle solutions were deposited on piranha-treated (super-hydrophilic) surfaces, binary assemblies upon solvent evaporation were fully disordered. On the contrary, ordered unary assembly of 20 and 40nm silica nanoparticles were found on both PS and glass slide surfaces as shown in **Figure 3-11**.

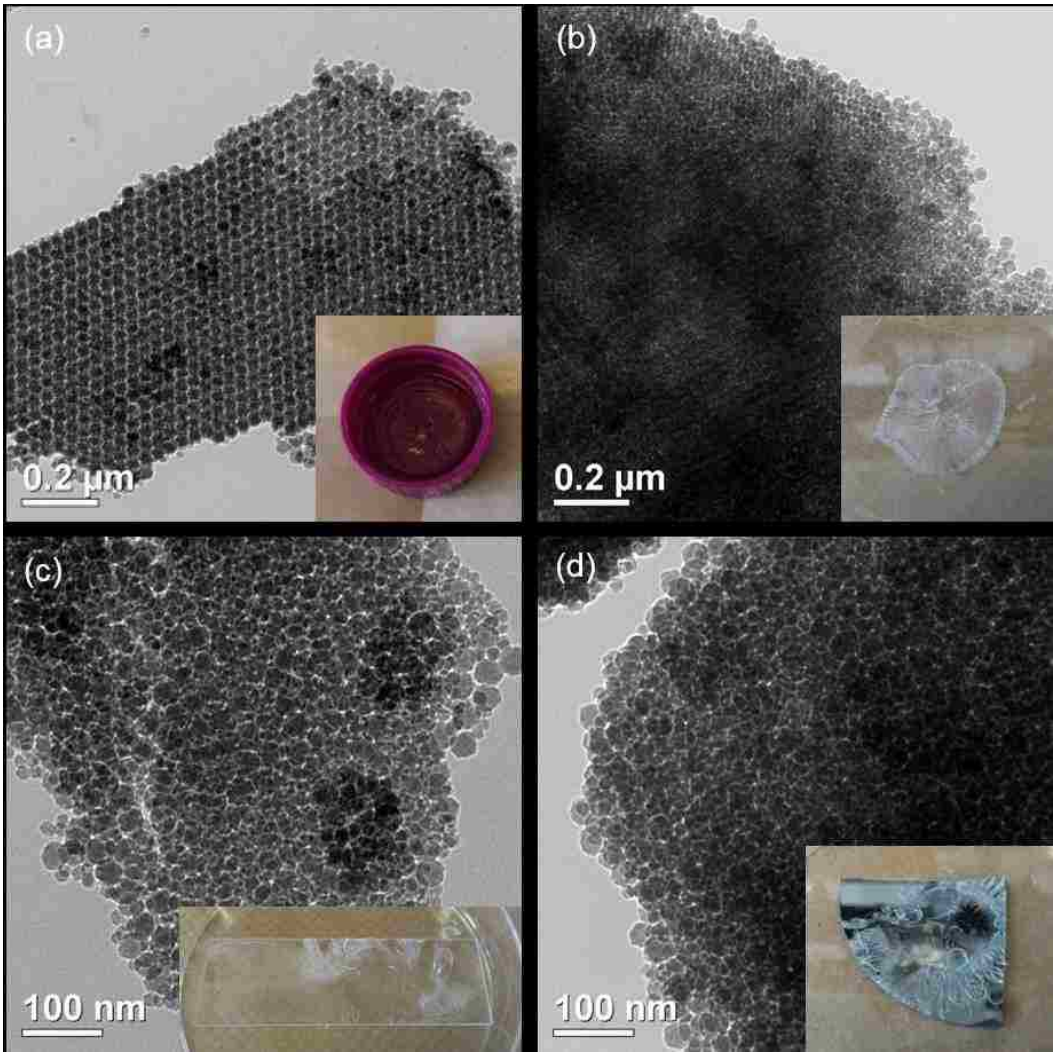

Figure 3-10. TEM images of binary assembly of silica nanoparticles on various surfaces, including (a) PS cap, (b) PS film deposited on glass slide, (c) piranha-treated glass slide and (d) silicon wafer

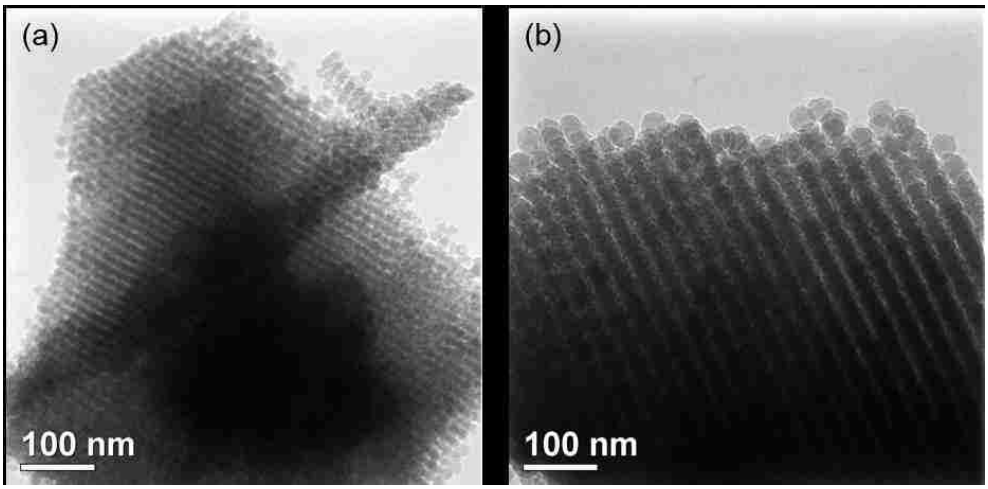

Figure 3-11. Unary assembly of (a) 20nm and (b) 40nm on piranha-treated glass slides

The degree of wetting of the substrates is indicated by contact angle measurements (**Figure 3-12)** carried out with deionized water on the same range of surfaces. The surface energy of piranha-treated silicon wafers is higher than hydrophobic carbon and polystyrene surfaces, so that the water droplet spread out easily on silicon the wafer, resulting in a very small contact angle (<5°). Whereas the realization of highly ordered unary colloidal crystals comprised of 20 nm and 40 nm particles is apparently independent of the changes in surface energy among the substrates (**Figure 3-11**), the confinement imposed by the thin wetting film as well as the area for evaporation (i.e., larger for high wetting, smaller for low wetting and/or cap confinement) may play an important role in controlling the order of binary assemblies given the concomitant need for the small and large constituent particles to arrive at the crystallization front. Specifically, as we have described in Chapter 2 (**Figure 2-13**), the extent of achievable order of the binary assembly appears strongly influenced by the relative rates of nanoparticle convection to the crystallization front (i.e.,

driven by solvent evaporation, and thus influenced by evaporative surface area) and the rate of local rearrangement.

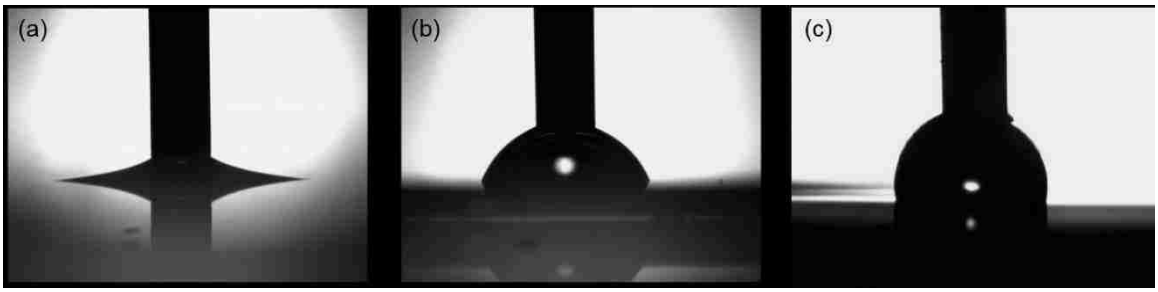

Figure 3-12. Contact angles of water droplet on (a) piranha-treated silicon wafer, (b) carbon film deposited on silicon wafer, and (c) polystyrene surface

3.3.5 Translation of bulk binary assembly to binary thin films

This sensitivity of binary order to the surface upon which the assembly is realized has important practical implications for scale-up of bulk ordered mesoporous materials as well as for the potential translation of the bulk structures to ordered binary nanoparticulate films. We have briefly studied the latter by carrying out convective deposition of binary silica sols using blade coating as reported previously[15, 16]. **Figure 3-13** shows the SEM top-view images of binary silica (20/40 nm) deposited on piranha-treated silicon wafers and silicon wafer-supported carbon films. Disordered binary silica films were observed on both substrates. Attempts to make the same films on silicon wafer-supported PS failed due to serious de-wetting of binary silica sol (aqueous solution with high surface tension) on the low surface energy PS surface. While efforts to translate the binary assemblies to convectively deposited thin films are challenging due to the difficulty in navigating the necessary balance of various interaction forces between particle-particle and particle-

substrate, such as capillary force between particles[27, 28] and particle-substrate interactions[29], and rates of deposition and assembly, collaborative work with Dr. Zheng Tian (Ph.D., Lehigh, 2014)[30] suggests that it can be possible as shown by the large binary order in the convectively deposited films shown in **Figure 3-14**.

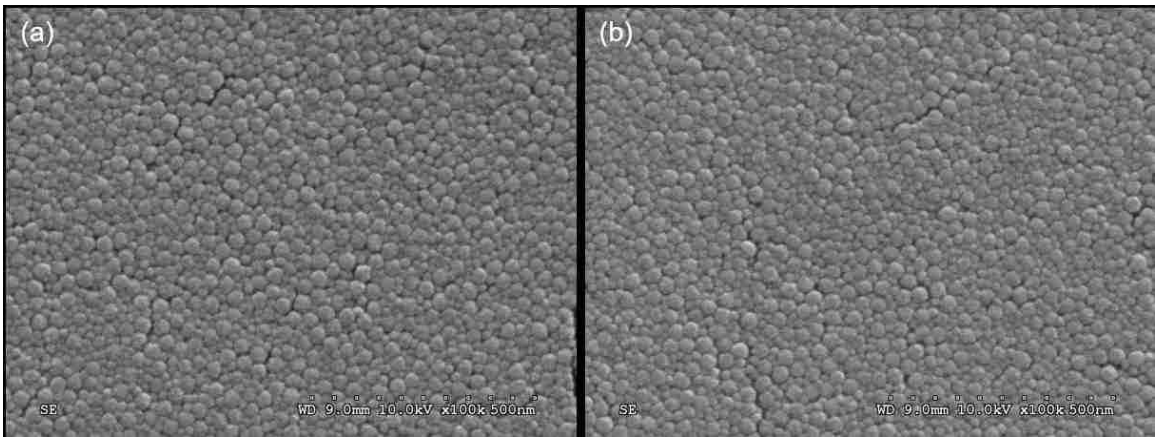

Figure 3-13. SEM top-view images of binary silica (20/40 nm) deposited on (a) piranha-treated silicon wafers and (b) carbon film deposited silicon wafers by blade coating

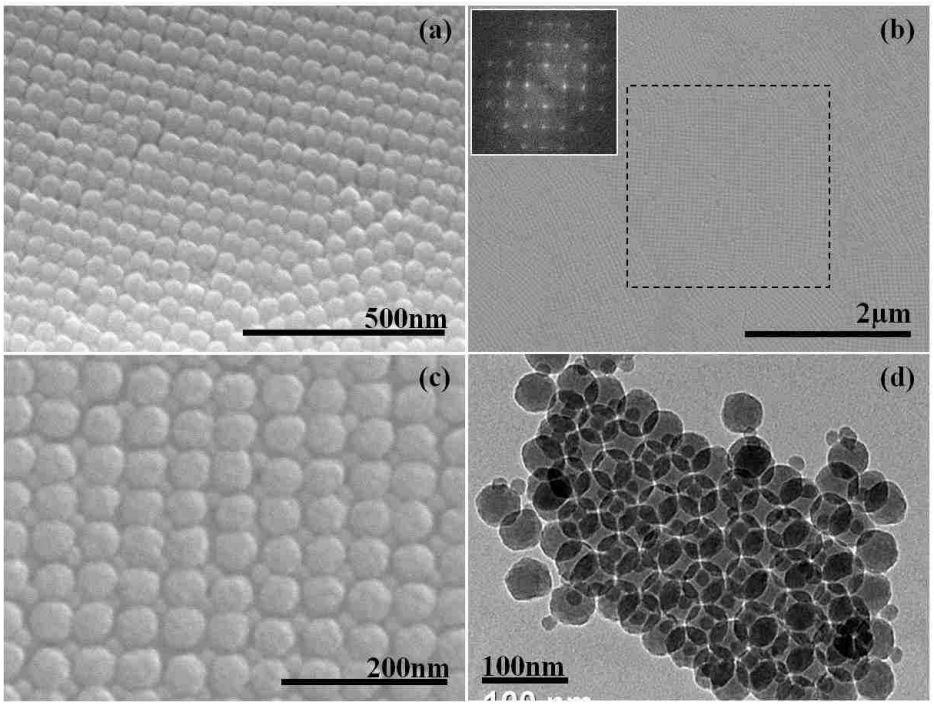

Figure 3-14. [Reproduced from Ref.[30]] Representative SEM and TEM images of top surface of ordered binary silica nanoparticle colloidal crystal film composed of 20/50nm binary particle mixture of AB-type symmetry. (a) High magnification SEM image with transition region from one crystal domain to another; (b) Low magnification SEM image with an inset FFT diffraction to confirm the ordered cubic stoichiometry; (c) High magnification SEM image of cubic packing of large particles with confined pattern of small particles; (d) TEM image of the corresponding a region scratched from the silicon-wafer substrate.

3.4 Conclusion

Beyond particle physics, the effect of composition of Lys-Sil sols and the role of electrostatic repulsive force on assembly of silica nanoparticles have been clarified, revealing that destabilization of the silica particles within the binary mixture by removal of solvated amino acids, a reactant for particle synthesis, via dialysis can lead to destruction of the crystallinity of the binary assembly even if the silica particles remain stable immediately upon dialysis and can assemble on their own into unary nanoparticle crystals. Simple replenishment of lysine (or arginine and NaOH) re-establishes the ordered binary phase behavior, underscoring the role of electrostatic repulsive forces in establishing intrinsic estability sufficient to counterbalance van der Waals forces such that entropic effects, and thus hard sphere phase behavior, dominate the Lys-Sil binary assembly.

In addition, evolution of the stability of dialyzed sols of Lys-Sil derived nanoparticles has been identified. FTIR spectroscopic insight has revealed how apparent evolution of the silica network comprising the smallest particles accompanies the order-to-disorder transition observed in the unary assembly. Despite this evolution in stability, crystalline nanoparticle order can be reestablished simply by titration of the aged sols by lysine, arginine, or NaOH in order to restore electrostatic stability.

Finally, the influence of the substrate upon which the binary assembly is prepared, namely differentiated by surface energy, has been explored. The sensitivity is attributed to concomitant changes in wetting of the nanoparticle sol and the related modulation of evaporation rate and possible particle-substrate interactions. This sensitivity only further underscores the need to balance rates of evaporation, and thus particle convection to the

crystallization front, and rates of local particle rearrangement in order to realize large-scale ordered binary silica structures and related, convectively deposited films.

3.5 Reference

1. Stober, W.; Fink, A.; Bohn, E., Controlled Growth of Monodisperse Silica Spheres in Micron Size Range. *Journal of Colloid and Interface Science* **1968,** 26, (1), 62-&.

2. Davis, T. M.; Snyder, M. A.; Krohn, J. E.; Tsapatsis, M., Nanoparticles in lysine-silica sols. *Chemistry of Materials* **2006,** 18, (25), 5814-5816.

3. Snyder, M. A.; Lee, J. A.; Davis, T. M.; Scriven, L. E.; Tsapatsis, M., Silica nanoparticle crystals and ordered coatings using lys-sil and a novel coating device. *Langmuir* **2007,** 23, (20), 9924-9928.

4. Fan, W.; Snyder, M. A.; Kumar, S.; Lee, P. S.; Yoo, W. C.; McCormick, A. V.; Penn, R. L.; Stein, A.; Tsapatsis, M., Hierarchical nanofabrication of microporous crystals with ordered mesoporosity. *Nature Materials* **2008,** 7, (12), 984-991.

5. Yokoi, T.; Sakamoto, Y.; Terasaki, O.; Kubota, Y.; Okubo, T.; Tatsumi, T., Periodic arrangement of silica nanospheres assisted by amino acids. *Journal of the American Chemical Society* **2006,** 128, (42), 13664-13665.

6. Yokoi, T.; Wakabayashi, J.; Otsuka, Y.; Fan, W.; Iwama, M.; Watanabe, R.; Aramaki, K.; Shimojima, A.; Tatsumi, T.; Okubo, T., Mechanism of Formation of Uniform-Sized Silica Nanospheres Catalyzed by Basic Amino Acids. *Chemistry of Materials* **2009,** 21, (15), 3719-3729.

7. Xia, Y. N.; Gates, B.; Yin, Y. D.; Lu, Y., Monodispersed colloidal spheres: Old materials with new applications. *Adv. Mater.* **2000,** 12, (10), 693-713.

8. Jeong, U.; Wang, Y. L.; Ibisate, M.; Xia, Y. N., Some new developments in the synthesis, functionalization, and utilization of monodisperse colloidal spheres. *Advanced Functional Materials* **2005,** 15, (12), 1907-1921.

9. Li, F.; Josephson, D. P.; Stein, A., Colloidal Assembly: The Road from Particles to Colloidal Molecules and Crystals. *Angewandte Chemie-International Edition* **2011,** 50, (2), 360-388.

10. Min, Y. J.; Akbulut, M.; Kristiansen, K.; Golan, Y.; Israelachvili, J., The role of interparticle and external forces in nanoparticle assembly. *Nature Materials* **2008,** 7, (7), 527-538.

11. Bishop, K. J. M.; Wilmer, C. E.; Soh, S.; Grzybowski, B. A., Nanoscale Forces and Their Uses in Self-Assembly. *Small* **2009,** 5, (14), 1600-1630.

12. Walker, D. A.; Kowalczyk, B.; de la Cruz, M. O.; Grzybowski, B. A., Electrostatics at the nanoscale. *Nanoscale* **2011,** 3, (4), 1316-1344.

13. Doane, T. L.; Chuang, C. H.; Hill, R. J.; Burda, C., Nanoparticle zeta-Potentials. *Accounts Chem Res* **2012,** 45, (3), 317-326.

14. Fan, W.; Snyder, M. A.; Kumar, S.; Lee, P. S.; Yoo, W. C.; McCormick, A. V.; Lee Penn, R.; Stein, A.; Tsapatsis, M., Hierarchical nanofabrication of microporous crystals with ordered mesoporosity. *Nature Materials* **2008,** 7, (12), 984-91.

15. Kumnorkaew, P.; Ee, Y. K.; Tansu, N.; Gilchrist, J. F., Investigation of the Deposition of Microsphere Monolayers for Fabrication of Microlens Arrays. *Langmuir* **2008,** 24, (21), 12150-12157.

16. Tian, Z.; Snyder, M. A., Hard Templating of Symmetric and Asymmetric Carbon Thin Films with Three-Dimensionally Ordered Mesoporosity. *Langmuir* **2014,** 30, (32), 9828-9837.

17. Kitadai, N.; Yokoyama, T.; Nakashima, S., ATR-IR spectroscopic study of L-lysine adsorption on amorphous silica. *Journal of Colloid and Interface Science* **2009,** 329, (1), 31-37.

18. Gao, Q.; Xu, W. J.; Xu, Y.; Wu, D.; Sun, Y. H.; Deng, F.; Shen, W. L., Amino acid adsorption on mesoporous materials: Influence of types of amino acids, modification of mesoporous materials, and solution conditions. *Journal of Physical Chemistry B* **2008,** 112, (7), 2261-2267.

19. Vlasova, N. N.; Golovkova, L. P., The adsorption of amino acids on the surface of highly dispersed silica. *Colloid Journal* **2004,** 66, (6), 657-662.

20. Snyder, M. A.; Demirgoz, D.; Kokkoli, E.; Tsapatsis, M., Benign, 3D encapsulation of sensitive mammalian cells in porous silica gels formed by Lys-Sil nanoparticle assembly. *Microporous and Mesoporous Materials* **2009,** 118, (1-3), 387-395.

21. Watanabe, R.; Yokoi, T.; Kobayashi, E.; Otsuka, Y.; Shimojima, A.; Okubo, T.; Tatsumi, T., Extension of size of monodisperse silica nanospheres and their well-ordered assembly. *Journal of Colloid and Interface Science* **2011,** 360, (1), 1-7.

22. Breitbart, D. J.; Nawar, W. W., Thermal-Decomposition of Lysine. *J Agr Food Chem* **1979,** 27, (3), 511-514.

23. Zhuravlev, L. T., The surface chemistry of amorphous silica. Zhuravlev model. *Colloid Surface A* **2000,** 173, (1-3), 1-38.

24. Innocenzi, P., Infrared spectroscopy of sol-gel derived silica-based films: a spectra-microstructure overview. *J Non-Cryst Solids* **2003,** 316, (2-3), 309-319.

25. Putz, A. M.; Putz, M. V., Spectral Inverse Quantum (Spectral-IQ) Method for Modeling Mesoporous Systems: Application on Silica Films by FTIR. *Int J Mol Sci* **2012,** 13, (12), 15925-15941.

26. Iler, R. K., *The Chemistry of Silica: Solubility, Polymerization, Colloid and Surface Properties and Biochemistry of Silica*. Wiley-Interscience: 1979.

27. Kralchevsky, P. A.; Nagayama, K., Capillary Forces between Colloidal Particles. *Langmuir* **1994,** 10, (1), 23-36.

28. Kralchevsky, P. A.; Denkov, N. D., Capillary forces and structuring in layers of colloid particles. *Curr Opin Colloid In* **2001,** 6, (4), 383-401.

29. Yan, Q.; Gao, L.; Sharma, V.; Chiang, Y. M.; Wong, C. C., Particle and Substrate Charge Effects on Colloidal Self-Assembly in a Sessile Drop. *Langmuir* **2008,** 24, (20), 11518-11522.

30. Tian, Z. Template-mediated, Hierarchical Engineering of Ordered Mesoporous Films and Powders. Ph.D. Thesis, Lehigh University, 2014.

Chapter 4:

Bimodal Three-Dimensionally Ordered Mesoporous Carbons with Tunable Mesopores

4.1 Introduction

Porous carbon materials have attracted extensive research effort because they are the most promising materials for the potential applications in diverse practical fields, such as adsorbents[1-3], energy conversion and storage systems[4-7], catalysts and supports[8-10], electrode materials[11, 12], and other emerging applications. In addition to the unique properties of carbons, such as chemical and mechanical stability, corrosion resistance and electrical conductivity, ordered mesoporous carbons (OMCs) with well-ordered pore topology, high specific surface areas and pore volumes, and tunable pore sizes with narrow pore size distributions hold the potential to provide higher overall performance for applications involving large guest molecules[13-18].

In 1999, ordered mesoporous carbons (OMCs) were synthesized for the first time by using surfactant-templated ordered mesoporous silicas (OMSs) as hard sacrificial templates[19]. Thereafter, this hard-templating methods, also known as nanocasting and requiring a multi-step template formation/replication approach, was widely used to synthesize OMCs with well-defined pore topology and narrow pore size distribution[14, 20-

[23]. First, the inorganic porous silicas were synthesized as hard sacrificial templates, followed by infiltration of carbon precursor into the void space of the silica templates, polymerization and carbonization of carbon precursor, and subsequent removal of silica templates. In the case of hard-templating of mesoporous carbons on OMSs, the carbon replica pores are templated by the OMS walls; however, the size range over which the wall thickness of OMSs can be tuned is quite limited, resulting in limited pore size control of OMCs of usually less than 5 nm[24, 25]. Larger mesopores are, however, desired for a range of applications where diffusion limits are more severe.

More recently, the soft-templating methods originating from surfactant-templated OMS synthesis were extended as another approach to design and synthesize OMCs. These approaches involve evaporation-induced co-assembly of amphiphilic surfactants and phenolic resins as the soft templates and carbon precursors, respectively[26-28]. The approach offers the simplicity to synthesize OMCs and flexibility to control and even enlarge the pore sizes. However, these approaches are hampered by the thermal instability of the polymer framework during pyrolysis, resulting in high pore shrinkage or collapse. Moreover, the ability to enlarge the pore size to larger than 15 nm remains challenging[4]. In addition, the well-ordered pore interconnectivity between mesopores in OMCs plays another important role as a "highway" for large guest molecules to transporting faster from one pore to another[29, 30].

In order to address these challenges, the methods to incorporate secondary mesoporosity in porous carbons were extensively studied, including by dual templates[31-34], soft-templates[35], agglomerate of silica templates[36, 37], and partial filling of carbon precursors[38-41]. However, realization of the bimodal 3D-ordered mesoporous carbons

combined with a broad range of pore size control and pore tunability remains a challenge with the current state-of-the-art.

Recently, template-free ordered mesoporous silicas (OMSs) by bottom-up evaporation-induced convective assembly of binary silica nanoparticles was reported by our group[42]. As detailed in Chapters 2-3 of this thesis, the phase behavior of binary colloidal crystals was governed by the particle size ratio, γ, which enables the fine tuning of primary particle sizes (ca. 10-50 nm) with the fixed particle packing symmetry along the stable size ratio range (AB, AB_2, and AB_{13}). In this work, by using these template-free OMSs as hard sacrificial templates, we demonstrate a facile method to synthesize bimodal three-dimensionally ordered mesoporous (b-3DOm) carbons with tunable large bimodal mesoporosity and 3D-interconnected mesopores.

4.2 Experimental

4.2.1 Preparation of silica templates

The synthesis of silica nanoparticles (Lys-Sil nanoparticles) solutions of different particle sizes and evaporation-induced convective assembly of binary Lys-Sil nanoparticles were reported previously[42-45]. In brief, the Lys-Sil nanoparticles were synthesized by hydrolysis and condensation of tetraethylorthosilicate (TEOS, 98%, Sigma-Aldrich) in aqueous lysine (Sigma Aldrich, 98%). Silica nanoparticles of nominal diameters of ca. 20 nm or less were synthesized by addition of prescribed amounts of TEOS to an aqueous solution of L-lysine that was heated to 90^{o}C. Hydrolysis was carried out under vigorous stirring for 24 hrs. Larger Lys-Sil particles were synthesized by seeded growth of the ca. 20 nm particles. Template-free ordered mesoporous silicas as hard

templates were prepared by mixing appropriate volumes (V_A, V_B) of each of two sols containing large (D_A) and small particles (D_B), respectively. The number density (ϕ_i) of particles in each Lys-Sil sol was measured by drying and weighing the as-made sols, assuming a silica density of 1.8 cm^3/g. Particles of specific sizes were synthesized and associated volume fractions adjusted in order to achieve a desired small-to-large stoichiometry, $N = (V_B\phi_B D_A^3)/(V_A\phi_A D_B^3)$, and a specific particle size ratio, $\gamma = D_B / D_A$, respectively. Once formed, the mixtures were sonicated for 15 minutes followed by evaporation at ambient temperature and pressure, and calcination at 550 ℃ for 12 hours.

4.2.2 Hard-templating of bimodal 3DOm carbons

Furfuryl alcohol (FA, Acros Organics, 98%) and oxalic acid (OA, Acros Organics, 98%) were used as carbon precursor and catalyst, respectively. Carbon precursor solution (molar ratio of FA/OA=100), was infiltrated into dried and calcined silica templates by the incipient-wetness method. The volume of carbon precursor solution was calculated based on the pore volume (cm^3/g) of silica templates. The infiltrated silica-monomer composites were polymerized at 90 ℃ for 20 hours, and the resulting silica-polymer composites were carbonized in a tube furnace at 900 ℃ with 5 ℃/min heating ramp for 3 hours under flowing nitrogen (1.5 L/min flow rate). Silica templates were selectively etched from the silica-carbon composites by potassium hydroxide (KOH, Alfa Aesar, 85%) aqueous solution at room temperature for 3 days under vigorous stirring, followed by centrifugation-redispersion cycles in water until the measured pH reached that consistent with DI water. Wet powder samples were dried at 70 ℃ overnight.

4.2.3 Characterization

Scanning electron microscope (SEM) and transmission electron microscope (TEM) images were collected on a Hitachi S-4300 and a JEOL 2000FX, respectively, to study the morphology and microstructure of the samples. 2D small angle x-ray scattering data (2D-SAXS, Rigaku S-Max3000) were collected for insight into sample mesostructures. Thermal analysis was conducted on a simultaneous thermogravimetric analysis-differential scanning calorimeters (TGA-DSC, TA Instruments SDT Q600). Nitrogen physisorption analysis was carried out on a Micromeritics ASAP-2020 analyzer at 77 K to assess textural properties of the samples. All samples were degassed at 350 $^{\circ}$C for 12 hours prior to analysis. The Brunauer-Emmett-Teller (BET) method was applied to estimate the total specific surface area. The total pore volume (V_t) was estimated from the adsorbed amount at a relative pressure P/P_0~0.995. Barrett-Joyner-Halenda (BJH) analysis was applied for estimation of the pore size distribution within the carbon replicas.

4.3 Results and Discussion

4.3.1 Hard-templating of bimodal 3DOm carbons

Template-free ordered mesoporous silicas (Chapters 2-3) with controllable pore topology and porosity, prepared by bottom-up convective assembly of binary silica nanoparticles, were used as hard sacrificial templates to synthesize b-3DOm carbons with 3D-interconnected large and tunable mesoporosity. The ability to synthesize size-tunable silica nanoparticles, and to assemble them into 3D ordered binary silicas with tunable particle sizes and crystalline phases obeying binary hard-sphere phase behaviors enables the independent mesopore size control of b-3DOm carbons composed of large pores (ca.

32-50nm), and small pores (ca. 15-24nm). Specifically, silica templates composed of binary closed-packed silica nanoparticles can be rationally designed with independently well-controlled particle sizes and binary colloidal crystal phases. To replicate these binary structures into b-3DOm carbons, furfuryl alcohol, used as the carbon precursor, was infiltrated into silica templates, followed by polymerization and carbonization. Carbons derived from polymer furfuryl alcohol are microporous materials with narrow pore size distribution centered on 0.4 to 0.5 nm depending on the synthesis conditions[46-48]. To create 3D-ordered bimodal mesoporosity in microporous carbons, the silica templates were completely etched by KOH aqueous solution.TGA-DSC analysis of the representative AB_2-type 20/40 nm carbons after etching of the silica is shown in **Figure 4-1**, with the complete weight loss indicative of the full removal of the binary silica template during the etching process. This indicates both sufficient etching of the silica as well as the 3D interconnectivity of binary pore bodies in lieu of carbon-isolated silica template particles.

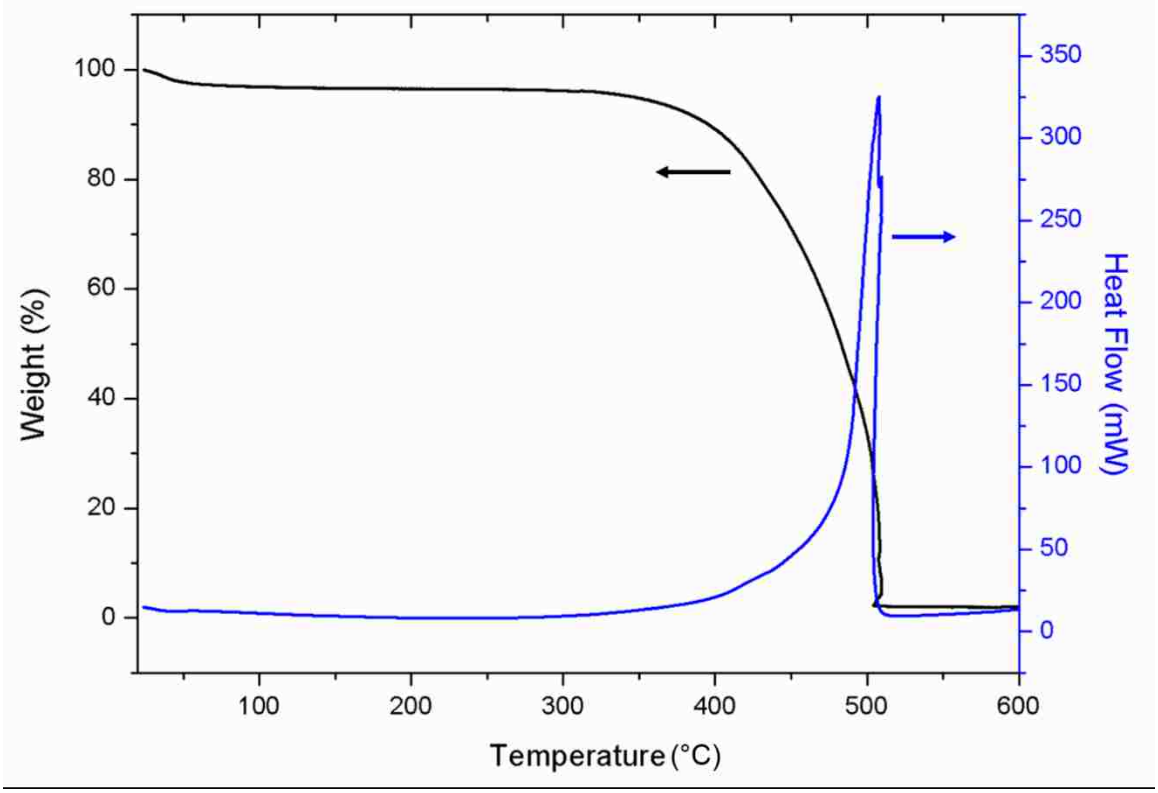

Figure 4-1. TGA-DSC analysis of AB_2-type 20/40nm b-3DOm carbon

In this work, the broad range of pore size control of b-3DOm carbons with small and large pores spanning from 15-23 nm and 40-50 nm, respectively, was demonstrated. Representative TEM images of the hard binary silica templates and the resulting bimodal carbons are shown in **Figure 4-2**. The images revealed that b-3DOm carbons with well-ordered mesostructures with independently tunable pore sizes, and no silica templates were observed in all cases under comprehensive TEM survey. **Figure 4-2**ac show the binary silica templates composed of 20/40 nm and 20/50 nm silica nanoparticles with AB_2-type crystal phase isostructural with AlB_2, and **Figure 4-2**e reveals the AB-type binary silica assembly composed of 15/40 nm silica nanoparticle isostructural with NaCl. The corresponding templated b-3DOm carbons were shown in **Figure 4-2**bde.

In principle, the small and large pore sizes should be tunable by independently changing the silica particle sizes of the hard templates. To study this, we have synthesized binary silica nanoaparticle assemblies as templates, and have systematically varied the constituent particle sizes while maintaining the solid stoichiometry among AB and AB_2. Comparison of **Figure 4-2**b and d demonstrate that the small pore size (20nm) of b-3DOm carbons, with the same pore topology (AB_2-type), can be fixed while changing the large pore size (40 and 50 nm). On the other hand, a comparison of **Figure 4-2**b and f underscores that the large pore size (40 nm) can be fixed while controlling the small pore sizes (15 and 20 nm) and, thereby, specific pore topology (AB and AB_2). These representative images demonstrate that the bimodal pores of b-3DOm carbons appear to be high-fidelity replicas of the binary silica templates. Ultimately, the pore topology and pore size of the resulting carbon are controlled precisely by the silica templates.

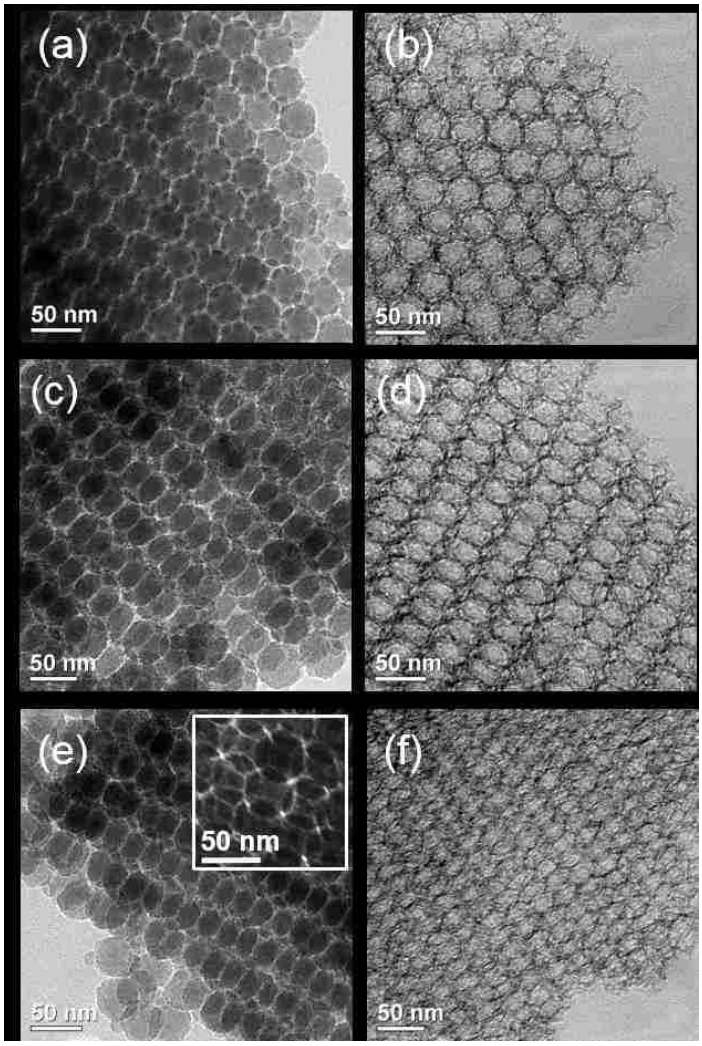

Figure 4-2. TEM images of binary silica templates (a) 20/40nm, (c) 20/50nm, (e) 15/40nm, and templated bimodal 3DOm carbons (b) 20/40nm, (d) 20/50nm, (f) 15/40nm

4.3.2 Bimodal 3DOm carbons with independently tunable pore sizes

The extent of bimodal mesoporous structures was studied by SEM and TEM at lower magnifications (**Figure 4-3**). The SEM images reveal the well-ordered bimodal mesostructures of 20/40 and 20/50 nm carbons, and TEM images with the corresponding fast-Fourier transform (FFT) show the long-range ordering of b-3DOm carbons. Besides the comprehensive TEM survey, the long-range ordered bimodal mesoporous structure of bulk carbon replicas were further confirmed by 2D-SAXS. **Figure 4-4** shows the 2D-SAXS of the binary silica templates and resulting b-3DOm carbons, where the dashed and solid lines represent the binary silica templates and b-3DOm carbons, respectively. 2D-SAXS reveals the 3D periodicity of the silica template as well as the porous carbon replica. The identical well-resolved peaks between corresponding silicate templates and replica materials underscore again how the templated b-3DOm carbons preserve the structural symmetry from the binary silica templates.

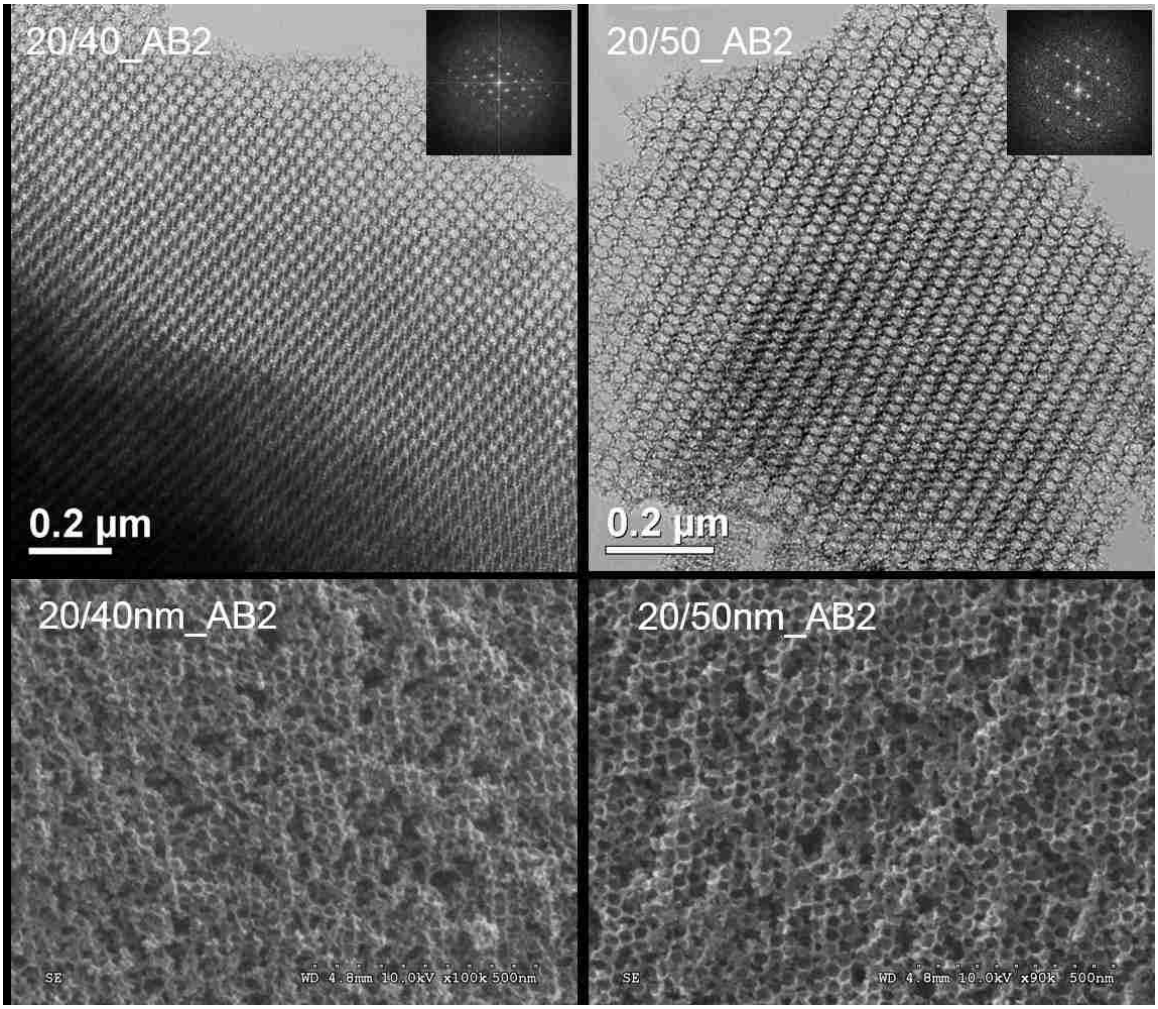

Figure 4-3. TEM and SEM images of AB_2-type 20/40 nm and 20/50 nm b-3DOm carbons

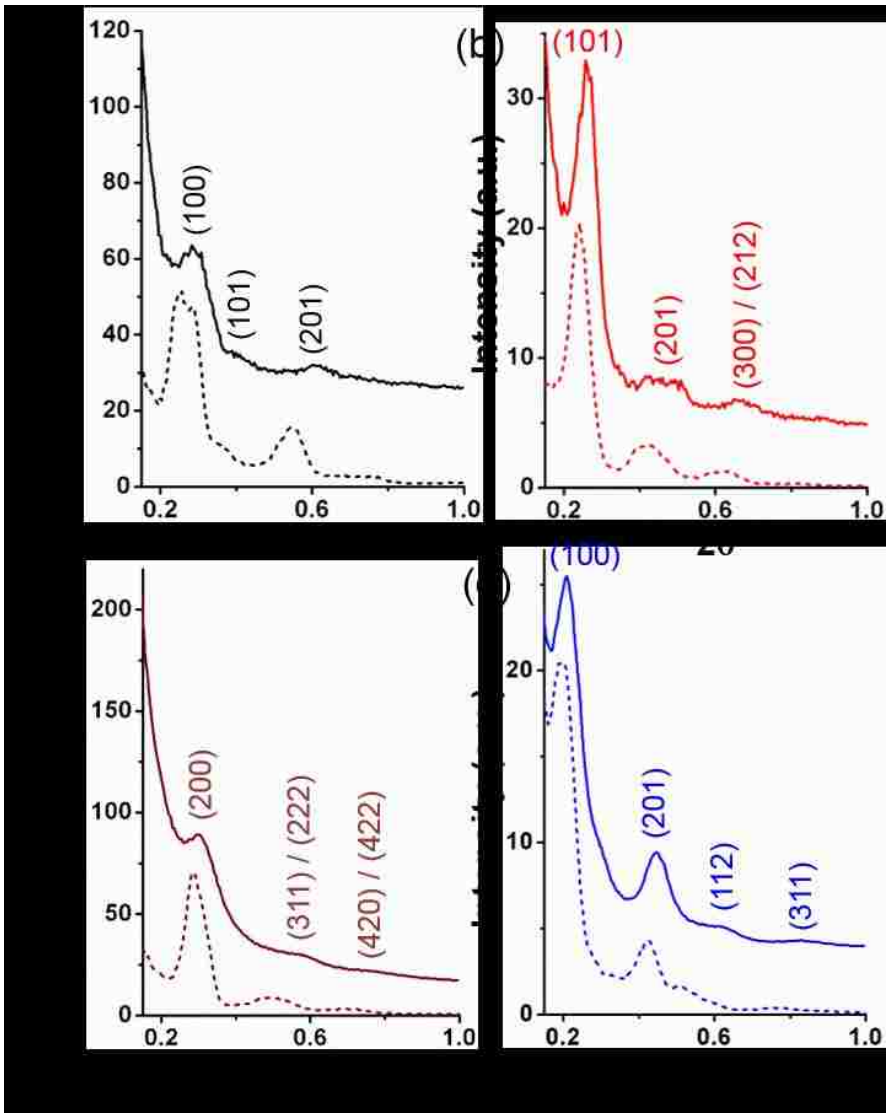

Figure 4-4. 2D-SAXS of silica templates (dash line) and 3DOm carbons (solid line) with (a) 20/40nm, (b) 20/50nm, (c) 15/40nm, and (d) 23/50nm bimodal pores

Independent tunability of mesoporosity and pore topology of these materials was confirmed by the nitrogen physisorption isotherms collected on representative bimodal 3DOm carbons (**Figure 4-5**a). Characteristic hysteresis loops indicate the mesoporosity in all samples. Specifically, two pore condensation steps are clearly observed in all cases studied. Corresponding BJH pore size distributions are shown for the fixed large pore size (50nm) with changing small pore sizes (20 to 23 nm) in **Figure 4-5**b, and a series of AB_2-type pore topology with fixed small pore (20 nm) with tunable large pores (40, 44, 50 nm) in **Figure 4-5**c.

First, the small pore (20nm) was fixed while changing large pores (40, 44, and 50nm) of the AB_2-type pore topology. Second, the large pores were fixed while changing small pores of the same (AB_2-type: 20/50 nm, 23/50 nm) and different pore topologies (AB-type: 15/40 nm; AB_2-type: 20/40 nm). Pore size distributions provide insight into the tunability of the pore sizes of b-3DOm carbons with AB-type (15/40 nm) and AB_2-type (20/40 nm, 20/44 nm, 20/50 nm, 23/50 nm) topology.

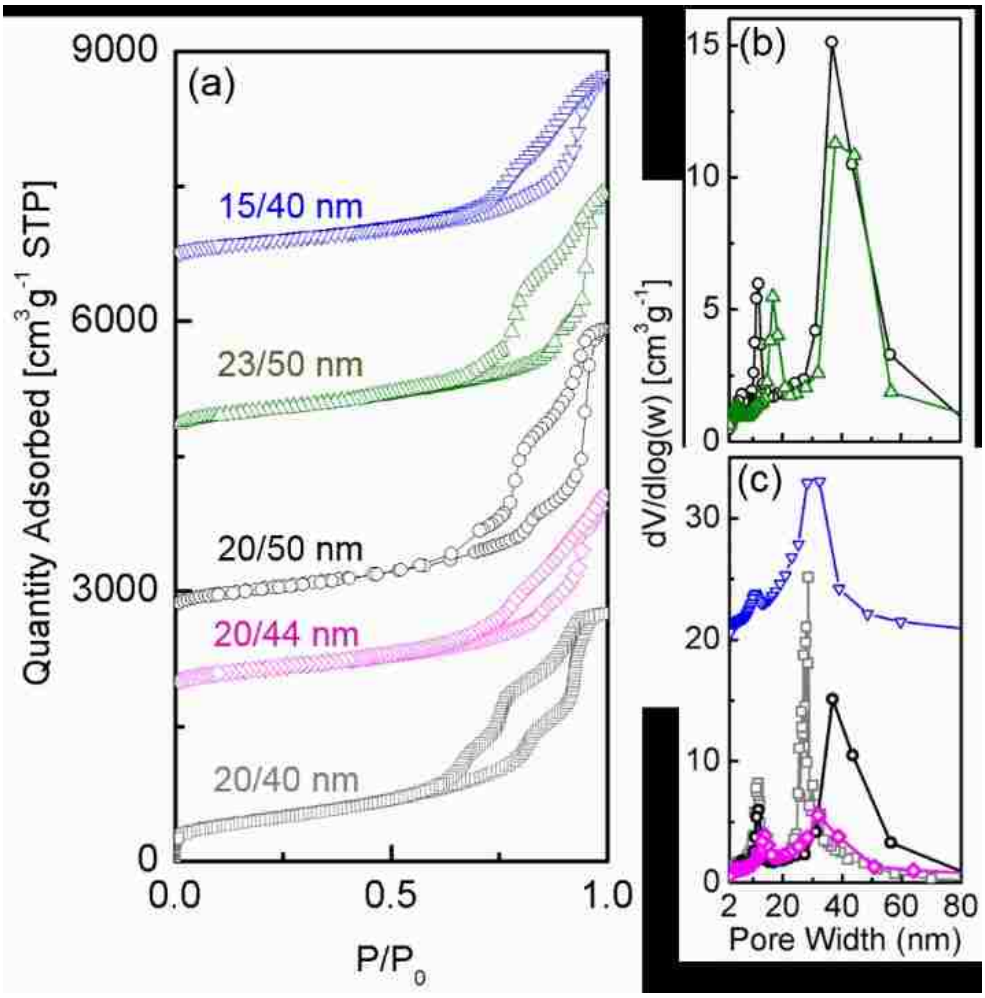

Figure 4-5. (a) Isotherms and (b-c) pore size distribution of b-3DOm carbons templated on binary silica nanoparticle crystals. Data is shown for two solid stoichiometries, (c) AB_2 (20/50 nm, 20/44 nm, 20/40 nm) and AB (15/40 nm), and (b) AB2 (23/50nm; 20/50nm) with specified large and small constituent particle sizes of the binary templates. The pore size distribution for the nominal 20/50 nm samples (black open circles) is shown for reference and comparison purposes in both panels (b) and (c).

4.3.3 Textural properties of bimodal 3DOm carbons

Pore interconnectivity was indicated first by complete removal of silica templates by KOH etching. The sizes of pore windows connecting adjacent spherical pore bodies are conventionally derived from analysis of the desorption branch. **Figure 4-6** reveals the pore size distributions calculated from adsorption and desorption branches by BJH model. Pore sizes were approximately 13 and 27 nm according to adsorption BJH analysis, and the bimodal window sizes of approximately 6 and 9 nm based on desorption BJH analysis, attributed to windows connecting small and large pore bodies, respectively.

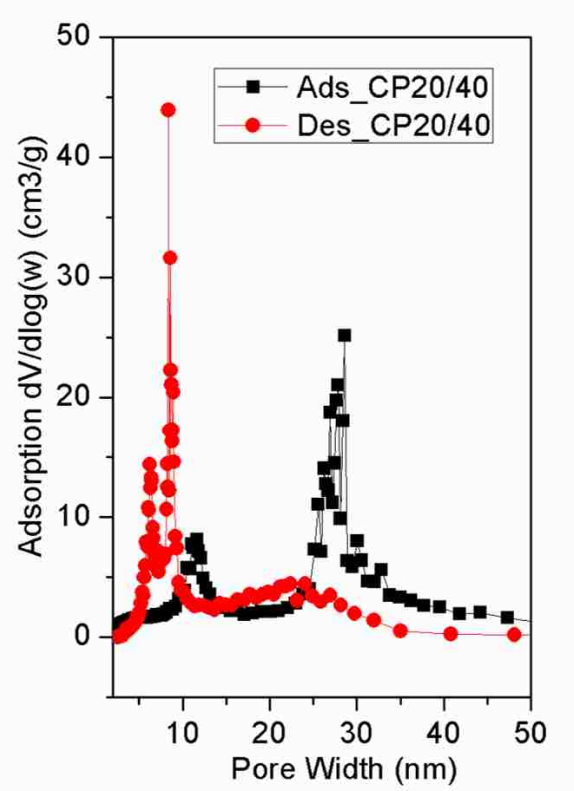

Figure 4-6. Pore size distribution of AB_2-type 20/40nm bimodal carbons derived from adsorption and desorption branches by BJH method

Textural properties are tabulated in **Table 4-1**. In all cases, the BET surface areas of b-3DOm carbons are larger than 1000 (m^2/g), and total pore volumes are between 2 and 5 (cm^3/g), which can be tuned by a KOH etching process at different etching temperatures. Specifically, by etching at higher temperature (180 ℃) KOH-activation of the carbon results in higher surface areas and total pore volumes. In addition, it reveals the apparent structural stability of the b-3DOm carbons even under hydrothermal conditions and in the presence of carbon loss during activation.

Figure 4-7 shows the cumulative pore volume calculated from the BJH adsorption-branch of representative 20/50nm b-3DOm carbons etched at different temperatures. Steeply increasing pore volume is observed in the large-mesopore regime between 10 to 50 nm indicating that the major pore volumes of b-3DOm carbons result from large mesopores. In addition, silica template etched at 180 ℃ results in higher pore volumes, probably due to the activation of carbon walls and enlargement of carbon porous structure.

Table 4-1. Textural properties of bimodal 3DOm carbons

Pore sizes	BET surface area (m^2/g)	Total pore volume (cm^3/g)
15/40nm	1182	3.36
20/50nm	1137 (1474)*	3.60 (5.10)*
20/40nm	1027 (1643)*	2.37 (4.26)*
20/44nm	1239	3.52
23/50nm	1375	4.34

Template silica nanoparticles etched nominally by 6M KOH solution at ambient temperature. Comparative textural properties for samples etched instead at180 ℃ (data shown in brackets) are denoted with *.

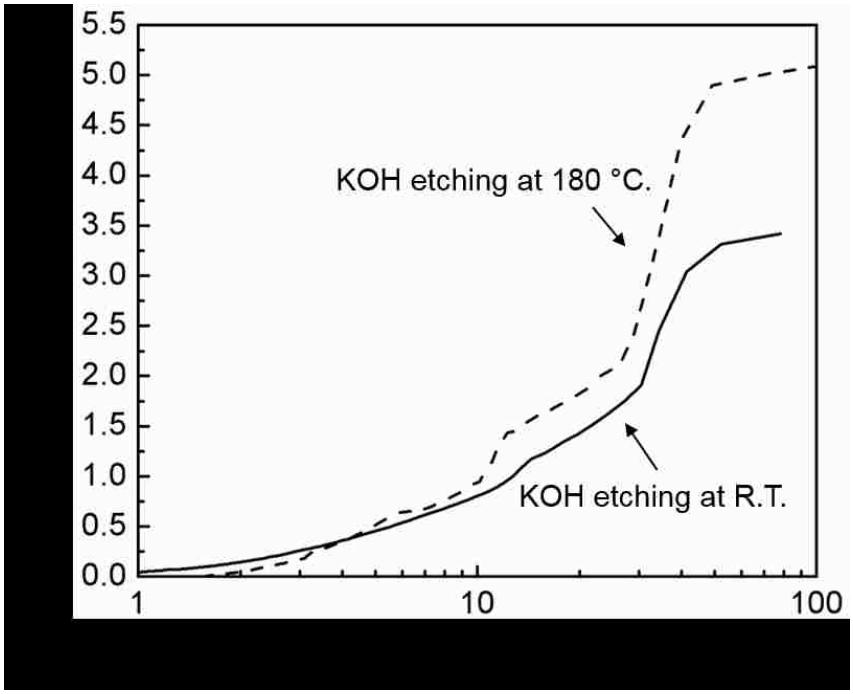

Figure 4-7. Cumulative pore volumes of the representative b-3DOm carbon (20/50nm) derived from adsorption branch by BJH method (solid and dashed lines indicate silica templates were etched by KOH at room temperature and 180 ℃, respectively)

4.4 Conclusions

Bimodal three-dimensionally ordered mesoporous carbons (OMCs) templated by hard sacrificial template-free ordered mesoporous silicas are demonstrated with the following characteristics: 1) high specific surface areas (>1000 m^2/g) and pore volumes (2-5 cm^3/g); 2) 3D-ordered large bimodal mesopores (15 to 50 nm); 3) continuous and independent pore size control with narrow pore size distribution, and 4) 3D-interconnected mesopores with bimodal window sizes. This new class of tunable bi- and tri-modal (i.e., the latter in the case of micropore activation) carbons holds promise for applications spanning batteries, electrodes, catalysts, and adsorbents where diffusion control and potential 3D localization of active sites (e.g., in one size cavity in the b-3DOm materials) could prove useful. In addition, the carbon replication process should be generalizable to

other materials including, for example, metal organic frameworks (MOFs) and metal oxides (TiO_2, ZrO_2).[49]

4.5 Reference

1. Zhuang, X.; Wan, Y.; Feng, C. M.; Shen, Y.; Zhao, D. Y., Highly Efficient Adsorption of Bulky Dye Molecules in Wastewater on Ordered Mesoporous Carbons. *Chemistry of Materials* **2009,** 21, (4), 706-716.

2. Vinu, A.; Miyahara, M.; Sivamurugan, V.; Mori, T.; Ariga, K., Large pore cage type mesoporous carbon, carbon nanocage: a superior adsorbent for biomaterials. *J. Mater. Chem.* **2005,** 15, (48), 5122-5127.

3. Wu, Z. X.; Webley, P. A.; Zhao, D. Y., Comprehensive Study of Pore Evolution, Mesostructural Stability, and Simultaneous Surface Functionalization of Ordered Mesoporous Carbon (FDU-15) by Wet Oxidation as a Promising Adsorbent. *Langmuir* **2010,** 26, (12), 10277-10286.

4. Zhai, Y. P.; Dou, Y. Q.; Zhao, D. Y.; Fulvio, P. F.; Mayes, R. T.; Dai, S., Carbon Materials for Chemical Capacitive Energy Storage. *Adv. Mater.* **2011,** 23, (42), 4828-4850.

5. Li, Y.; Fu, Z. Y.; Su, B. L., Hierarchically Structured Porous Materials for Energy Conversion and Storage. *Advanced Functional Materials* **2012,** 22, (22), 4634-4667.

6. Nishihara, H.; Kyotani, T., Templated Nanocarbons for Energy Storage. *Adv. Mater.* **2012,** 24, (33), 4473-4498.

7. Wang, J. C.; Kaskel, S., KOH activation of carbon-based materials for energy storage. *J. Mater. Chem.* **2012,** 22, (45), 23710-23725.

8. Chai, G. S.; Yoon, S. B.; Yu, J. S.; Choi, J. H.; Sung, Y. E., Ordered porous carbons with tunable pore sizes as catalyst supports in direct methanol fuel cell. *Journal of Physical Chemistry B* **2004,** 108, (22), 7074-7079.

9. Shao, Y. Y.; Sui, J. H.; Yin, G. P.; Gao, Y. Z., Nitrogen-doped carbon nanostructures and their composites as catalytic materials for proton exchange membrane fuel cell. *Appl Catal B-Environ* **2008,** 79, (1-2), 89-99.

10. Zhang, S. L.; Chen, L.; Zhou, S. X.; Zhao, D. Y.; Wu, L. M., Facile Synthesis of Hierarchically Ordered Porous Carbon via in Situ Self-Assembly of Colloidal Polymer and Silica Spheres and Its Use as a Catalyst Support. *Chemistry of Materials* **2010,** 22, (11), 3433-3440.

11. Chaudhari, S.; Kwon, S. Y.; Yu, J. S., Ordered multimodal porous carbon with hierarchical nanostructure as high performance electrode material for supercapacitors. *Rsc Advances* **2014,** 4, (73), 38931-38938.

12. Xie, K.; Qin, X. T.; Wang, X. Z.; Wang, Y. N.; Tao, H. S.; Wu, Q.; Yang, L. J.; Hu, Z., Carbon Nanocages as Supercapacitor Electrode Materials. *Adv. Mater.* **2012,** 24, (3), 347-+.

13. Ryoo, R.; Joo, S. H.; Kruk, M.; Jaroniec, M., Ordered mesoporous carbons. *Adv. Mater.* **2001,** 13, (9), 677-681.

14. Lee, J.; Kim, J.; Hyeon, T., Recent progress in the synthesis of porous carbon materials. *Adv. Mater.* **2006,** 18, (16), 2073-2094.

15. Xing, W.; Qiao, S. Z.; Ding, R. G.; Li, F.; Lu, G. Q.; Yan, Z. F.; Cheng, H. M., Superior electric double layer capacitors using ordered mesoporous carbons. *Carbon* **2006,** 44, (2), 216-224.

16. Deng, Y. H.; Yu, T.; Wan, Y.; Shi, Y. F.; Meng, Y.; Gu, D.; Zhang, L. J.; Huang, Y.; Liu, C.; Wu, X. J.; Zhao, D. Y., Ordered mesoporous silicas and carbons with large accessible pores templated from amphiphilic diblock copolymer poly(ethylene oxide)-b-polystyrene. *Journal of the American Chemical Society* **2007,** 129, (6), 1690-1697.

17. Ndamanisha, J. C.; Guo, L. P., Ordered mesoporous carbon for electrochemical sensing: A review. *Analytica Chimica Acta* **2012,** 747, 19-28.

18. Schuster, J.; He, G.; Mandlmeier, B.; Yim, T.; Lee, K. T.; Bein, T.; Nazar, L. F., Spherical Ordered Mesoporous Carbon Nanoparticles with High Porosity for Lithium-Sulfur Batteries. *Angewandte Chemie-International Edition* **2012,** 51, (15), 3591-3595.

19. Ryoo, R.; Joo, S. H.; Jun, S., Synthesis of highly ordered carbon molecular sieves via template-mediated structural transformation. *Journal of Physical Chemistry B* **1999,** 103, (37), 7743-7746.

20. Jun, S.; Joo, S. H.; Ryoo, R.; Kruk, M.; Jaroniec, M.; Liu, Z.; Ohsuna, T.; Terasaki, O., Synthesis of new, nanoporous carbon with hexagonally ordered mesostructure. *Journal of the American Chemical Society* **2000,** 122, (43), 10712-10713.

21. Lee, J.; Yoon, S.; Oh, S. M.; Shin, C. H.; Hyeon, T., Development of a new mesoporous carbon using an HMS aluminosilicate template. *Adv. Mater.* **2000,** 12, (5), 359-+.

22. Lee, J.; Han, S.; Hyeon, T., Synthesis of new nanoporous carbon materials using nanostructured silica materials as templates. *J. Mater. Chem.* **2004,** 14, (4), 478-486.

23. Lu, A. H.; Schuth, F., Nanocasting: A versatile strategy for creating nanostructured porous materials. *Adv. Mater.* **2006,** 18, (14), 1793-1805.

24. Kruk, M.; Jaroniec, M.; Ryoo, R.; Joo, S. H., Characterization of ordered mesoporous carbons synthesized using MCM-48 silicas as templates. *Journal of Physical Chemistry B* **2000,** 104, (33), 7960-7968.

25. Lee, J. S.; Joo, S. H.; Ryoo, R., Synthesis of mesoporous silicas of controlled pore wall thickness and their replication to ordered nanoporous carbons with various pore diameters. *Journal of the American Chemical Society* **2002,** 124, (7), 1156-1157.

26. Liang, C. D.; Li, Z. J.; Dai, S., Mesoporous carbon materials: Synthesis and modification. *Angewandte Chemie-International Edition* **2008,** 47, (20), 3696-3717.

27. Chuenchom, L.; Kraehnert, R.; Smarsly, B. M., Recent progress in soft-templating of porous carbon materials. *Soft Matter* **2012,** 8, (42), 10801-10812.

28. Ma, T. Y.; Liu, L.; Yuan, Z. Y., Direct synthesis of ordered mesoporous carbons. *Chemical Society Reviews* **2013,** 42, (9), 3977-4003.

29. Sun, G. W.; Wang, J. T.; Liu, X. J.; Long, D. H.; Qiao, W. M.; Ling, L. H., Ion Transport Behavior in Triblock Copolymer-Templated Ordered Mesoporous Carbons with Different Pore Symmetries. *J Phys Chem C* **2010,** 114, (43), 18745-18751.

30. Liang, Y. R.; Li, Z. H.; Fu, R. W.; Wu, D. C., Nanoporous carbons with a 3D nanonetwork-interconnected 2D ordered mesoporous structure for rapid mass transport. *J Mater Chem A* **2013,** 1, (11), 3768-3773.

31. Gierszal, K. P.; Jaroniec, M., Novel pitch-based carbons with bimodal distribution of uniform mesopores. *Chemical Communications* **2004**, (22), 2576-2577.

32. Pang, J. B.; Hu, Q. Y.; Wu, Z. W.; Hampsey, J. E.; He, J. B.; Lu, Y. F., Direct synthesis of unimodal and bimodal nanoporous carbon. *Microporous and Mesoporous Materials* **2004,** 74, (1-3), 73-78.

33. Lee, H. I.; Pak, C.; Shin, C. H.; Chang, H.; Seung, D.; Yie, J. E.; Kim, J. M., Rational design of ordered mesoporous carbon with controlled bimodal porosity via dual silica templating route. *Chemical Communications* **2005**, (48), 6035-6037.

34. Kwon, T. H.; Jung, S.; Kim, H. J.; Park, S.; Kim, S. J.; Huh, S., Preparation of Mesoporous Silica and Carbon Materials with Multilength-Scale Pores and Hydrogen Sorption Application. *European Journal of Inorganic Chemistry* **2009**, (19), 2811-2816.

35. Huang, Y.; Cai, H. Q.; Yu, T.; Zhang, F. Q.; Zhang, F.; Meng, Y.; Gu, D.; Wan, Y.; Sun, X. L.; Tu, B.; Zhao, D. Y., Formation of mesoporous carbon with a face-centered-cubic Fd(3)over-barm structure and bimodal architectural pores from the reverse amphiphilic triblock copolymer PPO-PEO-PPO. *Angewandte Chemie-International Edition* **2007,** 46, (7), 1089-1093.

36. Wu, D. C.; Liang, Y. R.; Yang, X. Q.; Li, Z. H.; Zou, C.; Zeng, X. H.; Lv, G. F.; Fu, R. W., Direct fabrication of bimodal mesoporous carbon by nanocasting. *Microporous and Mesoporous Materials* **2008,** 116, (1-3), 91-94.

37. Liang, Y. R.; Liang, F. X.; Li, Z. H.; Wu, D. C.; Yan, F. Y.; Li, S. Y.; Fu, R. W., The role of mass transport pathway in wormholelike mesoporous carbon for supercapacitors. *Phys Chem Chem Phys* **2010,** 12, (36), 10842-10845.

38. Fuertes, A. B.; Nevskaia, D. M., Control of mesoporous structure of carbons synthesised using a mesostructured silica as template. *Microporous and Mesoporous Materials* **2003,** 62, (3), 177-190.

39. Lu, A. H.; Schmidt, W.; Spliethoff, B.; Schuth, F., Synthesis of ordered mesoporous carbon with bimodal pore system and high pore volume. *Adv. Mater.* **2003,** 15, (19), 1602-+.

40. Fuertes, A. B., Low-cost synthetic route to mesoporous carbons with narrow pore size distributions and tunable porosity through silica xerogel templates. *Chemistry of Materials* **2004,** 16, (3), 449-455.

41. Lu, A. H.; Li, W. C.; Schmidt, W.; Schuth, F., Template synthesis of large pore ordered mesoporous carbon. *Microporous and Mesoporous Materials* **2005,** 80, (1-3), 117-128.

42. Kung, S.-C.; Chang, C.-C.; Fan, W.; Snyder, M. A., Template-Free Ordered Mesoporous Silicas by Binary Nanoparticle Assembly. *Langmuir* **2014,** 30, (39), 11802-11811.

43. Davis, T. M.; Snyder, M. A.; Krohn, J. E.; Tsapatsis, M., Nanoparticles in lysine-silica sols. *Chemistry of Materials* **2006,** 18, (25), 5814-5816.

44. Snyder, M. A.; Lee, J. A.; Davis, T. M.; Scriven, L. E.; Tsapatsis, M., Silica nanoparticle crystals and ordered coatings using lys-sil and a novel coating device. *Langmuir* **2007,** 23, (20), 9924-9928.

45. Fan, W.; Snyder, M. A.; Kumar, S.; Lee, P. S.; Yoo, W. C.; McCormick, A. V.; Penn, R. L.; Stein, A.; Tsapatsis, M., Hierarchical nanofabrication of microporous crystals with ordered mesoporosity. *Nature Materials* **2008,** 7, (12), 984-991.

46. Mariwala, R. K.; Foley, H. C., Evolution of ultramicroporous adsorptive structure in poly(furfuryl alcohol)-derived carbongenic molecular-sieves. *Ind. Eng. Chem. Res.* **1994,** 33, (3), 607-615.

47. Anderson, C. J.; Pas, S. J.; Arora, G.; Kentish, S. E.; Hill, A. J.; Sandler, S. I.; Stevens, G. W., Effect of pyrolysis temperature and operating temperature on the performance of nanoporous carbon membranes. *J. Membr. Sci.* **2008,** 322, (1), 19-27.

48. Peer, M.; Qajar, A.; Rajagopalan, R.; Foley, H. C., Synthesis of carbon with bimodal porosity by simultaneous polymerization of furfuryl alcohol and phloroglucinol. *Microporous and Mesoporous Materials* **2014,** 196, 235-242.

49. Yonemoto, B. T.; Guo, Q. Y.; Hutchings, G. S.; Yoo, W. C.; Snyder, M. A.; Jiao, F., Structural evolution in ordered mesoporous TiO2 anatase electrodes. *Chemical Communications* **2014,** 50, (64), 8997-8999.

Chapter 5:

Scaffolded Growth of Thin Zeolite Films by 3DOm Carbon Films

5.1 Introduction

Microporous crystalline zeolites have attracted extensive research effort owing to the broad range of applications spanning separations, catalysis, and adsorption among others[1, 2]. Structural diversity of zeolites (i.e., more than 200 different pore topologies and primary pore sizes) along with their chemically, thermally and mechanically stable crystalline structure enable the application of zeolite membranes for high-performance membrane-based molecular separations, such as small gases (e.g., CO_2, H_2, CH_4, etc.), and isomeric aromatics and alkanes (e.g., o-/p-xylenes, butanes)[3-6]. Fabrication of high-performance zeolite membranes applied for liquid or gas separations have been studied extensively over the past several decades, since they can serve as environmentally and economically attractive alternatives to current energy-intensive separation processes such as distillation, fractional crystallization, and others[7-10].

In general, zeolite membranes are formed on macroporous supports by an *in situ growth* technique[7, 11], resulting in large film thickness due to a low nucleation site density and undesired penetration of synthesis precursor into the macroporous support, which makes it a non ideal way to fabricate high performance zeolite membranes. The state-of-the-art method on the laboratory scale commonly employs *secondary seeded growth*[1, 2, 12-

[15], which decouples nucleation from crystal growth, including the following three procedures: 1) synthesis of a colloidal dispersion composed of zeolite crystals with desired sizes and shapes, 2) assembly of zeolite crystals deposited on a macroporous support serving as seed layer, and 3) secondary growth of the deposited zeolite crystals to form a continuous film.

For practical membrane applications it is necessary to combine high selectivity with high flux. Flux is typically sacrificed in lieu of forming high selectivity membranes because of the large membrane thickness required to realize continuous membranes by secondary seeded growth and the inverse proportionality of flux to membrane thickness. These large membrane thicknesses are due, in part, to multi-dimensional growth of large seed crystals (i.e., both lateral and vertical growth) until continuous polycrystalline films are realized. Even in these continuous films, non-selective pathways, such as cracks and grain boundaries, arise from the formation and thermal treatment of zeolite membranes[16]. Several approaches to minimize the effects of these defects on membrane selectivity have been reported (e.g. controlling grain orientation, forming nanocomposites with zeolite crystals in the support pores[7, 16-18], repairing by post-synthesis[19-21]). However, these processes tend to be costly and complicated, hampering the reliability and cost-effectiveness of commercial production of zeolite membranes.

Efforts to scale down these membranes in order to realize industrially relevant fluxes have focused recently on the synthesis of preferentially oriented and/or smaller seed crystals for secondary seeded growth. To control the micropore orientation and assembly of seeding zeolite crystals and subsequent secondary zeolite membrane growth, the synthesis and deposition of seed crystals with desirable pore orientation, by either using

the costly customized structure-directing agents (SDAs)[1, 12, 22] or the complex synthesis procedures[23-26], into a dense oriented membranes with the preferable crystal growing directions have been demonstrated. Confined crystal growth as another method led to nanosized zeolite crystals[27-29] and mesoporous zeolite single crystals[28, 30]. At the same time, three-dimensionally ordered mesoporous (3DOm) imprinted zeolite nanocrystals templated by 3DOm porous carbons with controllable mesopore sizes were realized[31]. Furthermore, effort to improve the secondary seeded growth for scaling down the zeolite membrane thickness with minimized membrane defects by exploiting these zeolite nanocrystals or exfoliated zeolite nanosheets as the seed crystals to grow large-scale continuous zeolite membranes has been reported[32-34]. All of these pioneering research results hold exciting implications for fabricating a new, continuous zeolite membrane with better separation performance, but need still exists for facile synthesis procedures with high cost-performance value.

In this chapter, a top-down templating approach of scaffolding the zeolite crystal growth in preformed 3D ordered mesoporous (3DOm) carbon films with controllable film thickness on the order of 10-100 nm stands to address the above challenges. We have reported the systematic study of 3DOm carbon films previously[35, 36]. Here, we exploit this 3DOm carbon film as a scaffold, and infiltrate the zeolite precursor sol into the 3D interconnected pore bodies of the carbon film, followed by steam-assisted crystallization (SAC) hydrothermal reaction to form a zeolite-carbon composite film. We demonstrate how the carbon scaffold can be selectively removed by calcination. Ultimately, the 3DOm-imprinted zeolite film with tunable film thickness is realized, which hold the potential for high-performance separation applications.

5.2 Experimental

5.2.1 Silica nanoparticle synthesis and convective assembly

Silica nanoparticles were synthesized via the hydrolysis of tetraethyl orthosilicate (TEOS, 98%, Acros Organics) in aqueous solution of L-lysine (Sigma-Aldrich) as mentioned previously in Chapter 2. A blade coating system[37] was used for depositing the dialyzed silica nanoparticles on glass slides (76 x 25 x 1 mm, Fisher Scientific) and silicon wafers (Silicon Quest) to form close-packed silica nanoparticle films. All of the substrates were pretreated with piranha solution (4:1 v./v. sulfuric acid/ hydrogen peroxide) for two hours to dissolve the organic impurities. 50μL silica sols were injected into the wedge between the hydrophobic parafilm-coated blade at the edge, and the substrate. The angle between the blade and substrate is 45°, and coating speed was 10 μm/s.

5.2.2 Fabrication of 3DOm carbon templates

Furfuryl alcohol (FA, Acros Organics, 98%) and oxalic acid (OA, Acros Organics, 98%) were used as carbon precursor and catalyst, respectively. Carbon precursor solution (molar ratio of FA/OA=100), was infiltrated into the colloidal silica films as reported previously.[35] The infiltrated silica-monomer composites were polymerized at 90 ℃ for 20 hours, and the resulting silica-polymer composites were carbonized in a tube furnace at 900 ℃ with 5 ℃/min heating ramp for 3 hours under flowing nitrogen (1.5 L/min flow rate). Silica templates were selectively etched from the silica-carbon composites by 4% diluted hydrofluoric acid (HF, Acros Organics, 48%) aqueous solution at room temperature for 2 hours, followed by DI water washing, and dried at ambient temperature.

5.2.3 Confined growth of zeolite crystals within carbon templates

Confined synthesis of uniform silicalite-1 nanocrystals within 3DOm carbon templates (i.e., both bulk powders and 3DOm thin films) was carried out using the steam-assisted crystallization (SAC) method.[38, 39] The overall replication process is schematized in **Figure 5-1** in the context of thin films, but an analogous procedure was used for powder replication. Specifically, in the case of 3DOm carbon powders, a clear solution consisting of tetrapropylammonium hydroxide (40%, Alfa Aesar), sodium hydroxide (NaOH, Merck), deionized water and ethanol was infiltrated into the pores of the 3DOm carbon by incipient-wetness. After slow evaporation of ethanol at room temperature (25℃), TEOS was added to the mixture, and the molar composition of the synthesis gel was 9 TPA_2O/ 0.15 Na_2O/ 50 SiO_2/ 390 H_2O/ 180 ethanol. The impregnated carbon mixture was transferred to an open glass vial, which was placed in a Teflon-lined stainless steel autoclave containing sufficient water to generate saturated steam at 135℃. Before heating, the precursor solution was aged at room temperature for 3h, followed by hydrothermal synthesis, which was carried out in an oven at 135℃ for 6 days. In the case of 3DOm carbon films, template films supported on silicon wafers were dipped in an open glass vial containing the same synthesis gel used for carbon powders. Following the capillary infiltration of reactants after at least 12 hours, the excess reactants were discarded, and the vial was place in a Teflon-lined stainless steel autoclave containing sufficient water to generate saturated steam at 135℃. Thereafter, 3DOm silicalite-1 particulate domains were grown inside the carbon film. Different crystal domain sizes of the silicalite-1 could be realized by tuning the hydrothermal reaction conditions. The carbon template and TPA+ were removed from the product by calcination in air at 570℃ for 7h. In addition, homogeneously nucleated and

grown silicalite-1 crystals without carbon templates were synthesized by mixing the TPAOH clear solution and TEOS with the same composition described above in a Teflon liner, and then repeating the above hydrothermal synthesis procedures.

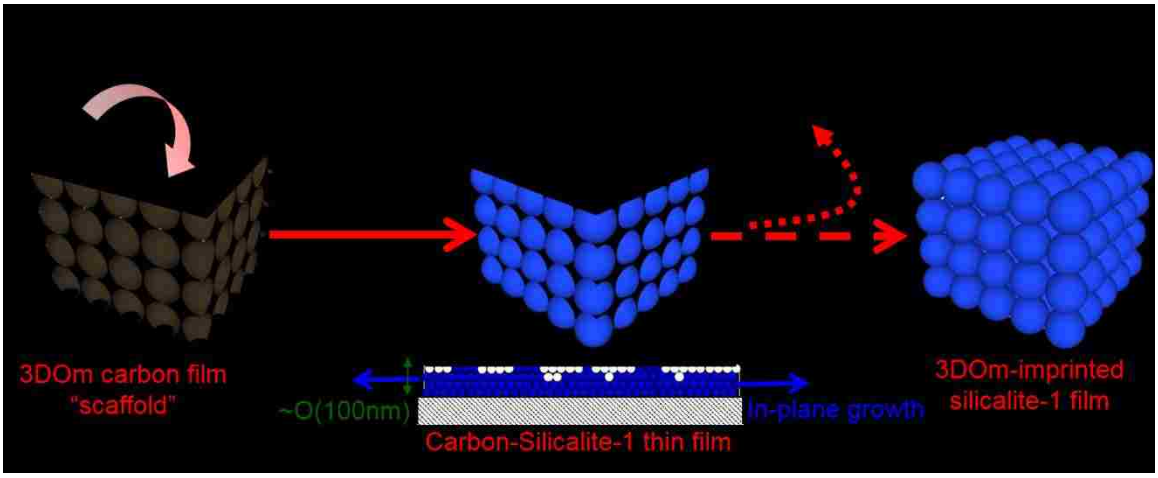

Figure 5-1. Schematic illustration of confined thin zeolite film growth

5.2.4 Characterization

Scanning electron microscope (SEM) and transmission electron microscope (TEM) images were collected on a Hitachi S-4300 and a JEOL 2000FX, respectively, to study the morphology and microstructure of the samples. Powder X-ray diffraction (XRD) was carried out on a benchtop XRD instrument (RIGACU, MINIFLEX 2) equipped with Cu x-ray source (wavelength: 1.54056 Å) with 0.02° step size and 2°/min scanning speed.

5.3 Results and Discussion

5.3.1 Scaffolded growth of zeolites in 3DOm carbon particles

The confined synthesis of silicalite-1 crystals in bulk 3DOm carbon templates was first reproduced to confirm the feasibility of confined crystal growth techniques. As shown in **Figure 5-2**, we can observe (arrows in **Figure 5-2**a) from SEM imaging that the partially grown silicalite-1 crystals were found on the fringe of the bulk crystal domains confined after the removal of the carbon template, and TEM images of the partially grown silicalite-1 crystals shown in **Figure 5-2**b reveal the lattice fringes originating from the crystalline nature of silicalite-1. This partial growth phenomenon is believed to be related to the propagative crystal growth through the carbon cavities, as illustrated in the inset of **Figure 5-2**a. Since nucleation occurs in one carbon cavity, growth of large silicalite-1 crystal domains is hypothesized to occur through propagative crystal growth among other cavities due to the high degree of pore interconnectivity. These partially grown silicalite-1 crystals are expected to result either from halted growth when the hydrothermal synthesis is stopped or by reactant depletion within the scaffold.

Upon carbon removal, 3DOm silicalite-1 nanoparticulate domains were obtained. Homogeneous silicalite-1 crystals without carbon template were also used as a reference. Powder XRD measurements were collected of homogeneously grown silicalite-1 (**Figure 5-2**c, trace A), the carbon-zeolite composite (**Figure 5-2**c, trace B), and silicalite-1 domains isolated from the carbon-zeolite composite (**Figure 5-2**c, trace C). Signature reflections of silicalite-1 (trace A) are observed in the isolated silicalite-1 domains (trace C) after carbon removal. As suggested previously[39], the amorphous nature of the powder

XRD data before carbon removal (**Figure 5-2**c, trace B) may be caused by the presence of the carbon templates.

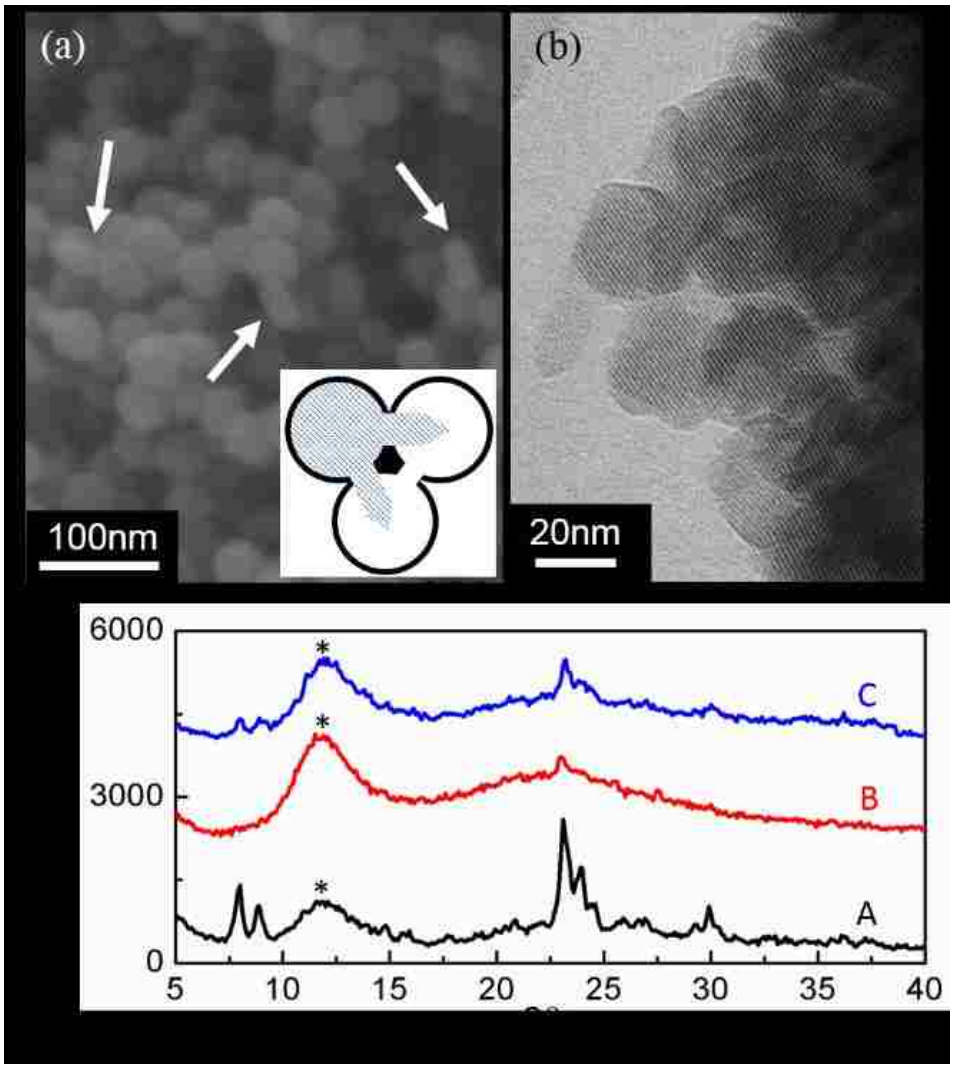

Figure 5-2. (a) SEM and (b) TEM images of silicalite-1 crystals, and (c) WAXS data without carbon template (trace A), before (trace B), and after (trace C) carbon removal (broad peak labeled * is due to adhesives tape used for mounting sample for XRD analysis

5.3.2 Scaffolded growth of silicalite-1 in 3DOm carbon films

A significant original research effort has focused on the translation of the technology confirmed and described above to confined crystal growth in thin (tens of nanometers) 3DOm carbon film structures, an effort aimed at realizing thin zeolite membranes by enforcing nearly in-plane crystal growth. Capillary infiltration was used to impregnate carbon films with zeolite precursor, by dipping a portion of the 3DOm carbon films supported on silicon wafers into an open glass vial containing reactant solution composed of TPAOH clear solution and TEOS. Precursor infiltration was carried out overnight. After removing excess reactants inside the glass vial, we place the glass vial into a Teflon-lined stainless steel autoclave containing sufficient water to produce saturated steam.

Figure 5-3a shows the top of a 3DOm carbon scaffold with apparent silicalite-1 crystals (arrow). The carbon scaffold is highly ordered with approximately 40nm interconnected pore bodies, some of which were found to be filled by silicalite-1 crystals, as shown in **Figure 5-3**b in lower magnification. Exploration of the zeolite-carbon composite films revealed regions having thin carbon films on top of the 3DOm carbon structure (**Figure 5-3**b). It should be noted that the thin nature of the carbon layers leads to their electron transparency in SEM images, enabling observation of underlying silicalite-1 domain structures. These microporous (i.e., rather than mesoporous) carbon layers appear to confine in-plane growth by covering the top of the crystals. This confinement is best illustrated by the infrequent crystal out-growth (i.e., secondary, seeded growth) from the film in the regions lacing the carbon over-layer or in cases with apparent delamination of the thinner carbon layer during the synthesis, leading to bulky “lego-like” structures as a

minor defect (see **Figure 5-4**). SEM (**Figure 5-3**c) clearly shows the 3DOm carbon film within which zeolite crystal domains have grown, and partially grown silicalite-1 crystals are observed as well.

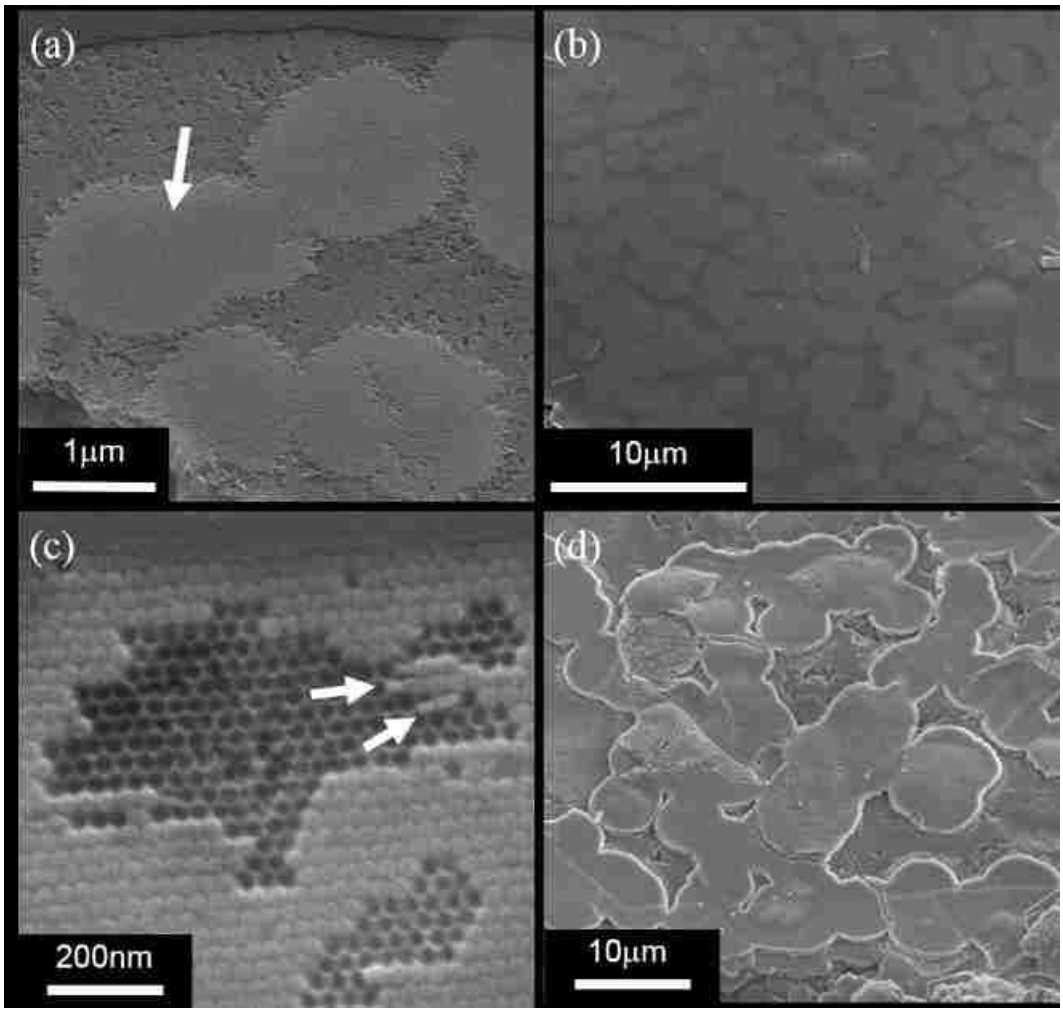

Figure 5-3. SEM images of the (a) propagative growth of silicalite-1 crystals (indicated by the arrows) and (b) Top view of silicalite-1 domains through "electron transparent" carbon top layer; (c) region showing significant filling of carbon films and partially grown silicalite-1 crystals (indicated by the arrows), and (d) remained silicalite-1 domains after burning off the carbon film

After carbon film removal, we observe circular zeolitic domains that appear to intersect one another in large area as shown in **Figure 5-3**d. We hypothesize that each primary circular crystal domain is associated with a single nucleation event occurring within the 3DOm carbon film, with subsequent propagative crystal growth among the interconnected carbon pore bodies. The image suggests that under specific reaction conditions (hydrothermal synthesis at 135℃ for 6 days), distributed nucleation events occur, and result in crystal domain intergrowth to form larger silicalite-1 regions. The size of these domains and their intergrowth may be related to the critical reaction conditions (e.g. reactant concentration, temperature and time), and sufficient mass transport of reactants within the mesoporous carbon scaffold as will be discussed more below.

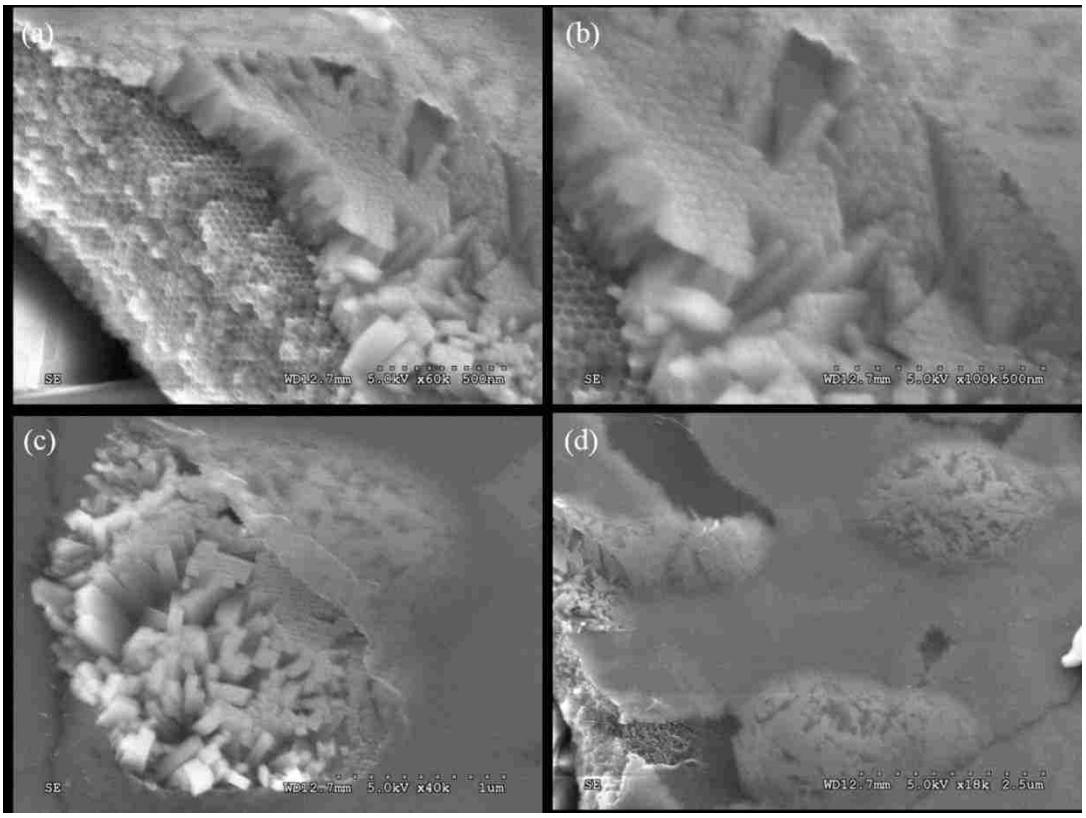

Figure 5-4. SEM images showing secondary outgrowth from templated films giving "Lego-like" structures

5.3.3 Control over morphology and film thickness of silicalite-1 films

Carbon films for confining silicalite-1 crystal growth were prepared by the infiltration of carbon precursor solution into interstitial space of colloidal silica films followed by polymerization and carbonization. After removal of silica film template by KOH etching at room temperature, 3DOm carbon film as a scaffold for confined silicalite-1 crystals growth was obtained. Carbon film thickness was controlled by the thickness of silica film template, which can be tuned via deposition speed and concentration of silica sols. Cross-sections of these crystal domains confined within the carbon films are shown in **Figure 5-5**. These cross-sectional images provide insight into the degree to which the thin 3DOm carbon films are filled by the zeolite crystals. While silicalite-1 domains have been observed in some cases to span only a fraction of the film thickness, numerous regions have also been observed in which crystal domains span the full thickness of the carbon scaffold. After carbon film removal, thin mesoporus silicalite-1 domains are obtained as shown in **Figure 5-5**d, and seem to be mechanically stable after carbon removal from the cross-sectional view since no crystal collapse is observed. The ability to control the carbon film thickness, coupled with the apparent in-plane confinement of zeolite crystal domains within the 3DOm carbon scaffold film, enables us to prepare silicalite-1 films with tunable thickness, and holds the potential to realize continuous ultra-thin silicalite-1 films of tens of nanometers in thickness.

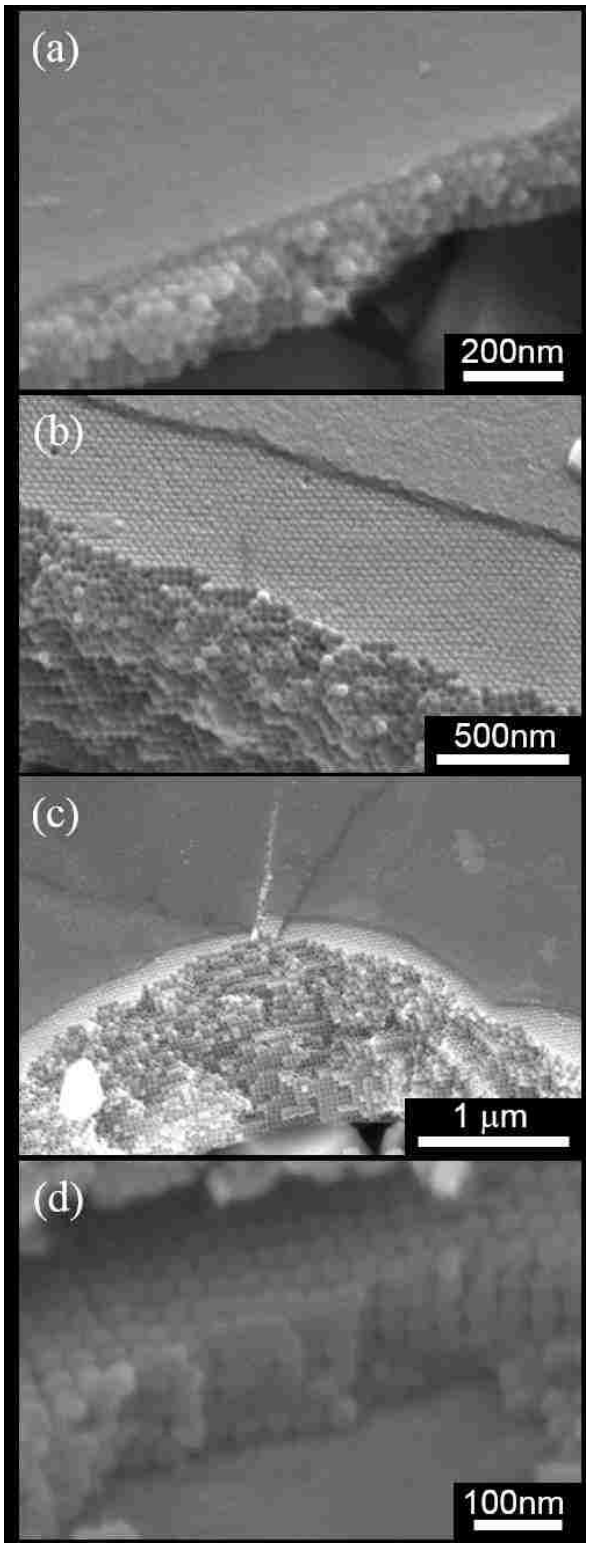

Figure 5-5. Cross-sectional SEM images of the silicalite-1 films templated by the (a) ~200 nm, (b) ~500 nm, and (c) 1 µm carbon film thickness; (d) silicalite-1 film after carbon film removal

The “carbon healed silica colloidal crystal defects” were found in the carbon-zeolite composite films as shown in **Figure 5-6**a. These defects, micro-cracks, originated from the convective assembly of silica nanoparticles were impregnated by carbon precursor solution followed by polymerization and carbonization. Therefore, the cracks of silica films were fully filled with carbons as indicated by arrows in **Figure 5-6**a. The micro-cracks and mesopores templated by carbon walls will re-appear after removing the carbon scaffold, and the secondary zeolite growth to fill these gaps are necessary to establish the separation selectivity in cases where these films are considered for membrane applications. Macroscopically, the nature of inorganic films are brittle and non-flexible, but in the case that the thickness of silicalite-1 films are ~O(100nm), the flexibility can be observed. SEM images in **Figure 5-6**b show the confined silicalite-1 films after carbon film removal. Clearly, the curled silicalite-1 film shown in **Figure 5-6**b shows the macroscopic flexibility owing to the ultrathin nature of confined silicalite-1 films.

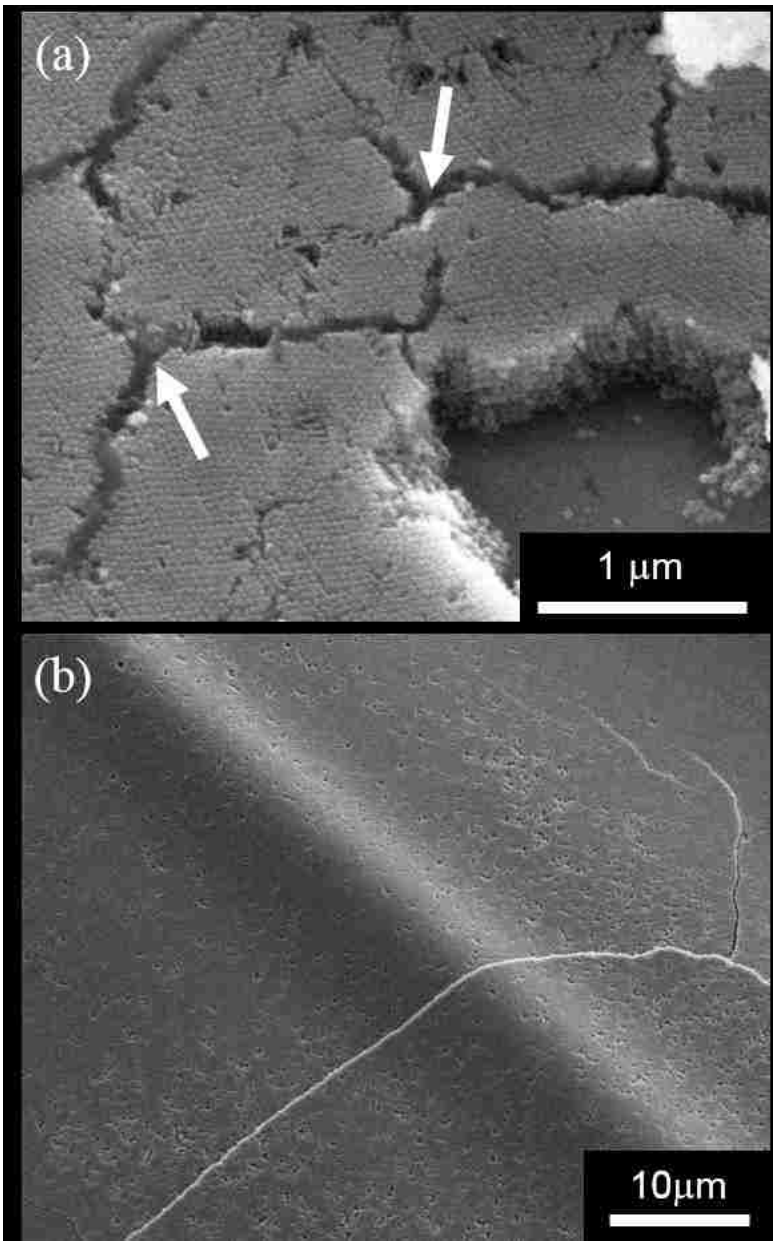

Figure 5-6. SEM images of the silicalite-1 domains showing (a) the carbon healed silica colloidal crystal defect (indicated by the arrows), and (b) the flexibility of silicalite-1 film

5.3.4 Controlling nucleation and scaffolded growth toward film continuity

Beyond secondary closure of imprinted mesoporosity and micro-cracks transferred to the zeolite films by the carbon scaffold, other important synthesis-structure relations requiring elucidation relate to the role of nucleation and growth conditions in achieving large-area film growth toward realizing continuous films. As such, we have studied the nucleation and crystal growth of silicalite-1 within 3DOm carbon films by controlling the zeolite synthesis time during hydrothermal reactions. Reaction temperature was kept constant at 135 ℃, and reaction time was varied from 1 day, 3 days to 6 days by using three structurally identical 3DOm carbon films (~200nm thickness with 40nm pore body and top carbon layer) as scaffolds. The carbon films were immersed in the zeolite precursor overnight, followed by SAC hydrothermal reaction for different period of time. After one day of hydrothermal reaction, micron-sized domains of silicalite-1 crystals were formed within carbon films as shown in **Figure 5-7**a. The inset in **Figure 5-7**a showing the single domain composed of silicalite-1 crystals is indicative of single nucleation and propagative growth of silicalite-1 crystals through carbon pore bodies. The corresponding XRD pattern (**Figure 5-7**d, trace 1d) shows low crystallinity of silicalite-1 crystals after one day reaction. After 3 days and 6 days, the silicalite-1 films were formed by the in-plane intergrowth of individually nucleated silicalite-1 domains as shown in **Figure 5-7**b and c, respectively (insets: corresponding high magnification images). Well-revolved XRD patterns reveal the signature reflection of silicalite-1 (**Figure 5-7**d, trace 3d and 6d). As a result, the hydrothermal synthesis time should be long enough for giving the impregnated zeolite precursor solution energy and time to transform from amorphous gel to crystalline structures resulting in continuous zeolite films.

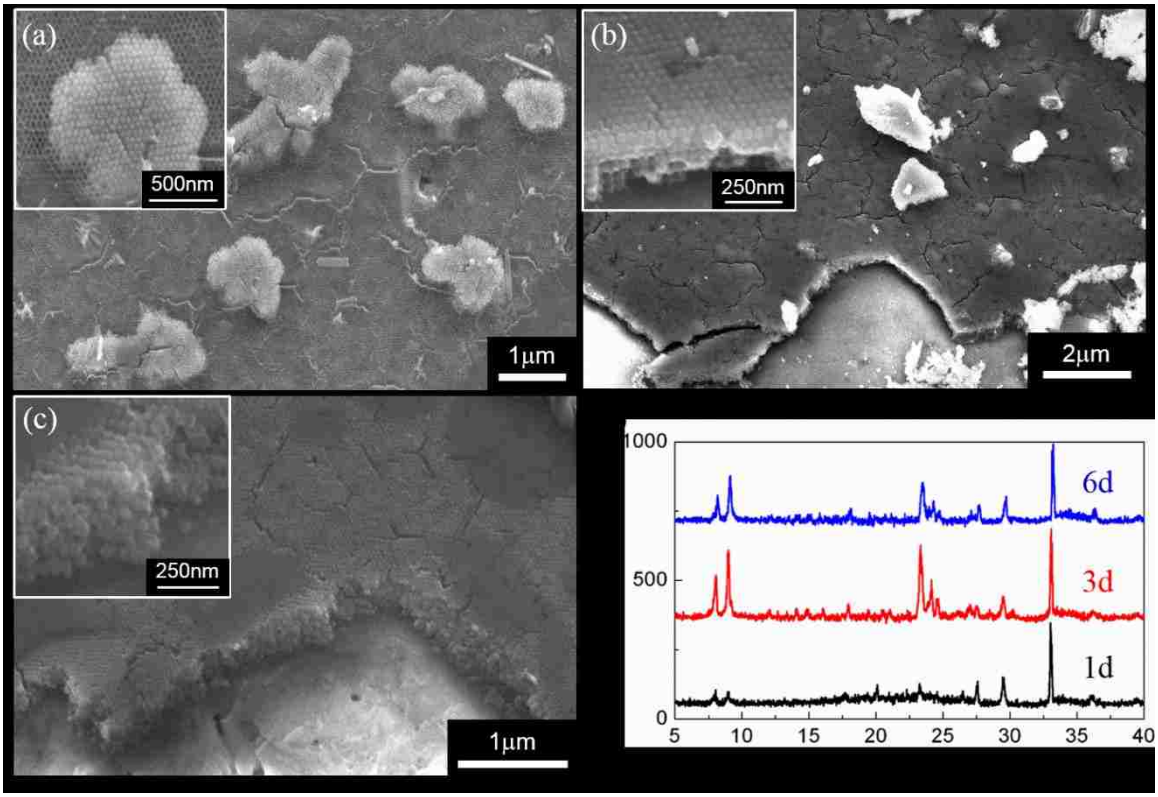

Figure 5-7. SEM images of the silicalite-1 crystal growth at 135℃ after (a) 1 day, (b) 3 days, and (c) 6 days crystallization time (insets: higher magnification). (d) corresponding XRD patterns

5.4 Conclusions

In this work, templated growth of microporous crystalline silicalite-1 crystals using 3DOm carbon films as scaffolds was demonstrated. The 3DOm carbon film was infiltrated by silicalite-1 precursor sol followed by SAC hydrothermal synthesis. After carbon film removal, large intergrown silicalite-1 domains were obtained. The thickness of the silicalite-1 domains can be fine-tuned and scaled down to the order of 10-100 nm by controlling the carbon film thickness. When the film thickness is thin enough, the flexibility of these brittle inorganic films can be observed. The nucleation and crystal growth of silicalite-1 crystals within 3DOm carbon films, from micron-sized silicalite-1 domains to continuous films, can be controlled by zeolite synthesis time during hydrothermal reactions. This scaffolded growth technique of thin zeolite films holds potential to realize high performance molecular separations.

5.5 Reference

1. Lai, Z. P.; Bonilla, G.; Diaz, I.; Nery, J. G.; Sujaoti, K.; Amat, M. A.; Kokkoli, E.; Terasaki, O.; Thompson, R. W.; Tsapatsis, M.; Vlachos, D. G., Microstructural optimization of a zeolite membrane for organic vapor separation. *Science* **2003,** 300, (5618), 456-460.

2. Snyder, M. A.; Tsapatsis, M., Hierarchical nanomanufacturing: From shaped zeolite nanoparticles to high-performance separation membranes. *Angewandte Chemie-International Edition* **2007,** 46, (40), 7560-7573.

3. Himeno, S.; Tomita, T.; Suzuki, K.; Nakayama, K.; Yajima, K.; Yoshida, S., Synthesis and permeation properties of a DDR-type zeolite membrane for separation of CO2/CH4 gaseous mixtures. *Ind. Eng. Chem. Res.* **2007,** 46, (21), 6989-6997.

4. Xomeritakis, G.; Tsapatsis, M., Permeation of aromatic isomer vapors through oriented MFI-type membranes made by secondary growth. *Chemistry of Materials* **1999,** 11, (4), 875-+.

5. Bowen, T. C.; Noble, R. D.; Falconer, J. L., Fundamentals and applications of pervaporation through zeolite membranes. *J. Membr. Sci.* **2004,** 245, (1-2), 1-33.

6. Coronas, J.; Santamaria, J., Separations using zeolite membranes. *Sep. Purif. Methods* **1999,** 28, (2), 127-177.

7. Hedlund, J.; Sterte, J.; Anthonis, M.; Bons, A. J.; Carstensen, B.; Corcoran, N.; Cox, D.; Deckman, H.; De Gijnst, W.; de Moor, P. P.; Lai, F.; McHenry, J.; Mortier, W.; Reinoso, J., High-flux MFI membranes. *Microporous and Mesoporous Materials* **2002,** 52, (3), 179-189.

8. Hedlund, J.; Jareman, F.; Bons, A. J.; Anthonis, M., A masking technique for high quality MFI membranes. *J. Membr. Sci.* **2003,** 222, (1-2), 163-179.

9. Gardner, T. Q.; Martinek, J. G.; Falconer, J. L.; Noble, R. D., Enhanced flux through double-sided zeolite membranes. *J. Membr. Sci.* **2007,** 304, (1-2), 112-117.

10. Sato, K.; Nakane, T., A high reproducible fabrication method for industrial production of high flux NaA zeolite membrane. *J. Membr. Sci.* **2007,** 301, (1-2), 151-161.

11. Kusakabe, K.; Murata, A.; Kuroda, T.; Morooka, S., Preparation of MFI-type zeolite membranes and their use in separating n-butane and i-butane. *J. Chem. Eng. Jpn.* **1997,** 30, (1), 72-78.

12. Lai, Z. P.; Tsapatsis, M.; Nicolich, J. R., Siliceous ZSM-5 membranes by secondary growth of b-oriented seed layers. *Advanced Functional Materials* **2004,** 14, (7), 716-729.

13. Ha, K.; Lee, Y. J.; Lee, H. J.; Yoon, K. B., Facile assembly of zeolite monolayers on glass, silica, alumina, and other zeolites using 3-halopropylsilyl reagents as covalent linkers. *Adv. Mater.* **2000,** 12, (15), 1114-+.

14. Xomeritakis, G.; Gouzinis, A.; Nair, S.; Okubo, T.; He, M. Y.; Overney, R. M.; Tsapatsis, M., Growth, microstructure, and permeation properties of supported zeolite (MFI) films and membranes prepared by secondary growth. *Chemical Engineering Science* **1999,** 54, (15-16), 3521-3531.

15. Lovallo, M. C.; Gouzinis, A.; Tsapatsis, M., Synthesis and characterization of oriented MFI membranes prepared by secondary growth. *Aiche Journal* **1998,** 44, (8), 1903-1913.

16. Choi, J.; Jeong, H. K.; Snyder, M. A.; Stoeger, J. A.; Masel, R. I.; Tsapatsis, M., Grain Boundary Defect Elimination in a Zeolite Membrane by Rapid Thermal Processing. *Science* **2009,** 325, (5940), 590-593.

17. Carreon, M. A.; Li, S. G.; Falconer, J. L.; Noble, R. D., Alumina-supported SAPO-34 membranes for CO2/CH4 separation. *Journal of the American Chemical Society* **2008,** 130, (16), 5412-+.

18. Nishiyama, N.; Gora, L.; Teplyakov, V.; Kapteijn, F.; Moulijn, J. A., Evaluation of reproducible high flux silicalite-1 membranes: gas permeation and separation characterization. *Sep. Purif. Technol.* **2001,** 22-3, (1-3), 295-307.

19. Xomeritakis, G.; Lai, Z. P.; Tsapatsis, M., Separation of xylene isomer vapors with oriented MFI membranes made by seeded growth. *Industrial & Engineering Chemistry Research* **2001,** 40, (2), 544-552.

20. Nomura, M.; Yamaguchi, T.; Nakao, S., Silicalite membranes modified by counterdiffusion CVD technique. *Ind. Eng. Chem. Res.* **1997,** 36, (10), 4217-4223.

21. Yan, Y. S.; Davis, M. E.; Gavalas, G. R., Preparation of highly selective zeolite ZSM-5 membranes by a post-synthetic coking treatment. *J. Membr. Sci.* **1997,** 123, (1), 95-103.

22. Choi, J.; Ghosh, S.; King, L.; Tsapatsis, M., MFI zeolite membranes from a- and randomly oriented monolayers. *Adsorption-Journal of the International Adsorption Society* **2006,** 12, (5-6), 339-360.

23. Lee, I.; Buday, J. L.; Jeong, H. K., mu-Tiles and mortar approach: A simple technique for the facile fabrication of continuous b-oriented MFI silicalite-1 thin films. *Microporous and Mesoporous Materials* **2009,** 122, (1-3), 288-293.

24. Liu, Y.; Li, Y. S.; Yang, W., Fabrication of highly b-oriented MFI monolayers on various substrates. *Chemical Communications* **2009**, (12), 1520-1522.

25. Liu, Y.; Li, Y. S.; Yang, W. S., Fabrication of Highly b-Oriented MFI Film with Molecular Sieving Properties by Controlled In-Plane Secondary Growth. *Journal of the American Chemical Society* **2010,** 132, (6), 1768-+.

26. Lee, I.; Jeong, H. K., Synthesis and gas permeation properties of highly b-oriented MFI silicalite-1 thin membranes with controlled microstructure. *Microporous and Mesoporous Materials* **2011,** 141, (1-3), 175-183.

27. Madsen, C.; Jacobsen, C. J. H., Nanosized zeolite crystals - convenient control of crystal size distribution by confined space synthesis. *Chemical Communications* **1999**, (8), 673-674.

28. Jacobsen, C. J. H.; Madsen, C.; Janssens, T. V. W.; Jakobsen, H. J.; Skibsted, J., Zeolites by confined space synthesis - characterization of the acid sites in nanosized ZSM-5 by ammonia desorption and Al-27/Si-29-MAS NMR spectroscopy. *Microporous and Mesoporous Materials* **2000,** 39, (1-2), 393-401.

29. Schmidt, I.; Madsen, C.; Jacobsen, C. J., Confined space synthesis. A novel route to nanosized zeolites. *Inorganic Chemistry* **2000,** 39, (11), 2279-83.

30. Tao, Y. S.; Kanoh, H.; Kaneko, K., ZSM-5 monolith of uniform mesoporous channels. *Journal of the American Chemical Society* **2003,** 125, (20), 6044-6045.

31. Fan, W.; Snyder, M. A.; Kumar, S.; Lee, P. S.; Yoo, W. C.; McCormick, A. V.; Lee Penn, R.; Stein, A.; Tsapatsis, M., Hierarchical nanofabrication of microporous crystals with ordered mesoporosity. *Nature Materials* **2008,** 7, (12), 984-91.

32. Yoo, W. C.; Stoeger, J. A.; Lee, P. S.; Tsapatsis, M.; Stein, A., High-Performance Randomly Oriented Zeolite Membranes Using Brittle Seeds and Rapid Thermal Processing. *Angewandte Chemie-International Edition* **2010,** 49, (46), 8699-8703.

33. Lee, P. S.; Zhang, X. Y.; Stoeger, J. A.; Malek, A.; Fan, W.; Kumar, S.; Yoo, W. C.; Al Hashimi, S.; Penn, R. L.; Stein, A.; Tsapatsis, M., Sub-40 nm Zeolite Suspensions via Disassembly of Three-Dimensionally Ordered Mesoporous-Imprinted Silicalite-1. *Journal of the American Chemical Society* **2011,** 133, (3), 493-502.

34. Varoon, K.; Zhang, X. Y.; Elyassi, B.; Brewer, D. D.; Gettel, M.; Kumar, S.; Lee, J. A.; Maheshwari, S.; Mittal, A.; Sung, C. Y.; Cococcioni, M.; Francis, L. F.; McCormick, A. V.; Mkhoyan, K. A.; Tsapatsis, M., Dispersible Exfoliated Zeolite Nanosheets and Their Application as a Selective Membrane. *Science* **2011,** 333, (6052), 72-75.

35. Tian, Z.; Snyder, M. A., Hard Templating of Symmetric and Asymmetric Carbon Thin Films with Three-Dimensionally Ordered Mesoporosity. *Langmuir* **2014,** 30, (32), 9828-9837.

36. Tian, Z. Template-mediated, Hierarchical Engineering of Ordered Mesoporous Films and Powders. Ph.D. Thesis, Lehigh University, 2014.

37. Kumnorkaew, P.; Ee, Y. K.; Tansu, N.; Gilchrist, J. F., Investigation of the Deposition of Microsphere Monolayers for Fabrication of Microlens Arrays. *Langmuir* **2008,** 24, (21), 12150-12157.

38. Xu, W. Y.; Dong, J. X.; Li, J. P.; Li, J. Q.; Wu, F., A NOVEL METHOD FOR THE PREPARATION OF ZEOLITE ZSM-5. *Journal of the Chemical Society-Chemical Communications* **1990**, (10), 755-756.

39. Fan, W.; Snyder, M. A.; Kumar, S.; Lee, P. S.; Yoo, W. C.; McCormick, A. V.; Penn, R. L.; Stein, A.; Tsapatsis, M., Hierarchical nanofabrication of microporous crystals with ordered mesoporosity. *Nature Materials* **2008,** 7, (12), 984-991.

Chapter 6:

Conclusions and Future Outlook

6.1 Summary

This dissertation has established the strategies for hierarchical engineering of multimodal ordered porous materials from bottom-up colloidal assembly to top-down hard-templating. Motivation for the ordered mesoporous silicas described in Chapter 2 drove the systematic study of binary assembly of Lys-Sil nanoparticles into template-free ordered mesoporous silicas with three different crystal isostructures (NaCl, AlB_2, $NaZn_{13}$). Chapter 3 provided the fundamental insights into binary colloidal assembly of silica nanoparticles intobulk powder structures to thin film deposition. One of the promising applications of these novel ordered mesoporous silicas was demonstrated in Chapter 4. Namely, a facile method to synthesize bimodal 3DOm carbons with controllable large mesoporosity and pore topology was established by exploiting OMSs as sacrificial hard templates. We believe that this hard templating method can be a platform for realizing multimodal ordered mesoporous materials bearing potential implications on applications spanning from separations, adsorbents, electrode materials, to catalyst supports. In Chapter 5, 3DOm carbon film used as a scaffold for confined growth of thin zeolite films with tunable film thickness was demonstrated. This top-down hard-templating method is versatile that is able to be translated to hard-templating growth of other functional materials promoting higher performance in applications.

6.2 Future Work

We conclude this thesis with future work to extend the established bottom-up assembly of silica nanoparticles towards structural and compositional diversity of binary nanoparticle assembly with preliminary proof-of-concept data. In addition, the potential extension of research of bimodal 3DOm carbons is summarized.

6.2.1 Structural diversity of binary silica nanoparticle assemblies

6.2.1.1 Introduction

In spite of the realization of binary silica nanoparticle superlattices with three different frameworks isostructural with NaCl, AlB_2, and $NaZn_{13}$, which is consistent with the prediction of hard-sphere models, continuing work is necessary to increase the *structural diversity of binary silica nanoparticle superlattices* resulting in better pore topology control of these novel ordered mesoporous silicas. As mentioned previously, the binary nanoparticle superlattices (BNSLs), composed of semiconducting, metallic, and magnetic nanoparticles, are identified with more than 15 different structure types, and at least 10 were in low packing density structures (packing density $\phi<0.74$), which were out of the theoretical calculation and simulation of space-filling principle and the hard-sphere model.[1-7] Although detailed mechanisms of formation of a variety of BNSL structures is unclear, it is demonstrated that at the nanometer scale, *electrical charges on sterically stabilized nanoparticles* determine the BNSL stoichiometry and additional contributions from *entropic, van der Waals, steric and dipolar forces* stabilize the variety of BNSL structures.[8] A series of computational results by Monte Carlo simulations[9] has been reported showing that the phase behavior of binary mixtures of nanoparticles, depending

on the free energy, is a function of the different charges and size ratios based on tuning the balance between dispersion and electrostatic forces. It suggests that at the nanoscale, both electrostatic and dispersion interactions should be taken into account to explain the experimentally observed BNSL structures.

In this work, we aimed to modify the surface chemistry of silica nanoparticles to control both positive and negative surface charge and steric stabilization on the particle surface, and study the phase behavior in binary assembly of these surface-modified silica nanoparticles.

6.2.1.2 Experimental

Polyethyleneimine (PEI) modification process The modification of the surface charge of silica nanoparticles was reported previously[10]. In brief, 3 mL of 1M HCl was added into 10 ml of 40 nm Lys-Sil sols (11.84 wt%). 100 to 1000 μL trimethoxysilylpropyl modified polyethyleneimine (Gelest) was slowly added (injection rate=2.1 mL/h) by syringe pump (Fisher) into the silica solution while stirring vigorously. The final pH of the silica solution was 1.2. The mixture was then heated to 60℃ for 24 h with stirring at 500 rpm. The mixture was washed by centrifugation at 20000 rpm for 60 min followed by replacement of supernatant with water at a pH~4.0 (the pH was adjusted by 0.25 M HCl). This washing process was repeated 3 times. The particles were re-dispersed in water with a pH of 4.0 by sonication and stored at 4℃.

6.2.1.3 Preliminary results and discussion

DLS, zeta-potential measurement, and TEM were carried out to study the particle size distribution, surface charges, and packing ordering of PEI-silica NPs.

In **Figure 6-1**a, DLS results show the particle size distribution of unmodified 20nm sols with pH of 9.5 (black line) and 4.0 (red line), and unmodified (blue line) and modified (green line) 40nm silica sols with pH of 9.0 and 4.0, respectively. It is observed that the size distribution of the 20nm silica particles is narrow, while that of the 40nm silica particles appears relatively broad, caused possibly by the seeded growth. Besides, the particle size of 20nm silica NPs with a pH of 4.0, which is adjusted by 0.25M HCl, is a bit larger than the as-made one. This probably results from the higher ionic concentration, which thickens the electric double layer of silica NPs from HCl titration. Surface-modified 40nm silica sols after multiple washing and centrifugation processes display a similar particle size distribution as the unmodified one.

TEM images shown in **Figure 6-1**b and c reveal the packing structures after evaporation of *unary* unmodified 20nm and PEI-modified 40nm silica sols with a pH of 4.0. Dense but disordered assembly of unmodified 20nm silica NPs are observed in **Figure 6-1**b caused probably by lack of electrostatic stabilization of silica NPs owing to low surface charge. TEM of PEI-modified 40nm silica NPs, as shown in **Figure 6-1**c, shows highly 3D-ordered positively charged (+49.8mV) 40nm silica NPs after evaporation-induced convective assembly.

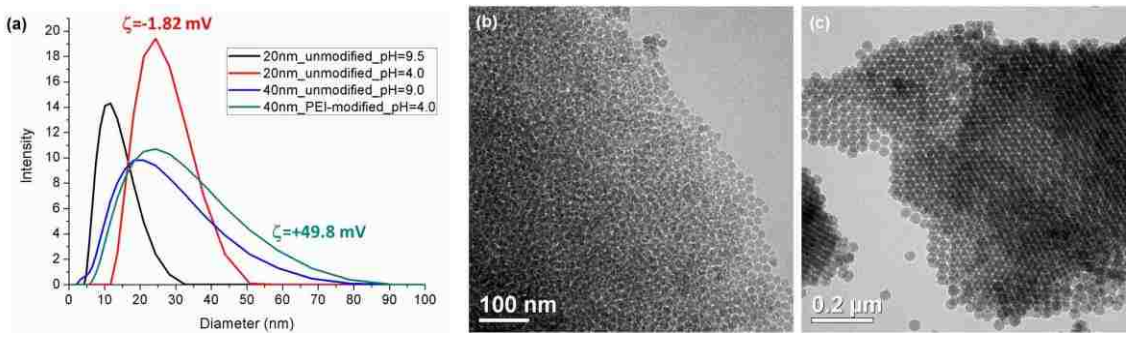

Figure 6-1. (a) Particle size distribution of 20 and 40nm silica NPs with and without PEI-modification. TEM images of (b) 20nm unmodified and (c) 40nm PEI-modified silica NPs (pH=4)

Binary silica NP mixtures are prepared by mixing negatively charged unmodified 20nm silica sol and positively charged 40nm PEI-modified silica sols with a pH of 4. TEM images in **Figure 6-2** show the binary silica mixture is dense but disordered. It is worthy to note that the mixture solution becomes cloudy and precipitates immediately while mixing these two different silica sols, which means the dispersion of silica NPs in the mixture is not stable. We attribute this instability to the strong electrostatic attractive force between the oppositely charged silica sols. The ability to well control the surface charges of oppositely charged silica NPs seems to be critical to balance the electrostatic and dispersion interactions.

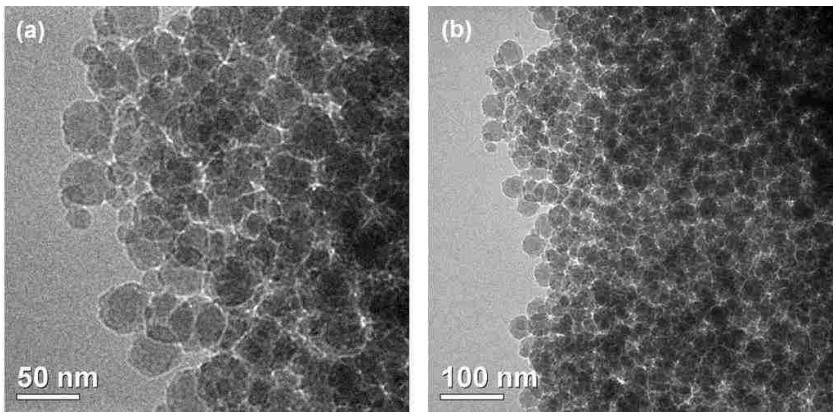

Figure 6-2. TEM images of the binary mixture of unmodified 20 and PEI-modified 40nm silica NPs at high (a), and low magnification (b)

Attempts to control the surface charges of PEI-modified 40nm silica sols were made first by changing the reaction time of PEI in 40nm silica sols to graft different amounts of PEI on the silica surface. Specifically, after the addition of PEI solution in the 40nm silica sol, the mixture was heated at 60°C for different periods of time spanning 1, 3, 6, 13, 18 to 22 hours, followed by the same washing procedures as described previously. The particle size distributions of the silica sols with different reaction/functionalization times are shown in **Figure 6-3**a. The stable particle dispersion and similar particle size distribution of all silica sols is observed. The zeta potential measurement, as shown in **Figure 6-3**b, indicates that there is no significant difference of surface charges of these silica sols under controlled functionalization times.

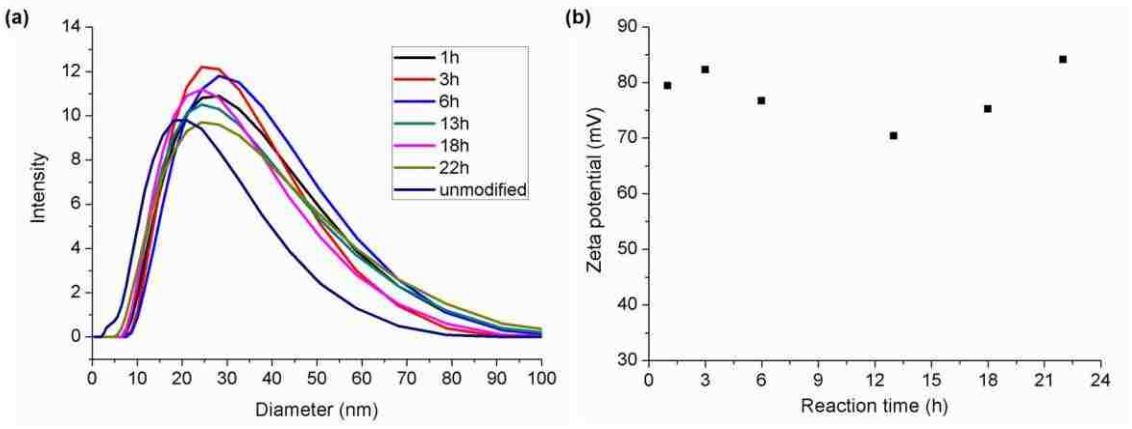

Figure 6-3. (a) Particle size distribution and (b) zeta potential measurement of PEI-modified 40nm silica NPs with different reaction times.

6.2.1.4 Preliminary conclusions and future work

According to the preliminary experimental results, it seems that the ability to broaden the window for tuning the charges of silica NPs to balance the electrostatic and dispersion interactions is critical. Future follow-up work to these challenges may include:

1) Further reducing the PEI reaction times from 10 to 30 minutes to see if kinetic control of PEI grafting density on the silica surface can be achieved.
2) Tuning the amount of PEI added in silica sols during the modification procedure to adjust the amount of PEI grafted on the silica surface.
3) Modifying the silica NPs by another functionalization agent, e.g. TMAPS, following the same modification procedures of PEI.

If the surface charges of silica NPs can be well-controlled, the assembly of binary silica mixture could be studied to determine:

1) Effects of additional electrostatic interaction between oppositely charged silica NPs with different charge ratios on BSNS structure types

2) Effects of changing particle size ratios from 0.2 to 0.7, and changing particle number ratios from 1 to 15 on BSNS structure types

The design rules for binary silica nanoparticle superlattices with diverse structure types could be developed after realizing the above systematic studies. These could lay the foundation to answer such fundamental questions as to if, how and why the BSNS structure is influenced by the electrostatic and dispersion interactions beyond what is predicted by theory and simulation of space-filling principles and hard-sphere model? This would also help to possibly expand the materials palette to other mixed binary nanoparticle systems?

6.2.2 Compositional diversity of binary nanoparticles

6.2.2.1 Introduction

Recently, catalytic nanoparticles (NPs) supported by mesoporous active oxides have attracted much research effort, and seem to have high potential for practical applications because of their high catalytic performance and environmentally friendly properties.[11, 12] The applicability and performance of ordered mesoporous silicas in the field of catalytic applications has been investigated because of the mesoporous architecture and capability of OMSs to be functionalized, facilitating the mass transport of reactant and product in the broad range of catalytic processes. Since there are no intrinsically active catalytic sites in OMS, introduction of catalytically active heteroatoms/nanoparticles either by direct synthesis or post-synthesis to enhance the acidic strength and catalytic activity of OMS is necessary.

In terms of incorporating catalytic NPs on the walls of OMS, the most common way is to impregnate the precursor solution of catalytic NPs into mesoporous framework

of OMS followed by reduction of precursor salts to form catalytic NPs. Small particle size (few nanometers in diameter) and good distribution of catalytic NPs in OMS supports are reported as critical factors on catalytic performance.[13-16] In general, during the processes of reduction and catalytic reaction, the size of catalytic NPs will be increased due to Ostwald ripening and/or particle migration-coalescence that consequently change the distribution of catalytic NPs in the supports and interfacial surface area between catalytic NPs and oxide supports.[16-19]

It is believed that the pore architecture and surface functionality of OMS have great impact on stability of catalytic nanoparticles. In the research of confinement of catalytic NPs in OMS, 1D pore structure with less pore interconnectivity are found to have better catalytic performance than 3D pore structure[18, 20], and it is hypothesized that catalytic NPs confined in 1D channels prevent extensive particle aggregation. However, if the 1D pore channel is blocked by coke or other deactivation, the catalytic performance decreases since there is no interconnectivity with adjacent pore channels.[21] Surface functionality plays another important role of improving the stability of catalytic NPs. It is reported that surface-modified OMSs can improve the stability of catalytic NPs by facilitating stronger particle anchoring.[16, 18] The limitation of OMS-supported catalysts that we aim to address in this work is: 1) low hydrothermal stability of OMS support; 2) limited confinement of catalytic NPs of 1D ordered OMS; and 3) small window/entrance size of interconnected pores channels of OMS.

Previously, we have discussed how purely siliceous binary nanoparticle superlattices can be assembled from solution (Chapters 2 and 3) and high-fidelity carbon replicas can be made (Chapter 4). Here, we aim to extend this assembly to multi-functional

binary nanoparticle superlattices, since 3D ordered mesoporous binary silica nanoparticle superlattices, as discussed previously, seem to be a good model to study the feasibility of assembling binary catalytic/silica nanoparticles. Two possible approaches to assemble the binary nanoparticles into 3D ordered mesoporous structures are schematically illustrated in **Figure 6-4**. The first approach, as shown in **Figure 6-4**a, is to replace the small silica nanoparticle in BSNS during the assembly process with the catalytic nanoparticle, and further replica can be prepared if needed. Owing to the close-packed crystal structure, the approach should lead to the catalytic NPs being ***well-distributed*** and ***confined*** in the silica NPs structure. We also hypothesize that the ***hydrothermal stability*** will be enhanced relative to conventional OMSs owing to the increased silica wall thickness (tens of nanometer) compared with OMSs (up to few nanometers). In addition, the ***3D-interconnected pore structures*** provide alternative transport pathways if pore blocking occurs during the catalysis (e.g., coke formation), given the trade-off between pore interconnectivity and the stability of catalytic NPs in the case of OMSs. If binary metal/silica nanoparticle superlattices could be realized, the confinement of metal NPs by the close-packed binary silica could help to bolster stability of the catalytic moieties against migration and aggregation. A second approach of assembling silica and core-shell nanoparticles, as shown in **Figure 6-4**b, could exploit core-shell particles constructed by silica encapsulation of core catalytic nanoparticles with controllable shell thickness to enable ***reduction of the size of the catalytic NPs*** and to ***ease the assembly of binary nanoparticles***.

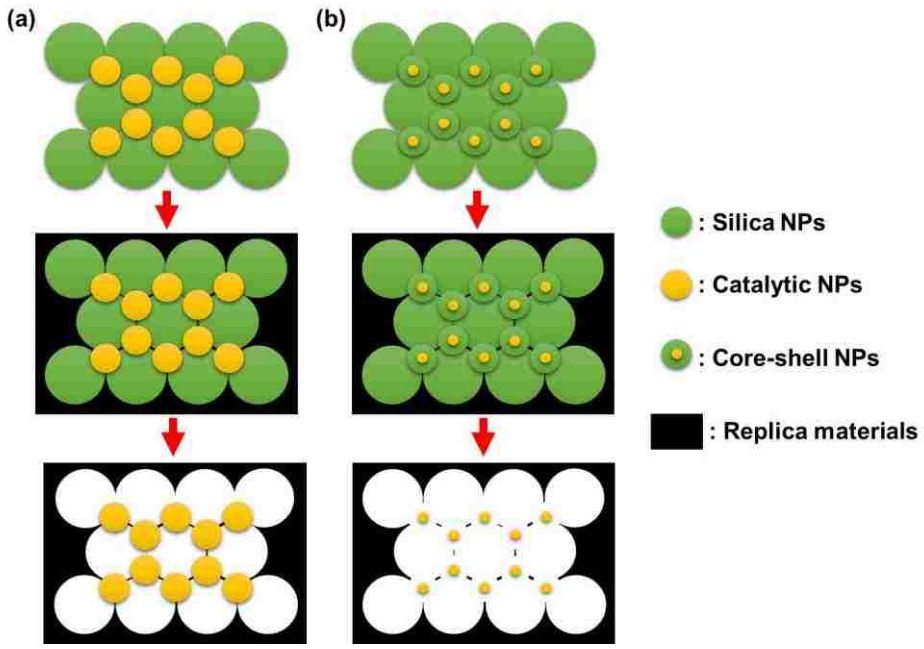

Figure 6-4. Schematic illustration of design of multi-funtional binary nanoparticles composites. (a) Binary silica/catalytic nanoparticle superlattices, and (b) binary silica/catalyst-silica (core-shell) nanoparticle superlattices.

Subsequent replica engineering of these two binary catalytic-silica NPs superlattices would enable realization of various supported catalyst materials with 3D ordered mesopores by infiltrating and solidifying the desired replica material (e.g., carbon as in Chapter 4) followed by etching of the silica template. This approach would potentially lead to confinement of the catalytic NPs within the replica frameworks. Depending on the applications, the source of replica materials can be from various functional materials, such as carbon, zirconia, titania, among others, to be applied for a broad range of catalytic reactions. The possible challenge to these approaches would be: 1) preparation of highly monodisperse catalytic nanoparticles with desirable sizes; and 2) rational and fine control of the interactions between siliceous and metallic nanoparticles.

6.2.2.2 Experimental

Synthesis of Au@SiO_2 core-shell structures

The synthesis of Au@SiO2 core-shell nanoparticles consists of two parts. First, a very thin silica layer was formed on the surface of 20nm gold nanoparticles (BBI Solutions, EM GC20), followed by secondary seeded growth of silica shell by using the thin silica coated gold nanoparticle as the seed. In order to form a thin silica layer on the gold surface, the gold nanoparticles were modified by (3-Aminopropyl)triethoxysilane (APTES, Sigma-Aldrich, 99%). 1mM APTES aqueous solution was prepared fresh by adding 19μL APTES in 80mL water with vigorous stirring. To cap the gold nanoparticles with APTES molecules, 74μL 1mM APTES was added into 20mL colloidal gold solution with vigorous stirring. Sodium silicate was used as the silica source for coating a thin silica layer on the APTES-modified gold surface. The sodium silicate solution (Sigma-Aldrich, 27%) was filtered by 0.45 μm syringe filter, and diluted to 0.54% by D.I. water. 0.8 mL of 0.54% sodium silicate solution was added into 20mL of gold nanoparticles coated with a thin silica layer, and reacted at room temperature with vigorous stirring for 2 days. After reaction, the mixture was washed by centrifugation at 4000 rpm for 6 hours, and re-dispersed in D.I. water, which was used as the "seed solution". To make a thick silica shell on the gold surface, 31μL 16% lysine was added into 5mL of the seed solution, and heated to 90℃, followed by addition of 15mL tetraethyl orthosilicate (TEOS) with vigorous stirring for 2 days. The solution was washed by centrifugation at 4000 rpm for 6 hours, and re-dispersed in D.I. water.

6.2.2.3 Preliminary results and discussion

The starting point of this work as the test bed is the ***assembly of binary gold/silica nanoparticles*** because the supported gold nanoparticles as catalysts hold high potential for numerous catalytic reactions (e.g., oxidation of CO[22, 23], epoxidation of propylene[24, 25], oxidation of alkanes to alcohols and ketones[15, 26]). In terms of the material properties related to the particle interactions during assembly, it was found that the gold NPs, like silica NPs, are negatively charged over a broad range of pH values, and are susceptible to modification by lysine molecules with stable dispersion. In addition, core-shell or yolk-shell structures of gold-silica nanoparticles have been investigated for decades[27-30], which could be adopted in this work.

Based on the model of the AB_2 binary silica nanoparticle superlattice, which is isostructural with AlB_2 and composed of 20/40nm silica NPs as shown in **Figure 6-5**, initial work aimed to replace the 20nm silica NPs with 20nm gold NPs, as illustrated in **Figure 6-5**b. The work started from the synthesis of 20nm gold NPs according to the published literature, but the results showed limited promise for further application. First, the shape of as-made colloidal gold NPs was not uniformly spherical. As shown in **Figure 6-6**a, triangle-, rectangular, and even irregular-shape gold NPs were obtained. Moreover, the broad size distribution (calculated from ~100 measured particle sizes in TEM images, standard deviation>10%, shown in **Figure 6-6**b) is not ideal for direct assembly of 3D ordered binary nanoparticles in this first approach as illustrated in **Figure 6-4**a. It is important to note that the commercial gold colloidal solutions (BBI Solutions, EM GC20) seem to have similar morphology, such as irregular shape and broad size distribution, as those synthesized in the lab.

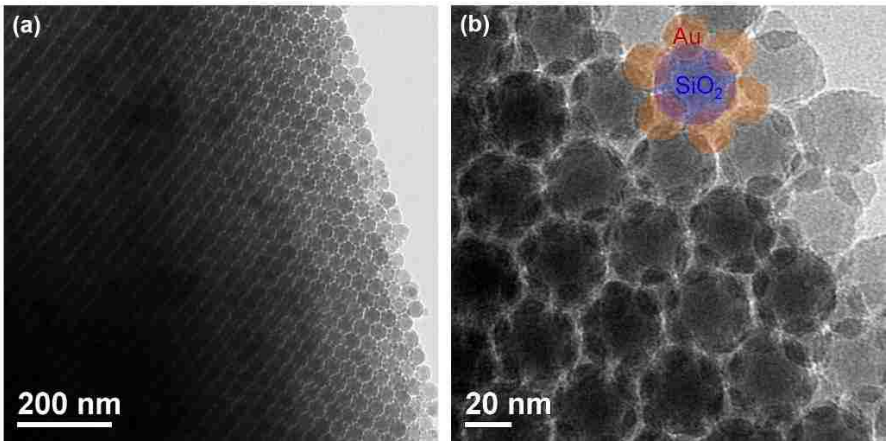

Figure 6-5. Model for binary gold/silica nanoparticle assembly. Binary silica nanoparticle superlattices (a), and illustration of targeted binary silica/gold nanoparticle superlattice (b).

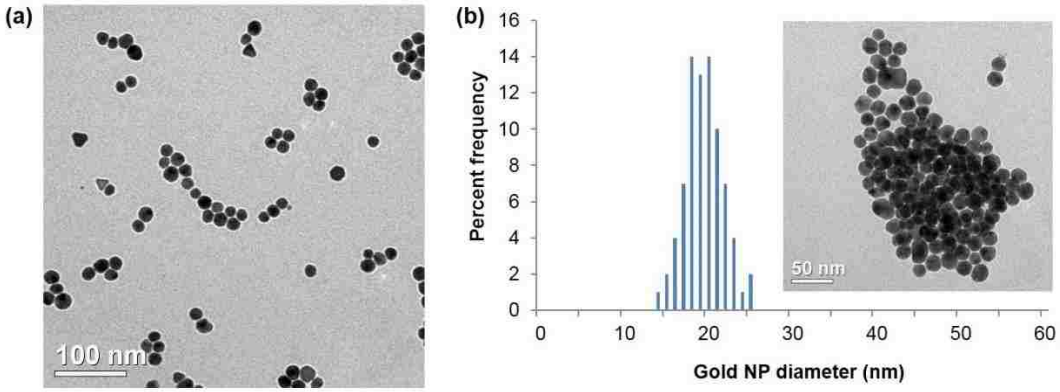

Figure 6-6. Synthesized gold NPs. Non-spherical shapes of gold NPs (a), and broad size distribution (b).

In the second approach illustrated in **Figure 6-4**b, we synthesized Au@SiO2 core-shell nanoparticles. Efforts to make this core-shell structure aim 1) to cover the gold surface with a silica shell to facilitate the binary assembly with pure silica nanoparticles, since we found that direct assembly of gold and silica nanoparticles resulted in disordered structure with large segregation of gold and silica nanoparticles, and 2) to narrow down the particle

size distribution so that the ordered binary assembly of silica and Au@SiO_2 could be realized.

The preliminary results of the synthesis of Au@SiO2 core-shell nanoparticles are shown in **Figure 6-7**. Spherical core-shell nanoparticles (**Figure 6-7**a) were found to be composed of 20nm gold nanoparticle as the core with silica shell with ~20nm thickness. In addition, pure silica nanoparticles and irregularly shaped core-shell nanoparticles were found as well (**Figure 6-7**bcd), probably due to unremoved silica speciesnuclei in solution and new nucleation of silica nanoparticles during the synthesis. The as-made Au@SiO_2 core-shell nanoparticle sols were dried at ambient condition and characterized by SEM as shown in **Figure 6-7**e. A dense but disordered structure composed of primary Au@SiO_2 nanoparticles was found, which suggests the particle shape and size distribution are critical to form a high ordered assembly of nanoparticles.

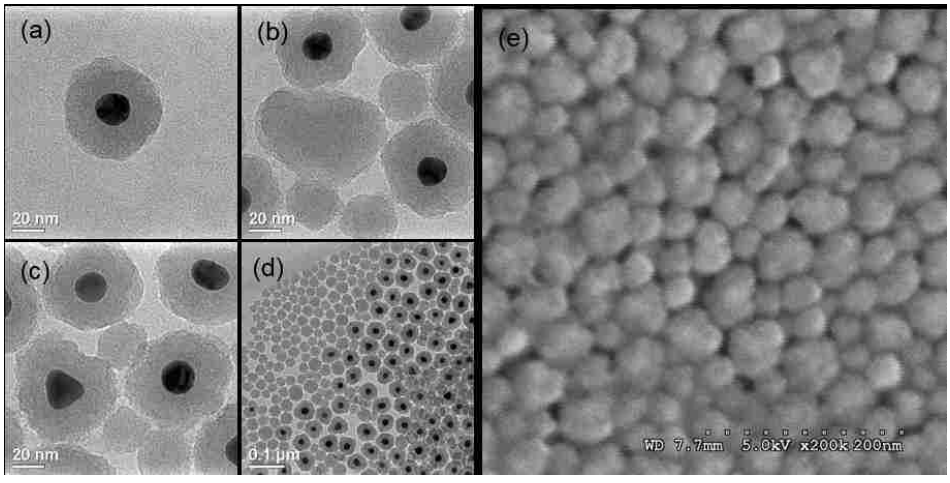

Figure 6-7. TEM (a to d) and SEM (e) images of Au@SiO_2 core-shell nanoparticles

6.2.2.4 Preliminary conclusions and future work

Two approaches to realize the binary metal/silica assembly were carried out. First, the gold nanoparticles were successfully synthesized in the lab, but we found that the particle shapes (e.g., spherical, triangle and irregular) as well as the particle size distribution hampered the formation of ordered binary colloidal assembly. Second, $Au@SiO_2$ core-shell nanoparticles were synthesized in the lab, but similar challenges of particle shape and size uniformity encountered in first approach persisted here as well.

In order to address these challenges, future work could involve the following:

1) Identification of strategies for synthesizing spherical gold nanoparticles with narrow particle size distribution.
2) Stabilization of gold nanoparticles by electrostatic and/or steric stabilizations to balance the attractive forces during the direct binary assembly process in the first approach.
3) Synthesis of $Au@SiO_2$ core-shell nanoparticle sols with regular spherical shape, narrow particle size distribution, and high purity will be critical to form ordered binary assemblies.

All of these studies will develop the fundamental insight to answer the questions: 1) Besides the binary silica NP superlattices, can the binary metal/silica NP superlattices be realized?; 2) How is the structure of binary metal/silica superlattice controlled?; 3) Can metal NPs be confined in the close-packed silica structures or dense replicas to prevent the aggregation of metal NPs?; 4) What is the difference of the effect of confinement on catalytic NPs stability between different binary structure types?

6.2.3 Bimodal Three-dimensionally Ordered Mesoporous Carbons

In Chapter 4, we have demonstrated a facile method to synthesize bimodal three-dimensionally ordered mesoporous (b-3DOm) carbons with tunable large bimodal mesoporosity and 3D-interconnected mesopores by using the template-free OMSs as hard sacrificial templates (discussed in Chapter 2). These novel materials bear a high potential to be applied in many fields, such as adsorbents[31-33], energy conversion and storage systems[34-37], catalysts and supports[38-40], electrode materials[41, 42], and other emerging applications. Future work of key interest for translation of the findings presented in this Dissertation to specific applications, should consider:

1) Evaluating the performance of b-3DOm carbons compared with commercial carbons, such as carbon black. Carbon materials used as electrode materials would be a standard testing application.

2) The material properties, such as mechanical and chemical properties, of carbons could be influenced by different carbon precursors used in hard-templating of b-3DOm carbons. Other monomers rather than furfuryl alcohol could be used as carbon precursors, such as phenol-formaldehyde, resorcinol-formaldehyde, and sucrose.

3) Beyond carbon materials, other functional materials could be infiltrated into OMSs (demonstrated in Chapter 2) to realize the multimodal porous functional materials for emerging applications.

6.3 Reference

1. Bartlett, P.; Ottewill, R. H.; Pusey, P. N., Superlattice formation in binary-mixtures of hard-sphere colloids. *Phys. Rev. Lett.* **1992,** 68, (25), 3801-3804.

2. Cottin, X.; Monson, P. A., A cell theory for solid-solutions - application to hard-sphere mixtures. *J. Chem. Phys.* **1993,** 99, (11), 8914-8921.

3. Eldridge, M. D.; Madden, P. A.; Frenkel, D., Entropy-driven formation of a superlattice in a hard-sphere binary mixture. *Nature* **1993,** 365, (6441), 35-37.

4. Eldridge, M. D.; Madden, P. A.; Frenkel, D., A computer-simulation investigation into the stability of the ab2 superlattice in a binary hard-sphere system. *Mol. Phys.* **1993,** 80, (4), 987-995.

5. Eldridge, M. D.; Madden, P. A.; Pusey, P. N.; Bartlett, P., Binary hard-sphere mixtures - a comparison between computer-simulation and experiment. *Mol. Phys.* **1995,** 84, (2), 395-420.

6. Trizac, E.; Eldridge, M. D.; Madden, P. A., Stability of the AB crystal for asymmetric binary hard sphere mixtures. *Mol. Phys.* **1997,** 90, (4), 675-678.

7. Hunt, N.; Jardine, R.; Bartlett, P., Superlattice formation in mixtures of hard-sphere colloids. *Phys. Rev. E* **2000,** 62, (1), 900-913.

8. Shevchenko, E. V.; Talapin, D. V.; Murray, C. B.; O'Brien, S., Structural characterization of self-assembled multifunctional binary nanoparticle superlattices. *Journal of the American Chemical Society* **2006,** 128, (11), 3620-3637.

9. Ben-Simon, A.; Eshet, H.; Rabani, E., On the Phase Behavior of Binary Mixtures of Nanoparticles. *Acs Nano* **2013,** 7, (2), 978-986.

10. Atchison, N.; Fan, W.; Brewer, D. D.; Arunagirinathan, M. A.; Hering, B. J.; Kumar, S.; Papas, K. K.; Kokkoli, E.; Tsapatsis, M., Silica-Nanoparticle Coatings by Adsorption from Lysine-Silica-Nanoparticle Sols on Inorganic and Biological Surfaces. *Angewandte Chemie-International Edition* **2011,** 50, (7), 1617-1621.

11. Taguchi, A.; Schuth, F., Ordered mesoporous materials in catalysis. *Microporous and Mesoporous Materials* **2005,** 77, (1), 1-45.

12. White, R. J.; Luque, R.; Budarin, V. L.; Clark, J. H.; Macquarrie, D. J., Supported metal nanoparticles on porous materials. Methods and applications. *Chemical Society Reviews* **2009,** 38, (2), 481-494.

13. Sehested, J., Four challenges for nickel steam-reforming catalysts. *Catal Today* **2006,** 111, (1-2), 103-110.

14. Chi, Y. S.; Lin, H. P.; Mou, C. Y., CO oxidation over gold nanocatalyst confined in mesoporous silica. *Applied Catalysis a-General* **2005,** 284, (1-2), 199-206.

15. Chen, L. F.; Hu, J. C.; Richards, R., Intercalation of Aggregation-Free and Well-Dispersed Gold Nanoparticles into the Walls of Mesoporous Silica as a Robust "Green" Catalyst for n-Alkane Oxidation. *Journal of the American Chemical Society* **2009,** 131, (3), 914-+.

16. Jin, Y.; Wang, P. J.; Yin, D. H.; Liu, J. F.; Qiu, H. Y.; Yu, N. Y., Gold nanoparticles stabilized in a novel periodic mesoporous organosilica of SBA-15 for styrene epoxidation. *Microporous and Mesoporous Materials* **2008,** 111, (1-3), 569-576.

17. Bore, M. T.; Pham, H. N.; Switzer, E. E.; Ward, T. L.; Fukuoka, A.; Datye, A. K., The role of pore size and structure on the thermal stability of gold nanoparticles within mesoporous silica. *Journal of Physical Chemistry B* **2005,** 109, (7), 2873-2880.

18. Gabaldon, J. P.; Bore, M.; Datye, A. K., Mesoporous silica supports for improved thermal stability in supported Au catalysts. *Topics in Catalysis* **2007,** 44, (1-2), 253-262.

19. Zhong, Z. Y.; Lin, J. Y.; Teh, S. P.; Teo, J.; Dautzenberg, F. M., A rapid and efficient method to deposit gold particles on catalyst supports and its application for CO oxidation at low temperatures. *Advanced Functional Materials* **2007,** 17, (8), 1402-1408.

20. Yu, N. Y.; Ding, Y.; Lo, A. Y.; Huang, S. J.; Wu, P. H.; Liu, C.; Yin, D. H.; Fu, Z. H.; Yin, D. L.; Hung, C. T.; Lei, Z. B.; Liu, S. B., Gold nanoparticles supported on periodic mesoporous organosilicas for epoxidation of olefins: Effects of pore architecture and surface modification method of the supports. *Microporous and Mesoporous Materials* **2011,** 143, (2-3), 426-434.

21. Rolison, D. R., Catalytic nanoarchitectures - The importance of nothing and the unimportance of periodicity. *Science* **2003,** 299, (5613), 1698-1701.

22. Park, J. Y.; Lee, H.; Renzas, J. R.; Zhang, Y. W.; Somorjai, G. A., Probing hot electron flow generated on Pt nanoparticles with Au/TiO2 Schottky diodes during catalytic CO oxidation. *Nano Lett.* **2008,** 8, (8), 2388-2392.

23. Tai, Y.; Yamaguchi, W.; Tajiri, K.; Kageyama, H., Structures and CO oxidation activities of size-selected Au nanoparticles in mesoporous titania-coated silica aerogels. *Applied Catalysis a-General* **2009,** 364, (1-2), 143-149.

24. Huang, J. H.; Akita, T.; Faye, J.; Fujitani, T.; Takei, T.; Haruta, M., Propene Epoxidation with Dioxygen Catalyzed by Gold Clusters. *Angewandte Chemie-International Edition* **2009,** 48, (42), 7862-7866.

25. Nijhuis, T. A. R.; Visser, T.; Weckhuysen, B. M., The role of gold in gold-titania epoxidation catalysts. *Angewandte Chemie-International Edition* **2005,** 44, (7), 1115-1118.

26. Zhao, R.; Ji, D.; Lv, G. M.; Qian, G.; Yan, L.; Wang, X. L.; Suo, J. S., A highly efficient oxidation of cyclohexane over Au/ZSM-5 molecular sieve catalyst with oxygen as oxidant. *Chemical Communications* **2004**, (7), 904-905.

27. Graf, C.; Vossen, D. L. J.; Imhof, A.; van Blaaderen, A., A general method to coat colloidal particles with silica. *Langmuir* **2003,** 19, (17), 6693-6700.

28. Lee, J.; Park, J. C.; Song, H., A nanoreactor framework of a Au@SiO2 yolk/shell structure for catalytic reduction of p-nitrophenol. *Adv. Mater.* **2008,** 20, (8), 1523-+.

29. Liz-Marzan, L. M.; Giersig, M.; Mulvaney, P., Synthesis of nanosized gold-silica core-shell particles. *Langmuir* **1996,** 12, (18), 4329-4335.

30. Lu, Y.; Yin, Y. D.; Li, Z. Y.; Xia, Y. N., Synthesis and self-assembly of Au@SiO2 core-shell colloids. *Nano Lett.* **2002,** 2, (7), 785-788.

31. Zhuang, X.; Wan, Y.; Feng, C. M.; Shen, Y.; Zhao, D. Y., Highly Efficient Adsorption of Bulky Dye Molecules in Wastewater on Ordered Mesoporous Carbons. *Chemistry of Materials* **2009,** 21, (4), 706-716.

32. Vinu, A.; Miyahara, M.; Sivamurugan, V.; Mori, T.; Ariga, K., Large pore cage type mesoporous carbon, carbon nanocage: a superior adsorbent for biomaterials. *J. Mater. Chem.* **2005,** 15, (48), 5122-5127.

33. Wu, Z. X.; Webley, P. A.; Zhao, D. Y., Comprehensive Study of Pore Evolution, Mesostructural Stability, and Simultaneous Surface Functionalization of Ordered Mesoporous Carbon (FDU-15) by Wet Oxidation as a Promising Adsorbent. *Langmuir* **2010,** 26, (12), 10277-10286.

34. Zhai, Y. P.; Dou, Y. Q.; Zhao, D. Y.; Fulvio, P. F.; Mayes, R. T.; Dai, S., Carbon Materials for Chemical Capacitive Energy Storage. *Adv. Mater.* **2011,** 23, (42), 4828-4850.

35. Li, Y.; Fu, Z. Y.; Su, B. L., Hierarchically Structured Porous Materials for Energy Conversion and Storage. *Advanced Functional Materials* **2012,** 22, (22), 4634-4667.

36. Nishihara, H.; Kyotani, T., Templated Nanocarbons for Energy Storage. *Adv. Mater.* **2012,** 24, (33), 4473-4498.

37. Wang, J. C.; Kaskel, S., KOH activation of carbon-based materials for energy storage. *J. Mater. Chem.* **2012,** 22, (45), 23710-23725.

38. Chai, G. S.; Yoon, S. B.; Yu, J. S.; Choi, J. H.; Sung, Y. E., Ordered porous carbons with tunable pore sizes as catalyst supports in direct methanol fuel cell. *Journal of Physical Chemistry B* **2004,** 108, (22), 7074-7079.

39. Shao, Y. Y.; Sui, J. H.; Yin, G. P.; Gao, Y. Z., Nitrogen-doped carbon nanostructures and their composites as catalytic materials for proton exchange membrane fuel cell. *Appl Catal B-Environ* **2008,** 79, (1-2), 89-99.

40. Zhang, S. L.; Chen, L.; Zhou, S. X.; Zhao, D. Y.; Wu, L. M., Facile Synthesis of Hierarchically Ordered Porous Carbon via in Situ Self-Assembly of Colloidal Polymer and Silica Spheres and Its Use as a Catalyst Support. *Chemistry of Materials* **2010,** 22, (11), 3433-3440.

41. Chaudhari, S.; Kwon, S. Y.; Yu, J. S., Ordered multimodal porous carbon with hierarchical nanostructure as high performance electrode material for supercapacitors. *Rsc Advances* **2014,** 4, (73), 38931-38938.

42. Xie, K.; Qin, X. T.; Wang, X. Z.; Wang, Y. N.; Tao, H. S.; Wu, Q.; Yang, L. J.; Hu, Z., Carbon Nanocages as Supercapacitor Electrode Materials. *Adv. Mater.* **2012,** 24, (3), 347-+.

VITAE

Shih-Chieh Kung

EDUCATION and WORK EXPERIENCE

- Saint-Gobain Corporation, Northboro, Massachusetts Mar. 2015-Present
  Senior Research Engineer, Northboro R&D Center

- Lehigh University, Bethlehem, Pennsylvania Aug. 2009-Jan. 2015
  Ph.D., Department of Chemical and Biomolecular Engineering
  Advisor: Prof. Mark A. Snyder
  Thesis: *Hierarchical engineering of multimodal ordered nanoporous materials*

- Far Eastern New Century Corporation, Taoyuan, Taiwan Oct. 2004-Feb. 2009
  Research Scientist, R&D Center

- National Tsing Hua University, Hsinchu, Taiwan Sep. 2002-Jul. 2004
  M.S., Department of Chemical Engineering
  Advisor: Prof. Ta-Jo Liu
  Thesis: *Research and development of backlit light diffusing film*

- National Tsing Hua University, Hsinchu, Taiwan Sep. 1998-Jun. 2002
  B.S., Department of Chemical Engineering

PUBLICATIONS and REPORTS

1. Z. Wang, C. Li, H.J. Cho, **S.-C. Kung**, M. A. Snyder, W. Fan "Direct, single-step synthesis of hierarchical zeolites without secondary templating," *J. Mater. Chem. A*, **3**, (2015) 1298-1305
2. **S.-C. Kung**, C.-C. Chang, W. Fan, M. A. Snyder, "Template-free ordered mesoporous silicas by binary nanoparticle assembly," *Langmuir*, **30** (2014) 11802-11811
3. **S.-C. Kung**, M. A. Snyder, "Bimodal Three-Dimensionally Ordered Mesoporous Carbons with Tunable Large Mesopores," in preparation
4. **S.-C. Kung**, M. A. Snyder, "Scaffolded Growth of Thin Zeolite Films by 3DOm Carbon Films," in preparation
5. Z. Tian, **S.-C. Kung**, M. A. Snyder, "Convective Assembly of Binary Nanoparticle Thin films," in preparation
6. **S.-C. Kung**, Z. Tian, M. A. Snyder, "Three-dimensionally ordered binary colloidal crystal films," *EPI Graduate Progress Report (GRPR)* (2013). *(Cover article)*

SELECTED CONFERENCE PRESENTATIONS

1. **S.-C. Kung**, and M. A. Snyder, "Assembly of 3D Ordered Binary Silica Nanoparticle Superlattices and Multi-modal Porous Carbons", 88th ACS Colloids & Surface Science Symposium, Philadelphia, PA, 2014 *(Oral Presentation)*
2. **S.-C. Kung**, and M. A. Snyder, "Assembly of 3D Ordered Binary Silica Nanoparticle Superlattices and Multi-modal Porous Carbons", AIChE Annual Meeting, San Francisco, CA, 2013 *(Oral Presentation)*
3. **S.-C. Kung**, and M. A. Snyder, "Scaffolded Growth of Thin Zeolite Films towards High Performance Molecular Separations and Reaction-Separation Technologies", AIChE Annual Meeting, San Francisco, CA, 2013 *(Poster Presentation)*
4. **S.-C. Kung**, and M. A. Snyder, "Hierarchically Structured Porous Materials towards High Performance Molecular Separations and Reaction-Separation Technologies", EPI Annual Review meeting, Bethlehem, PA, 2013 *(Oral Presentation)*
5. **S.-C. Kung**, and M. A. Snyder, "Hierarchically Structured Porous Materials towards High Performance Molecular Separations and Reaction-Separation Technologies", The Catalysis Society of Metropolitan New York, Princeton, NJ, 2013 *(Poster Presentation)*

SKILLS and EXPERTISE

Synthesis, characterization, and coating process of organic and inorganic materials, such as polymers, adhesives, UV-curable resins, and inorganic colloidal nanoparticle solutions

Materials and Formulation Development

- Organic materials: UV curable acrylics, Pressure sensitive adhesives, Solvent/waterborne polymers, Liquid crystal solutions
- Inorganic materials: Sol-gel materials, Zeolites, Silica and metal nanoparticles, Gold@SiO_2 core-shell nanoparticles, highly ordered porous carbons, SiO_2/TiO_2 suspensions, Silane coupling agents

Product Development

- Optical films: Optical compensation/retardation films, Anti-reflection/Anti-glare films, Hard coating films
- Polymer adhesive coatings: Conductive & protective films, Thermal and UV curable PSA coatings
- Polarized UV aligned coatings

Process Development (integrated from lab, pilot to manufacturing processes)

- Roll-to-roll processes: Coating, Drying, Curing, Lamination, Polarized UV alignment, Rubbing, Slitting
- Measurement technique: In-line measurement of coating film properties, Coating meniscus monitoring
- Chemical processing: Mixing, Dispersing, Filtration, and Fluid delivery systems
- Lab-scale coatings: Wired bar coating, Spin coating, Convective assembly blade coating

Characterization & Analysis

- Electron microscopy: SEM, TEM, EDS
- Colloid and surface science: XRD, SAXS, Nitrogen Adsorption, DLS particle size

analysis, zeta-Potential

- Analytical measurement: FT-IR, UV-Vis, DSC, TGA, Rheometry, Surface Tensiometry, Contact Angle

AWARDS

- 1st Place Poster Award of Materials Engineering and Sciences Division, AIChE Annual Meeting, Pittsburgh, PA, 2012
- Poster award and Invited Talk, North-East Corridor Zeolite Association Conference, Philadelphia, PA, 2010

RESEARCH AFFILIATIONS

- American Institute of Chemical Engineers (AIChE)
- American Chemical Society (ACS)
- Emulsion Polymers Institute (EPI) at Lehigh University
- Center for Advanced Materials and Nanotechnology (CAMN) at Lehigh University